COUPLING OF ELECTRON AND ION DYNAMICS IN 1D, 2D AND 3D MATERIALS

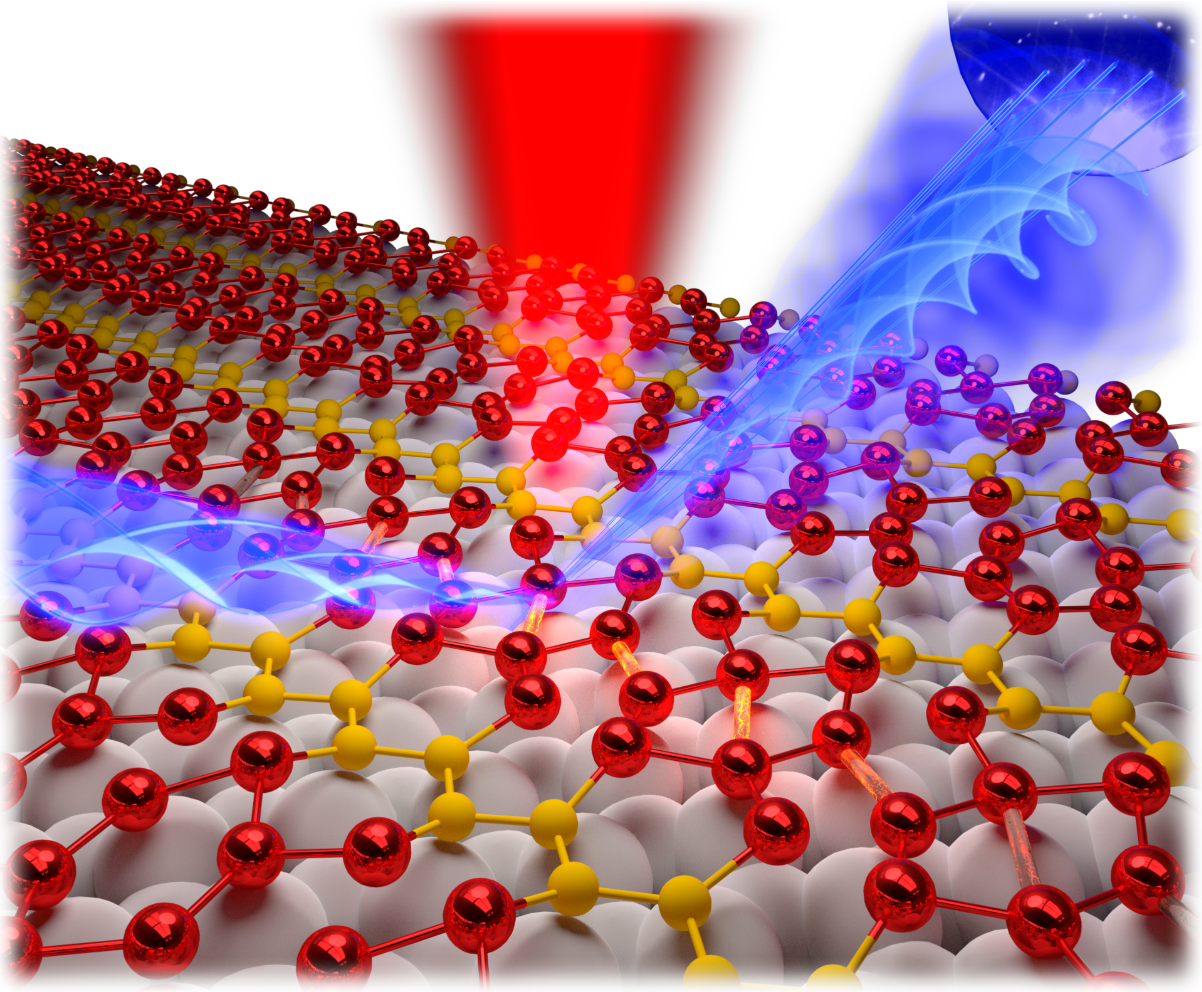

Dissertation zur Erlangung des akademischen Grades
doctor rerum naturalium (Dr. rer. nat.)

Andreas Lücke

Department Physik, Arbeitsgruppe Theoretische Materialphysik
Universität Paderborn

Name: Andreas Lücke
Geboren am: 29.07.1988
Geburtsort: Paderborn
Matrikelnummer: 6545979
Eingereicht am: 19.01.2017

Promotionskommission

Vorsitzender: Prof. Dr. rer. nat. habil. Cedrik Meier
(Universität Paderborn)
Erstgutachter: Prof. Dr. rer. nat. habil. Wolf Gero Schmidt
(Universität Paderborn)
Zweitgutachter: Prof. Dr. rer. nat. habil. Michael Horn-von Hoegen
(Universität Duisburg-Essen)
Beisitzer: Dr. rer. nat. Matthias Reichelt
(Universität Paderborn)

“Electric lamps were not invented by improving candles.”

Henri Audier

Kurzfassung

Organische Halbleiter finden aufgrund ihrer günstigen Herstellungsweise und ihren besonderen Eigenschaften wie z.B. Flexibilität immer mehr Anwendungen in moderner Elektronik. Da ein effizienter Ladungstransport dabei häufig zwingend notwendig ist, wird dieser am Beispiel von dem Polymer Poly(3-hexylthiophene) (P3HT) in dieser Arbeit untersucht. Im ersten Teil liegt der Fokus auf der Identifizierung von transporthemmenden strukturellen Defekten. Diese werden durch eine Vielzahl von Konfigurationen modelliert, deren Eigenschaften im Rahmen der Dichtefunktionaltheorie bestimmt werden. Als besonders transportschädigend herausgestellt haben sich dabei die Adsorption von Sauerstoff an das Kohlenstoff-Rückgrat der Polymerstränge sowie eine Verdrehung von zwei aufeinander folgenden P3HT Monomeren um Winkel im Bereich von 90°.

Da eine starke Kopplung von ionischen und elektronischen Freiheitsgraden interessante physikalische sowie technologisch relevante Effekte ermöglicht, steht diese Kopplung im Zentrum der weiteren Betrachtungen. In P3HT wird die Elektron-Phonon-Kopplung durch die Einführung von Polaron-Quasiteilchen berücksichtigt, welches zudem eine temperaturabhängige Beschreibung der Transporteigenschaften ermöglicht. Die Ergebnisse zeigen eine stark ausgeprägte Kopplung sowie eine maximale Ladungsträgerbeweglichkeit in Kettenrichtung von gut $40\ \mathrm{cm}^2/(\mathrm{Vs})$ bei Raumtemperatur, für P3HT-Filme ohne strukturelle Defekte.

Neuere Entwicklungen beruhen zudem zunehmend auf der konkreten Ausnutzung von speziellen Eigenschaften von Nanomaterialien, z.B. in Form von Quantenpunkten und Nanodrähten. Aus diesem Grund werden im letzten Teil der Arbeit Indium-Nanodrähte auf einer Siliziumoberfläche charakterisiert. Der Schwerpunkt liegt dabei auf einer theoretischen Beschreibung eines experimentell beobachteten, optisch getriebenen Phasenübergangs, da dieser vor allem durch eine stark gekoppelte, zeitabhängige Atomkern- und Elektron-Dynamik charakterisiert werden kann. Die Ergebnisse erklären dabei die Wirkmechanismen während dieses Phasenübergangs, wobei die theoretisch vorhergesagten Übergangszeitkonstanten dabei sehr gut mit dem Experiment übereinstimmen. Eine zusätzlich durchgeführte Bindungsanalyse visualisiert zudem den Verlauf des Phasenübergangs und gibt detaillierte Einblicke auf atomarer Ebene.

Abstract

Organic semiconductors experience increasingly applications in modern electronics due to their cheap manufacturing and their special properties like, e.g., flexibility. In general these applications require an efficient charge transport, which is investigated here using the example of the polymer Poly(3-hexylthiophene) (P3HT). Thereby, the focus is on the identification of strongly transport limiting structural defects. These defects are modeled by a variety of configurations for which the properties are determined in the framework of the density functional theory. An adsorption of oxygen to a polymer strand's carbon backbone as well as torsion angles around 90° between two adjacent P3HT monomers are found to strongly reduce the conductivity.

A strong coupling between ionic and electronic degrees of freedoms enables interesting physical and technological relevant effects. Therefore, the analysis of such couplings constitutes the main part in the following considerations. The electron-phonon coupling in P3HT is accounted for by introducing the polaron quasiparticle, which enables also a temperature-dependent transport description. The results indicate a distinct coupling and predict a maximum charge carrier mobility of about $40\ \mathrm{cm}^2/(\mathrm{Vs})$ at room temperature in polymer chain direction for P3HT films without structural defects.

Since modern processings exploit increasingly the particular properties of nanomaterials like, e.g., quantum dots and nanowires, the last part of the thesis deals with indium nanowires on a silicon surface. The representative focus is here on the theoretical description of an experimentally observed optically driven phase transition. This transition is characterized by strongly coupled, time-dependent ion and electron dynamics. The microscopic details of the phase transition are elucidated and the results are, e.g., additionally visualized by a detailed bonding analysis. The predicted phase transition time constants are thereby in good agreement with the experimental measurements.

Contents

1 **Introduction** 1

2 **Theoretical foundations** 5
  2.1 The many-body problem 5
  2.2 Density functional theory 6
  2.3 Van der Waals interaction 9
  2.4 Pseudopotentials 10
  2.5 Ab initio description of the quantum conductance 14
    2.5.1 Transport through an ideal quantum wire 14
    2.5.2 Quantum conductance across a potential barrier 16
    2.5.3 Determining the quantum conductance in real systems 17
  2.6 Temperature dependent mobility 30
  2.7 Bonding analysis 34
    2.7.1 Technical Implementation in Fortran 37

3 **Transport properties of P3HT** 41
  3.1 Influence of structural defects 42
    3.1.1 P3HT layer displacements 44
    3.1.2 Chain Torsions 45
    3.1.3 Chain Bending 50
    3.1.4 Isomer defect 51
    3.1.5 Oxygen impurities 54
  3.2 Temperature-dependent hole mobility of P3HT 59
    3.2.1 Tight-binding band structure 59
    3.2.2 Electron-phonon coupling constants 61
    3.2.3 Temperature-dependent chemical potential 62
    3.2.4 Temperature-dependent hole mobilities 63

4 Indium nanowires on Si(111) 71
4.1 Quantum conductance of regular indium nanowires upon oxygen adsorption 72
4.2 Optically driven phase transition 75
4.2.1 Identify contributing states 76
4.2.2 A detailed bonding analysis 85
4.2.3 Time dynamics of the phase transition 90
4.2.4 Excitation thresholds 92

5 Conclusion 95

A Extensions and modifications of the molecular editor `Avogadro` 99
A.1 Input files 99
A.2 Minor Bug fixes and Changes 99
A.3 Maximize periodic distance 100
A.4 Try to restore a molecule from folded atoms into the unit cell 102
A.5 Show `PWCond` system 102
A.6 Measure plane angle 103
A.7 Put in plane 104

B Publications 107

Acronyms 109

Bibliography 113

1

Introduction

Todays technology advances with a tremendous speed. On the one hand, the consumer electronics like smartphones, tablets, etc. become smaller and smaller, which is mainly achieved by an increasing density of electronic components. On the other hand, also the integrated circuits used in electronics contain more and more transistors per volume. This has also the advantage that the decreased size and distances between the transistors allows for a faster clock rate. Moreover, it enables the designs of system on chips (SoCs) with enhanced functionalities while small chip sizes are maintained.

Already in 1965 Gordon E. Moore published his observation that every two years the number of circuit components in an integrated circuit doubles[1]. To accommodate such a large number, the distance between circuit paths, transistor gate sizes, etc. need to be downsized. For instance, Intel uses currently a 14 nm manufacturing technology[2]. For comparison, 14 nm are more than 5000 times smaller than the thickness of a human hair. Moreover, Intel has announced the release of its new 10 nm processor generation with the codename Cannonlake in 2017, while IBM produces already 7 nm test chips[3].

The miniaturization of the semiconductor devices makes several challenges like heat dissipation and electromigration becoming more and more significant. In addition, the low-dimensionality and nanostructuring leads to an increased surface/volume ratio, where quantum mechanical effects become apparent. For instance, aside the laws of classical physics, one has to take care of a possible tunneling of charge carriers through a barrier, thereby causing leakage currents. Such effects are amongst others analyzed in Sec. 4.1, where the tunneling probability change from one metal nanowire to an adjacent one is investigated upon exposure to oxygen. In these nanowires charge carriers exhibit a strong coupling to each other without being directly connected.

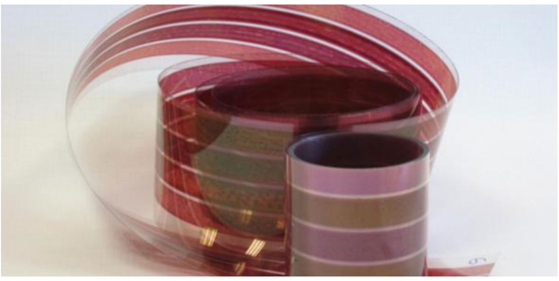

Figure 1.1: Organic solar cells offer a large flexibility for new application possibilities. The image is taken from Ref. 4 and under a Creative Commons License (CC BY-NC-SA 3.0).

However, there are also various applications which demand large transmission probabilities. For example, if electrical components need to be contacted, the resulting interface should impede the charge carrier transport between the different materials as less as possible. Thus, another important research topic deals with the search for well-conducting and controllable organic materials. Recently, the application of organic semiconductors in consumer products has increased considerably - ranging from organic light-emitting diode (OLED) displays to organic solar cells. Organic semiconductors have the advantage that they are usually cheap to produce and offer interesting properties like being mechanically flexible. Their manifold compositions give additional variabilities for design, thus opening up new application possibilities. Unfortunately organic materials suffer from relatively fast degeneration compared to inorganic semiconductors. In this context, a large part (Sec. 3.1) of this thesis pays attention to the influence of several kinds of defects in the organic polymer Poly(3-hexylthiophene) (P3HT) which is often used for organic solar cells.

Since interesting physics and technological relevant effects arise when electron and ion dynamics are coupled to each other, this work investigates also the coupling of ionic and electronic degrees of freedom by means of two different systems: (i) In Sec. 3.2 the polaron quasiparticle is introduced to account for the coupling between electrons and phonons in P3HT. The description allows for including also temperature effects due to ionic vibrations, which goes beyond the so far static transport characterization of P3HT. (ii) The last section 4.2 goes even further by examining the coupling of ion and electron dynamics yet time-resolved in indium nanowires. This system was chosen due to its very distinct coupling between electrons and ions. The focus is thereby on an in-depth analysis of a collective motion of the indium atoms towards another phase upon electronic excitation by a laser pulse. The mechanisms, leading to the experimentally realized phase transition, are investigated and visualized from different perspectives for which even a bonding analysis tool was implemented.

The thesis is divided into three parts: In the first one (Chap. 2), theoretical foundations needed to understand the following results are presented. It starts with a motivation and introduction of the density functional theory (DFT) followed by two different transport approaches which are used in the following chapter 3 to characterize the transport properties of the polymer P3HT. The last chapter deals with the widely studied indium nanowires on a Si(111) substrate and their interesting properties like an insulator-metal transition.

2

Theoretical foundations

In order to investigate material properties at the nanoscale from the theoretical point of view, it is often necessary to describe the system quantum mechanically. This requires a solution of a many-body problem as the studied systems include usually several nuclei and even more electrons.

This chapter deals with the theoretical framework used to describe the many-body problem from *first principles*. It starts with a general formulation of the many-body Schrödinger equation which needs to be simplified, leading to the density functional theory whose basics are shortly outlined afterwards.

2.1 The many-body problem

Starting point for a quantum mechanical description is the many-body Hamiltonian [5] which is the key operator in the Schrödinger equation

$$\mathbb{H} = \mathbb{H}_{\mathrm{e,kin}} + \mathbb{H}_{\mathrm{ee}} + \mathbb{H}_{\mathrm{I,kin}} + \mathbb{H}_{\mathrm{II}} + \mathbb{H}_{\mathrm{eI}}. \tag{2.1}$$

$\mathbb{H}_{\mathrm{e,kin}}$ and $\mathbb{H}_{\mathrm{I,kin}}$ denote the kinetic energy of the electrons and the atomic nuclei. The Coulomb interaction of the electrons is included by $\mathbb{H}_{\mathrm{ee}}$ and that of the nuclei via $\mathbb{H}_{\mathrm{II}}$. The term $\mathbb{H}_{\mathrm{eI}}$ takes the Coulomb interaction between electrons and nuclei into account. This Hamiltonian 2.1 acts onto a many-body wave function with all in all $3N_e + 3N_I$ coordinates[1] (labeled $\{\mathbf{r}\}$ and $\{\mathbf{R}\}$, respectively) where N_e denotes the number of electrons and N_I the number of ions

$$\mathbb{H}\Psi\left(\{\mathbf{r}\},\{\mathbf{R}\}\right) = E\Psi\left(\{\mathbf{r}\},\{\mathbf{R}\}\right). \tag{2.2}$$

---

[1] The factor 3 regards the three degrees of freedom of each particle along the spatial directions x, y and z.

Within the limits of the Born-Oppenheimer approximation[6], one can separate the "movement" of the electrons and ions. This can often be justified by the large mass difference between electrons and nuclei, assuming that the electrons can follow the ions' movements instantaneously. This approximation allows for considering the ion positions $\{\mathbf{R}\}$ as (fixed) parameters so that the many-body problem needs only to be solved for the electrons. The ion positions can afterwards be optimized by minimizing the system's total energy, e.g., with a gradient descent scheme. This requires the solution of the electronic many-body problem for each altered ion configuration.

Effects like electron-phonon couplings are neglected due to the Born-Oppenheimer approximation although they are crucial, e.g., for charge transport in organic semiconductors at finite temperatures. This disadvantage is overcome by employing a tight-binding model later on to include also polaronic effects. This model is presented in more detail in Sec. 2.6.

2.2 Density functional theory

Since the electronic wave function depends on $3N_e$ coordinates even after separation of the ions and electrons by means of the Born-Oppenheimer approximation, the many-electron problem is still too complicated to be solved directly.

A remedy is found by the density functional theory (DFT): According to the Hohenberg-Kohn theorem[7], the electron density $n(\mathbf{r})$ is an *unique* functional of a given potential $V(\mathbf{r})$, hence requiring the determination of the electron density $n(\mathbf{r})$ exclusively instead of the full wave function $\Psi\left(\{\mathbf{r}\}\right)$. This offers the tremendous advantage that the desired functional depends only on three variables instead of $3N_e$.

Unfortunately the Hohenberg-Kohn theorem does only say that the electron density $n(\mathbf{r})$ is sufficient to describe the system completely but not how to determine physical quantities like the total energy E in dependence on the electron density. Hence, one searches for a description of the total energy in functional dependence on the electron density. A general starting point is given by the following ansatz

$$E[n] = \langle \Psi \mid \mathbb{H}_{\mathrm{e,kin}} + \mathbb{H}_{\mathrm{ee}} \mid \Psi \rangle + \langle \Psi \mid v_{\mathrm{ext}}(\mathbf{r}) \mid \Psi \rangle = F[n] + \int v_{\mathrm{ext}}(\mathbf{r}) n(\mathbf{r}) d^3\mathbf{r}, \quad (2.3)$$

where $F[n]$ denotes the unknown functional expression for the kinetic energy and the electron-electron interaction in dependence on the electron density. The second term contains the external potential $v_{\mathrm{ext}}(\mathbf{r})$, especially the Coulomb potential generated by the atomic nuclei. According to Kohn & Sham[8] one can write

$$F[n] = T_0[n] + \frac{1}{2}\int\int \frac{n(\mathbf{r})n(\mathbf{r}')}{|\mathbf{r}-\mathbf{r}'|} d^3\mathbf{r} d^3\mathbf{r}' + E_{\mathrm{xc}}[n] \tag{2.4}$$

for the functional $F[n]$ (in atomic units[2]). The kinetic energy $T[n]$ of an interacting particle system is approximated by the kinetic energy $T_0[n]$ belonging to a system of non-interacting particles. The Coulomb interaction (second term) is also expressed for a system of non-interacting particles. The differences between an interacting and a non-interacting system is accounted for by adding $E_{\mathrm{xc}}[n]$, i.e., the so-called exchange-correlation correction[3]. Moreover, this term should take care of many-body effects like, e.g., the exchange-correlation hole. However, for the general case the exact expression for $E_{\mathrm{xc}}[n]$ is still unknown and has to be approximated, leading to a broad range of applicable exchange-correlation functionals which will be discussed later on (e.g., various flavors of the local density approximation, generalized gradient approximation, etc. cf. Refs. 11–18).

The electronic ground state (energetic minimum) is determined by calculating the functional derivative with respect to the electron density

$$\frac{\delta E[n]}{\delta n} \overset{!}{=} 0. \tag{2.5}$$

The variation has to be performed with the constraint that the particle number needs to be preserved. This additional condition can be formulated via $\int n(\mathbf{r})d^3\mathbf{r} = N_e$ and is mathematically realized by a Lagrange multiplier[19] μ

$$\frac{\delta}{\delta n}\left\{E[n] - \mu\left(\int n(\mathbf{r})d^3\mathbf{r} - N_e\right)\right\} = 0. \tag{2.6}$$

Inserting Eqs. 2.3 and 2.4 yields

$$\frac{\delta E[n]}{\delta n} = \frac{\delta F[n]}{\delta n} + v_{\mathrm{ext}}(\mathbf{r}) = \frac{\delta T_0[n]}{\delta n} + V_{\mathrm{eff}}(\mathbf{r}) = \mu, \tag{2.7}$$

with

$$V_{\mathrm{eff}}(\mathbf{r}) = v_{\mathrm{ext}}(\mathbf{r}) + \int \frac{n(\mathbf{r}')}{|\mathbf{r}-\mathbf{r}'|} d^3\mathbf{r}' + \frac{\delta E_{\mathrm{xc}}}{\delta n}, \tag{2.8}$$

which can be seen as an equation for a system of non-interacting particles in an effective potential V_{eff}[8]. The interacting particle system was thereby transformed into a single-particle description[4] with the same ground-state density $n(\mathbf{r})$. This offers the possibility to introduce one-particle wave functions $\phi_i(\mathbf{r})$ for the independent particles. The ground-state density can then be calculated with[5]

---

[2] Atomic units are an alternative to the SI units. They offer the advantage to be very convenient for atomic physics calculations due to their property that the four fundamental physical constants m_e, e, $\hbar$ and the Coulomb constant are unity by definition. For more details see, e.g., Ref. 9.

[3] Many-body effects beyond the exchange in the Hartree-Fock theory[10], which is based on a single Slater determinant description, are summed up by the term correlation.

$$n(\mathbf{r}) = \sum_{i=1}^{\infty} f_i |\phi_i(\mathbf{r})|^2, \tag{2.9}$$

where f_i denotes the occupation number of the orbital $\phi_i(\mathbf{r})$. While there exists no exact expression for the kinetic energy $T[n]$ of the interacting particle system, the kinetic energy $T_0[n]$ of the independent particle system can easily be calculated with the one-particle wave functions

$$T_0[n] = T_0\left[\sum_{i=1}^{\infty} f_i |\phi_i(\mathbf{r})|^2\right] = \sum_{i=1}^{\infty} f_i \left\langle \phi_i \right| - \frac{\nabla^2}{2} \left| \phi_i \right\rangle. \tag{2.10}$$

Performing the functional derivative in Eq. 2.7 with respect to $\phi_i^*(\mathbf{r})$ leads to one-particle Schrödinger equations[20], which can be used to determine the orbitals $\phi_i(\mathbf{r})$

$$\left\{ -\frac{\nabla^2}{2} + \overbrace{v_{\text{ext}}(\mathbf{r}) + \int \frac{n(\mathbf{r}')}{|\mathbf{r}-\mathbf{r}'|} d^3\mathbf{r}' + \frac{\delta E_{\text{xc}}}{\delta n}(\mathbf{r})}^{V_{\text{eff}}} \right\} \phi_i(\mathbf{r}) = \epsilon_i \phi_i(\mathbf{r}). \tag{2.11}$$

These equations are also known as Kohn-Sham equations[6].

To summarize the idea of the framework so far: The many-body wave function depends on too many variables and is therefore replaced by the electron density. By introducing a reference system of independent particles with the same ground-state electron density as the interacting system, the energy functional can be easily evaluated to find the energy minimum. The Hohenberg-Kohn theorem ensures thereby that the ground-state energy of both systems - the interacting and non-interacting one - is exactly the same[24].

The Kohn-Sham eigenvalues ϵ_i are not equal to the energy eigenvalues of the interacting system, however, they are often a good approximation and are frequently used[7].

---

[4] The equation describes quasi-independent particles since the influence of the other electrons enters only indirectly through the effective potential $V_{\text{eff}}(\mathbf{r})$ (mean field theory).

[5] The system must be describable in terms of a single Slater determinant.

[6] For comparison, the Hartree-Fock equations[10,21,22] are $\left[-\frac{\nabla^2}{2} + v_{\text{ext}}(\mathbf{r}) + \int \frac{n(\mathbf{r}')}{|\mathbf{r}-\mathbf{r}'|} d^3\mathbf{r}'\right] \phi_i(\mathbf{r}) + \int \Sigma^x(\mathbf{r},\mathbf{r}',\epsilon_i)\phi_i(\mathbf{r}')d^3\mathbf{r}' = \epsilon_i\phi_i(\mathbf{r})$ with $\Sigma^x(\mathbf{r},\mathbf{r}',\epsilon_i) = -\sum_{k}^{\text{occ}} \int \delta_{\sigma_i,\sigma_k} \frac{\phi_k^*(\mathbf{r}')\phi_k(\mathbf{r})}{|\mathbf{r}-\mathbf{r}'|}$. It looks similar, but the exchange potential Σ^x is nonlocal due to the integral over $\phi_i(\mathbf{r}')$, leading to an increased computational effort. In the GW approximation[21,23], the exchange potential Σ^x becomes the self-energy which includes also dynamically screening effects, not included in the Hartree-Fock method. Such screened charge carriers are called quasiparticles and the imaginary part of the self-energy expectation value gives hints towards the lifetime of their corresponding states (used in Sec. 4.2.1).

As $V_{\mathrm{eff}}(\mathbf{r})$ in Eq. 2.11 depends itself on the solution of the Kohn-Sham equation $\phi_i(\mathbf{r})$ (cf. Eq. 2.8 after inserting Eq. 2.9)), this equation has to be solved as an integro-differential equation self-consistently.

The exact expression for E_{xc}, which is needed in Eq. 2.8 to determine the effective potential V_{eff}, is still an unsolved problem. As already mentioned, there exist several functionals, where some of which contain to a certain extent exact (Hartree-Fock) exchange (e.g., B3LYP[15,16] or HSE06[18]).

A simple but often successfully applied approximation is called *local density approximation (LDA)*[8]

$$E_{\mathrm{xc}}[n] = \int n(\mathbf{r})\epsilon_{\mathrm{xc}}[n]d^3\mathbf{r} = \int n(\mathbf{r})\epsilon_{\mathrm{xc}}^{\mathrm{LDA}}(n(\mathbf{r}))d^3\mathbf{r} + \mathcal{O}[\nabla n]. \tag{2.12}$$

The function $\epsilon_{\mathrm{xc}}^{\mathrm{LDA}}(n(\mathbf{r}))$ depends only *locally* on the electron density (no functional any longer). There are several suggestions for parameterizing this function (e.g. Refs. 25 & 26).

The local density approximation can be generalized by taking beside the local density $n(\mathbf{r})$ also the local density gradient $\nabla n(\mathbf{r})$ into account in order to better incorporate effects based on inhomogeneities of the density. This semi-local approximation is called *generalized gradient approximation (GGA)*. The generalization is not unique - there exist several GGA functionals which depend in different ways on $n(\mathbf{r})$ and $\nabla n(\mathbf{r})$. A simple, commonly used generalized gradient approximation functional is called PBE and was suggested by Perdew, Burke and Ernzerhof[13,14] in 1996. Nevertheless, even with this functional the (i) self-interaction and (ii) long range Coulomb interaction remain unsolved problems. The latter one is considered in the following section.

2.3 Van der Waals interaction

As mentioned in the last section, the semi-local GGA functionals take beside the local density $n(\mathbf{r})$ also the gradient of the local density $\nabla n(\mathbf{r})$ into account. Now, if one considers a positively charged molecule, there will be a distance at which nearly no electron density is expected any more. Nevertheless, in a real system, the long range Coulomb interaction exists even at this distance, e.g., being able to attract a remote electron towards the molecule. However, this attractive force cannot be described correctly within LDA or GGA as the local density and its derivative vanish between molecule and electron.

---

[7] Beside some exceptions, this approximation is also applied in this work.

[8] This approximation is exact for a homogeneous electron gas.

Long-range effects like the van der Waals (vdW) interaction (dispersion) can be accounted for by extending the functional to long-ranged correlation contributions. This extended description is not only important for charged systems but in particular, e.g., for molecules adsorbed on surfaces. Moreover, the dispersion is essential for the interaction between molecules in an organic semiconductor (a molecular crystal). Since this work also deals with the organic polymer P3HT, the vdW interaction was included, namely by using the method of Grimme[27]. The Kohn-Sham equation is thereby extended by a R^{-6} damped term

$$E_{\mathrm{disp}} = -s_6 \sum_{i=1}^{N_I-1} \sum_{j=i+1}^{N_I} \frac{C_6^{ij}}{R_{ij}^6} f_{\mathrm{dmp}}(R_{ij}). \tag{2.13}$$

The sums take all pairwise interactions between each of the N_I atoms with distance R_{ij} and interaction strength C_6^{ij} into account and s_6 is a global scaling factor. The damping function

$$f_{\mathrm{dmp}}(R_{ij}) = \frac{1}{1 + e^{-d(R_{ij}/R_r - 1)}} \tag{2.14}$$

is added to avoid singularities at small R_{ij}. R_r corresponds thereby to the sum of the van der Waals radii of the atoms i and j. Grimme[27] suggests a value of 20 for the parameter d. The interaction coefficients C_6^{ij} can be determined from the geometric mean

$$C_6^{ij} = \sqrt{C_6^i C_6^j}, \tag{2.15}$$

where the atom specific coefficients C_6^i have been tabulated in Ref. 27.

2.4 Pseudopotentials

This work makes use of plane-wave expansions of the electron wave functions as they are well-suited for periodic systems and very efficient due to the availability of the fast Fourier transform (FFT). However, the expansion of electron wave functions requires a large basis set to describe the strongly oscillating behavior accurately in the region close to an atomic core. As the computational effort increases enormously with the size of the basis set, an alternative is needed to describe the regions around the cores. The augmented plane wave (APW) method[28] offers a possibility which uses atomic orbitals as basis set for the region around the cores and plane waves in the interstitial region. The pseudopotential method is another alternative which is used in this work. The basics of the pseudopotential formalism are shortly outlined in the following.

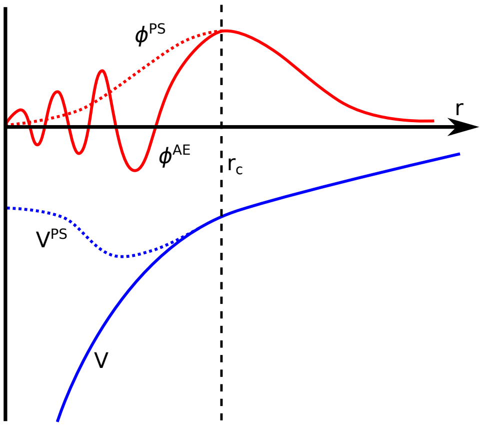

Figure 2.1: Schematic comparison of the pseudopotential V^{PS} with the original core potential V. Furthermore, the corresponding wave functions ϕ^{PS} and ϕ^{AE} are depicted. Both wave functions have to be equal from the cutoff radius r_c[29], [30].

First of all, the electrons are separated into two categories - the core electrons which are mainly located close to the nuclei and the valence electrons which are responsible for forming bonds. The *frozen core approximation* assumes that the core electrons remain unaffected by chemical bonds. Hence, their influence onto the valence electrons can be incorporated into the core potential, thereby reducing the effective number of electrons to deal with. In the worst case this reduces the accuracy of the results by about 0.1 eV[31]. However, in general this approximation is well-justified. After this, the many-body problem is only solved for the valence electrons whose external potential is replaced by an atom-specific pseudopotential containing the core electrons. The wave function of the valence electrons is called pseudo wave function ϕ^{PS} due to differences compared to the all-electron (AE) wave function[9]. The potential V^{PS} belonging to ϕ^{PS} is optimized during the pseudopotential generation to get a preferably smooth pseudo wave function. This reduces the number of plane-wave basis functions needed for the expansion. The potential is thereby also smoother and does not exhibit the diverging $1/r$ property close to the core (cf. Fig. 2.1).

Pseudopotentials have the property that the pseudo wave function and the all-electron wave function are equal outside of an atom-centered cutoff radius r_c (called augmentation region). The all-electron wave function inside the cutoff region can even be reconstructed mathematically for projector augmented wave (PAW) pseudopotentials[32,33], to get the AE wave function from a pseudopotential calculation. The linear reconstructing transformation $\mathcal{T}$ is derived in the following

$$|\phi^{\text{AE}}\rangle = \mathcal{T}\,|\phi^{\text{PS}}\rangle\,. \tag{2.16}$$

As already mentioned, it is assumed that the pseudo wave function and the all-electron wave function differ only within the cutoff radius (cf. Fig. 2.1). Hence, one can build up the transformation from single atom centered contributions

---

[9] This is the "real" wave function of the system where no pseudopotentials are used and all electrons are included in the calculation.

$$\mathcal{T} = 1 + \sum_{\alpha} \mathcal{T}_{\alpha}. \tag{2.17}$$

The index α sums over all atoms. $\mathcal{T}_{\alpha}$ is only non-zero within the cutoff radius which ensures that $|\phi^{\mathrm{AE}}\rangle = |\phi^{\mathrm{PS}}\rangle$ for $r > r_c$ (cf. Eq. 2.16 after insertion of Eq. 2.17).

An expression for $\mathcal{T}_{\alpha}$ can be found by expanding the system's solution $|\phi^{\mathrm{AE}}\rangle$ and $|\phi^{\mathrm{PS}}\rangle$ in any atom-centered basis (e.g partial wave functions)

$$|\phi^{\mathrm{AE}}\rangle = \sum_{i,\alpha} c_i^{\alpha} |\Phi_i^{\alpha}\rangle \qquad \text{and} \tag{2.18}$$

$$|\phi^{\mathrm{PS}}\rangle = \sum_{i,\alpha} c_i^{\alpha} |\tilde{\Phi}_i^{\alpha}\rangle , \tag{2.19}$$

where i is a macro index which runs over all quantum numbers of the system (e.g., l, m for the angular momentum). Eq. 2.19 requires that the basis functions for the pseudo wave function are chosen in that way that the expansion coefficients c_i^{α} are equal to the ones of Eq. 2.18. Moreover, one can define a projector $|\tilde{p}_j^{\beta}\rangle$ having the property

$$\langle \tilde{p}_j^{\beta} | \tilde{\Phi}_i^{\alpha} \rangle = \delta_{i,j}\delta_{\alpha,\beta}. \tag{2.20}$$

Applying this projector onto Eq. 2.19 one obtains

$$c_j^{\alpha} = \langle \tilde{p}_j^{\alpha} | \phi^{\mathrm{PS}} \rangle \tag{2.21}$$

for the expansion coefficients c_i^{α}. The difference between the all-electron wave function and the pseudo wave function can be written as

$$\begin{aligned} |\phi^{\mathrm{AE}}\rangle - |\phi^{\mathrm{PS}}\rangle &= \sum_{i,\alpha} c_i^{\alpha} \left(|\Phi_i^{\alpha}\rangle - |\tilde{\Phi}_i^{\alpha}\rangle \right) \\ \Leftrightarrow |\phi^{\mathrm{AE}}\rangle &= \sum_{i,\alpha} c_i^{\alpha} \left(|\Phi_i^{\alpha}\rangle - |\tilde{\Phi}_i^{\alpha}\rangle \right) + |\phi^{\mathrm{PS}}\rangle . \end{aligned} \tag{2.22}$$

Inserting the expansion coefficients determined in Eq. 2.21 yields

$$|\phi^{\mathrm{AE}}\rangle = \left[\sum_{i,\alpha} \left(|\Phi_i^{\alpha}\rangle - |\tilde{\Phi}_i^{\alpha}\rangle \right) \langle \tilde{p}_i^{\alpha} | + 1 \right] |\phi^{\mathrm{PS}}\rangle . \tag{2.23}$$

Comparing with Eq. 2.17 gives the prescription for the reconstructing transformation $\mathcal{T}$

$$\mathcal{T} = 1 + \sum_{i,\alpha} \left(|\Phi_i^{\alpha}\rangle - |\tilde{\Phi}_i^{\alpha}\rangle \right) \langle \tilde{p}_i^{\alpha} | . \tag{2.24}$$

In praxis, the linear transformation between the all-electron wave function and the pseudo wave function can be obtained by calculating the all-electron wave function $|\phi^{\mathrm{AE}}\rangle$ for a simple reference system consisting of one single atom. This solution can be expanded in any atom centered basis $|\Phi_i^\alpha\rangle$ getting the expansion coefficients c_i^α (cf. Eq. 2.18). After this, the system is solved again. However, now the pseudopotential is used to obtain also the pseudo wave function $|\phi^{\mathrm{PS}}\rangle$ for the reference system. The requirement that both wave functions have the same expansion coefficients c_i^α allows for the determination of the atomic basis $|\tilde{\Psi}_i^\alpha\rangle$ for the pseudo wave function by inverting Eq. 2.19. Moreover, the projector $|\tilde{p}_i{}^\alpha\rangle$ can also be obtained by inverting Eq. 2.20. Thus, all needed functions for $\mathcal{T}$ have been calculated (cf. Eq. 2.24). Assuming transferability of the pseudopotential[10], one can apply the determined $\mathcal{T}$ also to every other system.

The calculation of expectation values of any observable $\mathbb{O}$ (e.g., for the total energy of the system) would actually need the all-electron wave function

$$\langle \mathbb{O} \rangle = \langle \phi^{\mathrm{AE}} | \mathbb{O} | \phi^{\mathrm{AE}} \rangle \, . \tag{2.25}$$

This causes considerably computationally costs since every time the pseudo wave function has changed, the all-electron wave function has to be reconstructed. Moreover, this would wreck the advantage of the smaller plane-wave basis set because one needs much more plane waves to expand the AE wave function. By means of the PAW transformation one can avoid this additional effort. For this, Eq. 2.16 is inserted into Eq. 2.25 for the expectation value calculation

$$\langle \mathbb{O} \rangle = \langle \phi^{\mathrm{PS}} \mathcal{T}^\dagger | \mathbb{O} | \mathcal{T} \phi^{\mathrm{PS}} \rangle = \langle \phi^{\mathrm{PS}} | \underbrace{\mathcal{T}^\dagger \mathbb{O} \mathcal{T}}_{=\tilde{\mathbb{O}}=\mathbb{O}+\Delta\mathbb{O}} | \phi^{\mathrm{PS}} \rangle \tag{2.26}$$

with

$$\Delta\mathbb{O} = \sum_{i,j,\alpha} |\tilde{p}_i{}^\alpha\rangle \left[\underbrace{\langle \Phi_i^\alpha | \mathbb{O} | \Phi_j^\alpha \rangle - \langle \tilde{\Phi}_i^\alpha | \mathbb{O} | \tilde{\Phi}_j^\alpha \rangle}_{=O_{i,j}^\alpha} \right] \langle \tilde{p}_j{}^\alpha | \, . \tag{2.27}$$

Hence, one only needs to determine the additional term $\Delta\mathbb{O}$ for each observable $\mathbb{O}$. This circumvents the expensive transformation to the AE wave function, because now every expectation value can be calculated with the pseudo wave functions directly. For instance, to solve the Kohn-Sham equations 2.11, one has to transform the respective

---

[10] The wave functions localized at the core are assumed to remain unchanged as these orbitals participate only negligible in bonds.

Hamiltonian $\mathbb{H}$. $\tilde{\mathbb{H}}$ is obtained via $\Delta\mathbb{H}$ using Eq. 2.27

$$\Delta\mathbb{H} = \sum_{i,j,\alpha} \mid \tilde{p}_i^{\alpha}\rangle H_{i,j}^{\alpha} \langle \tilde{p}_j^{\alpha} \mid . \tag{2.28}$$

According to Ref. 24 one can use the separable Kleinman-Bylander pseudopotential representation in which an operator $O_{i,j}^{\alpha}$ from Eq. 2.27 becomes diagonal ($O_{i,j}^{\alpha} = \tilde{O}_i^{\alpha}\delta_{i,j}$). This approximation is used in the ballistic transport formalism presented in Sec. 2.5.3. For $\Delta\mathbb{H}$ this results in

$$\Delta\mathbb{H} = \sum_{i,\alpha} \tilde{H}_i^{\alpha} \mid \tilde{p}_i^{\alpha}\rangle\langle \tilde{p}_i^{\alpha} \mid . \tag{2.29}$$

2.5 Ab initio description of the quantum conductance through a scattering region

This section deals with the calculation of the quantum transport along a scattering region. For the ab initio description of this kind of transport several open source programs are available which follow different approaches to determine the desired transmission probabilities. For instance, the `Quantum Espresso`[34] package tool `WanT` makes use of Green's functions expressed in real space (cf. Ref. 35 for theoretical details). The `WanT` code requires thereby the electronic wave functions expressed in a maximal localized basis set. This requirement constitutes the largest drawback of this method as many supercell based programs (including the `Quantum Espresso` package) use plane-wave basis sets, which makes a time-consuming and error-prone conversion between both basis sets necessary. Moreover, it is rather difficult to expand strongly dispersive bands in Wannier functions used as maximal localized basis set in the `WanT` program. Hence, to circumvent the transformation into Wannier functions, an alternative ab initio approach is chosen here, which is not based on the Green's function formalism. It is implemented in the `PWCond` program which works in reciprocal space and is also part of the `Quantum Espresso` package.

Two simple examples illustrate the quantum transport first and introduce the utilized concept, to become familiar with the described physics. After this introduction the more general formalism is presented. The latter is later-on applied to real systems like the polymer P3HT (Sec. 3.1) and indium nanowires (Sec. 4.1).

2.5.1 Transport through an ideal quantum wire

The concept of the quantum conductance is applicable if the influence of inelastic scattering events (e.g., with atom cores) can be neglected. Moreover this transport

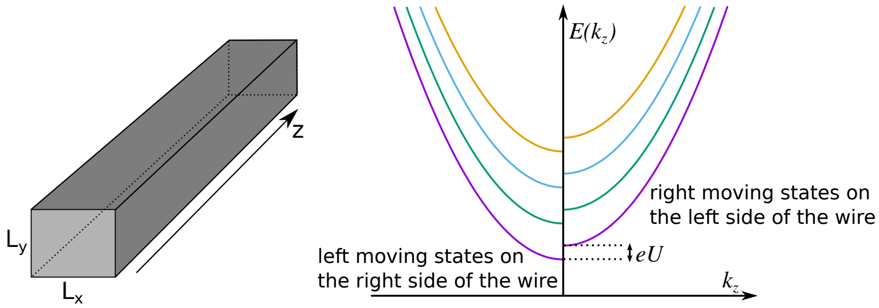
L_y
L_x
z
E(k_z)
right moving states on the left side of the wire
left moving states on the right side of the wire
eU
k_z

Figure 2.2: Ideal quantum wire (*left*) with parabolic band structure (*right*). The energy levels differ due to an applied voltage U to the ends of the ballistic conductor.

plays a role if the elongation of the scatterer is comparable small to the mean free path of the charge carriers[35]. This length is even at room temperature (300 K) in the two digit nanometer range for metals[36].

The ideal quantum wire depicted in Fig. 2.2 is the simplest system demonstrating the quantum conductance. With additional metallic contacts one can apply a voltage which creates a potential difference eU between the ends of the one dimensional ballistic[11] conductor that leads a current flow.

The (ballistic) current induced by an applied voltage U can be calculated by simple considerations (for the sake of simplicity for one single band): Each charge carrier with quasi-momentum k adds its contribution I_k to the total current

$$I_k = env_k = e\frac{1}{L}\frac{1}{\hbar}\frac{\partial \epsilon_k}{\partial k}, \tag{2.30}$$

where $n = 1/L$ denotes the charge carrier density and v_k the group velocity of those in transport direction. Summing up all contributions gathers the total current through the 1D ballistic conductor

$$I = \sum_k^{k_F} I_k = \frac{e}{L\hbar}\sum_k^{k_F}\frac{\partial \epsilon_k}{\partial k}. \tag{2.31}$$

The density of states in k-space becomes nearly continuously for large L, hence the sum in Eq. 2.31 can be rewritten as an integral ($\sum_k \to \frac{L}{2\pi}\int dk$)

$$I = 2\cdot\frac{e}{2\pi\hbar}\int_0^{k_F}\frac{\partial \epsilon_k}{\partial k} = 2\cdot\frac{e}{2\pi\hbar}\int_0^{\epsilon_F} d\epsilon. \tag{2.32}$$

The additional factor of 2 takes the assumed spin degeneracy into account. The real flowing net current is then given by the superposition of the currents flowing from left to right and vice versa

---

[11] The transport is called ballistic if any scattering events can be neglected.

$$I_{\text{total}} = I_{r\to l} + I_{l\to r} = 2\cdot\frac{e}{2\pi\hbar}\int_0^{\epsilon_F} d\epsilon - 2\cdot\frac{e}{2\pi\hbar}\int_{eU}^{\epsilon_F} d\epsilon = \frac{2e^2}{h}U. \tag{2.33}$$

The conductance G can be evaluated with the formula $G = I/U$

$$G = \frac{2e^2}{h} = G_0. \tag{2.34}$$

Notably, the conductance is independent of the length of the ballistic conductor. This follows from the fact that the charge carrier density n decreases with increasing L ($\propto 1/L$) but the number of k-states per energy interval increases ($\propto L$). Hence, both effects cancel each other.

So far, no scatterer was considered and it was said that the length scale of the ballistic transport is smaller than the mean free path of the charge carriers. This provokes the question where does the resistance come from? The answer is that it is not an intrinsic resistance of the quantum wire but a contact resistance with energy dissipation at the interfaces between the wire and the surrounding metallic contacts. It arises due to the fact that the metallic contacts carry approximately infinitely many modes compared to the quantum wire which has usually only a few ones[35]. This mismatch in the number of current carrying modes at the interfaces requires a redistribution of the total current, thereby leading to an interface resistance. Therefore, one can say that the contact resistance of a single mode conductor is $G_0^{-1} \approx 12.9\ \mathrm{k\Omega}$.

2.5.2 Quantum conductance across a potential barrier

The foregoing section presented the simplest version of quantum conductance - the ballistic conductor, the *ideal* conductor. This system is now extended by a scattering potential barrier.

Fig. 2.3 depicts the potential shape of a system with scattering region in sector II on

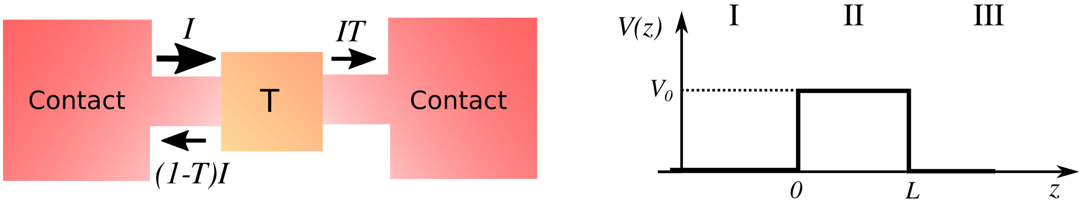

Figure 2.3: *Left:* System with a scattering region in which a current I is transmitted with a probability T and reflected with a probability $(1-T)$. An example for a simple scattering region is a potential barrier (*right*).

the right. For electrons with an energy smaller than eV_0 the transmission probability equals the tunneling probability through the barrier. The conductance formula 2.34 can be extended with the transmission probability, to calculate the conductivity of a system with scattering region

$$G = \overbrace{\frac{2e^2}{h}}^{G_0} T. \tag{2.35}$$

The contact resistance can be separated from the resistance induced by the scatterer by rewriting Eq. 2.35

$$G^{-1} = G_0^{-1}\frac{1}{T} = \overbrace{G_0^{-1}}^{\text{contact resistance}} + \overbrace{G_0^{-1}\frac{1-T}{T}}^{\text{scatterer resistance}}, \tag{2.36}$$

which correctly describes the fact that the system has no intrinsic resistance for $T = 1$.

The required transmission probability is obtained by solving the 1D Schrödinger equation for an incoming wave (e.g., e^{ikz} from left). For the wave function in the three sectors I, II and III the ansatz

$$\Psi(z) = \begin{cases} e^{ikz} + r \cdot e^{-ikz} & z \text{ in I} \\ A \cdot e^{i\kappa z} + B \cdot e^{-i\kappa z} & z \text{ in II} \\ t \cdot e^{ikz} & z \text{ in III} \end{cases} \tag{2.37}$$

can be used. The four unknowns in Eq. 2.37 (t, r, A and B) are determined by the continuity conditions for the wave function and its derivative at the interfaces between the sectors. The transmission probability is given by $T = |t|^2$, the reflection by $R = |r|^2$.

2.5.3 Determining the quantum conductance in real systems

The following subsection explains a possible method for calculating the quantum transport in realistic, three dimensional systems. The theoretical considerations are based on Refs. 37 and 38.

The investigated systems consist of semi-infinite periodically repeated contacts, represented by unit cells which surround the scattering region (cf. Fig. 2.4). The quantum conductance will be calculated along these contacts in z direction for a given mode energy E. For technical reasons the system is assumed to be periodic in the xy plane. Therefore, surrounding vacuum has to be chosen large enough if 1D structures are investigated.

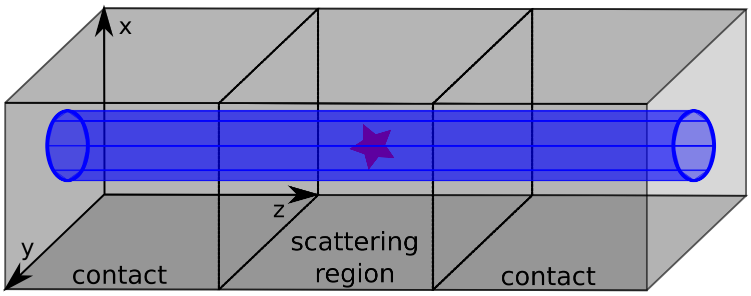

Figure 2.4: Composition of the system to be analyzed. The middle scattering region is allowed to inherit every kind of defect, however, the surrounding ideal contact unit cells have to be semi-infinite periodically repeated along z direction.

The essential parts to calculate the transport can be divided into three steps:

1. Calculation of all possible wave functions in the three regions left & right contact and the scattering region *without* specifying the boundary conditions at the borders of the regions[12] (Sec. 2.5.3.1).
2. Determination of existing k modes in both contacts. Therefore, the complex band structure[13] needs to be calculated (Sec. 2.5.3.2).
3. Similar to the potential barrier example above, for each propagating mode[14] in the left contact the transmission and reflexion coefficients are determined via continuity conditions at the boundaries (Sec. 2.5.3.3).

The listed steps will be explained in more detail in the following. These details might be skipped up to Eq. 2.70ff. to get directly to the final results.

2.5.3.1 Calculating the wave function

This part deals with the calculation of all possible wave functions with still open boundary conditions for a given mode energy E in all three regions. Starting point is the Kohn-Sham equation extended by an additional reconstruction term due to the use of pseudopotentials

---

[12] With fixed boundary conditions there would be only one wave function due to the need for unambiguity (except some degenerated states).

[13] In the complex band structure complex k values occur also beside real k values. These k modes do not spread over the full crystal but appear at interfaces. More details can be found in Sec. 2.5.3.2.

[14] A k mode is propagating if it neither diverges nor converges towards zero for $z \to \pm\infty$. This is equivalent to a real valued k as the Bloch theorem states that a wave function differs only by a complex phase factor in two unit cells if k does not contain an imaginary part which would change the absolute value of the phase factor $e^{ikz} = e^{i\Re(k)z} \cdot e^{-\Im(k)z}$.

$$E\,|\psi\rangle = -\frac{\hbar^2}{2m}\nabla^2\,|\psi\rangle + V_{\mathrm{loc}}\,|\psi\rangle + \underbrace{\sum_{i,\alpha}\tilde{H}_i^\alpha\,|\tilde{p}_i^{\,\alpha}\rangle\,\langle\tilde{p}_i^{\,\alpha}\mid\psi\rangle}_{=\Delta\mathbb{H}\text{ cf. Eq. 2.29}}. \tag{2.38}$$

The local potential V_{loc} contains the electrostatic potential from the cores modified by the pseudopotentials and the exchange and correlation contributions. In the following, the bra-ket notation is dropped in order to make use of an explicit argument listing of the various functions

$$\begin{aligned} E\psi(\mathbf{r}) = -\frac{\hbar^2}{2m}\nabla^2\psi(\mathbf{r}) + V_{\mathrm{loc}}(\mathbf{r})\psi(\mathbf{r}) + \sum_{\alpha,l,m}\sum_{\mathbf{R}_\perp} Z_l^\alpha W_{lm}^\alpha(\mathbf{r}-\boldsymbol{\tau}^\alpha-\mathbf{R}_\perp) \\ \times\int d^3\mathbf{r}'[W_{lm}^\alpha(\mathbf{r}'-\boldsymbol{\tau}^\alpha-\mathbf{R}_\perp)]^*\psi(\mathbf{r}'), \end{aligned} \tag{2.39}$$

where $\boldsymbol{\tau}^\alpha$ denotes the position of the αth atom in the unit cell. The last term corresponds to $\Delta\mathbb{H}$ in Eq. 2.38 after transformation into the angular momentum basis with the angular momentum quantum numbers l and m. W_{lm}^α & Z_l^α thereby include $\tilde{H}_i^\alpha$ and the projectors $\langle\tilde{p}_i^{\,\alpha}|$ of the pseudopotentials. Due to the periodicity in the xy plane, $\mathbf{R}_\perp$ sums over all lattice vectors in this plane. The periodicity allows for the application of the Bloch theorem $\psi(\mathbf{r}+\mathbf{R}_\perp)=\psi(\mathbf{r})e^{i\mathbf{k}_\perp\cdot\mathbf{R}_\perp}$, where $\mathbf{k}_\perp$ is perpendicular aligned to the transport direction (k_z). Hence, Eq. 2.39 can be rewritten as

$$E\psi(\mathbf{r}) = -\frac{\hbar^2}{2m}\nabla^2\psi(\mathbf{r}) + V_{\mathrm{loc}}(\mathbf{r})\psi(\mathbf{r}) + \sum_{\alpha,l,m} C_{\alpha,l,m} Z_l^\alpha \sum_{\mathbf{R}_\perp} e^{i\mathbf{k}_\perp\cdot\mathbf{R}_\perp} W_{lm}^\alpha(\mathbf{r}-\boldsymbol{\tau}^\alpha-\mathbf{R}_\perp) \tag{2.40}$$

with

$$C_{\alpha,l,m} = \int d^3\mathbf{r}'[W_{lm}^\alpha(\mathbf{r}'-\boldsymbol{\tau})]^*\psi(\mathbf{r}'). \tag{2.41}$$

Eq. 2.40 is an *inhomogeneous* integro-differential equation. It can be solved in two steps:

1. At first, only the homogeneous part of the equation is solved

   $$E\psi_n(\mathbf{r}) = -\frac{\hbar^2}{2m}\nabla^2\psi_n(\mathbf{r}) + V_{\mathrm{loc}}(\mathbf{r})\psi_n(\mathbf{r}), \tag{2.42}$$

   where n numbers the linear independent solutions for the system.

2. Subsequently, a particular solution of the inhomogeneous equation needs to be found. Therefore, only one $C_{\alpha,l,m}$ is set to 1 whereas all other coefficients are set 0. This is done sequentially for one after another giving an inhomogeneous

differential equation for each $C_{\alpha,l,m}$

$$\begin{aligned} E\psi_{\alpha,l,m}(\mathbf{r}) = &-\frac{\hbar^2}{2m}\nabla^2\psi_{\alpha,l,m}(\mathbf{r}) + V_{\mathrm{loc}}(\mathbf{r})\psi_{\alpha,l,m}(\mathbf{r}) \\ &+Z_l^\alpha \sum_{\mathbf{R}_\perp} e^{i\mathbf{k}_\perp\cdot\mathbf{R}_\perp} W_{lm}^\alpha(\mathbf{r}-\boldsymbol{\tau}^\alpha-\mathbf{R}_\perp). \end{aligned} \tag{2.43}$$

The general solution of Eq. 2.40 is obtained by combining the solutions of the homogeneous and the particular equations

$$\psi(\mathbf{r}) = \sum_n a_n\psi_n(\mathbf{r}) + \sum_{\alpha,l,m} C_{\alpha,l,m}\psi_{\alpha,l,m}(\mathbf{r}). \tag{2.44}$$

The yet undetermined coefficients a_n and $C_{\alpha,l,m}$ will be later determined by the boundary conditions of the three regions. Different $\mathbf{k}_\perp$ do not couple to each other in Eq. 2.40, hence the system can be solved separately for each $\mathbf{k}_\perp$. The obtained transmission probabilities can be summed up subsequently (weighted with the corresponding weight $\mathbf{w}_{\mathbf{k}_\perp}$).

In the following, the solution strategy for the homogeneous equation 2.42 is presented first. After this, the same strategy will be used in a slightly modified manner to solve the inhomogeneous equation 2.43.

Solution of the homogeneous equation

Due to the periodicity in the xy plane, the wave function $\psi_n(\mathbf{r})$ and the local potential $V_{\mathrm{loc}}(\mathbf{r})$ can be expanded in plane waves in lateral direction

$$\begin{aligned} \psi_n(\mathbf{r}) &= \sum_{\mathbf{G}_\perp} \psi_n(\mathbf{G}_\perp, z)e^{i(\mathbf{k}_\perp+\mathbf{G}_\perp)\cdot\mathbf{r}_\perp}, \\ V_{\mathrm{loc}}(\mathbf{r}) &= \sum_{\mathbf{G}_\perp} \psi_n(\mathbf{G}_\perp, z)e^{i\mathbf{G}_\perp\cdot\mathbf{r}_\perp}. \end{aligned} \tag{2.45}$$

This transforms the homogeneous equation into

$$\begin{aligned} E\psi_n(\mathbf{G}_\perp, z) = &\frac{\hbar^2}{2m}\left\{-\frac{d^2}{dz^2} + |\mathbf{k}_\perp+\mathbf{G}_\perp|^2\right\}\psi_n(\mathbf{G}_\perp, z) \\ &+\sum_{\mathbf{G}'_\perp} V_{\mathrm{loc}}(\mathbf{G}_\perp-\mathbf{G}'_\perp, z)\psi_n(\mathbf{G}'_\perp, z). \end{aligned} \tag{2.46}$$

The solution of this equation requires the local potential V_{loc} in dependence on $\mathbf{G}_\perp$ and z. It can be obtained from $V_{\mathrm{loc}}(\mathbf{G})$ if the supercell approach is also applied in z direction with periodicity L_z. The latter is calculated beforehand in self-consistent DFT runs for each of the three regions separately.

The periodic continuation in z direction leads to a systematic inaccuracy in the potential of the scattering region as this sector does not have an intrinsic periodicity. This is in contrast to the surrounding semi-infinite contacts and causes discontinuities at the interfaces. The mismatch can be minimized by including several contact unit cells into the scattering region. This increases the distance between the scatterer and its periodic image. Thereby it improves the potential matching at the boundaries between the scattering region and the ideal contacts.

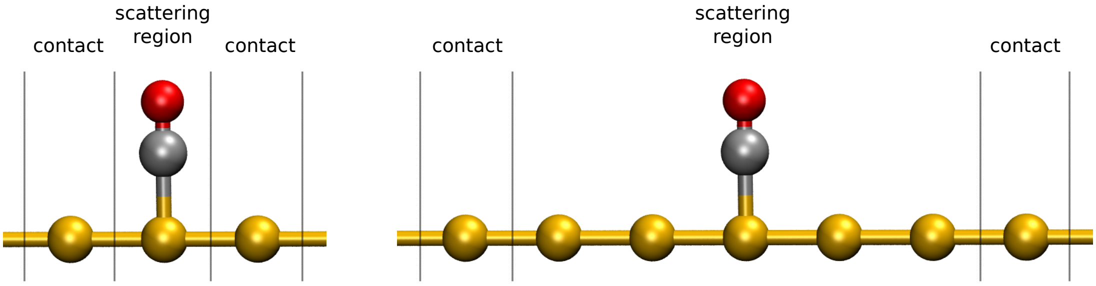

Figure 2.5: Possibilities to model a gold chain with an adsorbed CO scatterer.

Fig. 2.5 depicts different possibilities to model an infinite gold chain with a CO molecule as scatterer. With respect to the periodically repeated contact unit cells to semi-infinite leads, both possibilities describe formally the same system. However, there will be large differences in the results due to the periodic continuation of the scattering region potential: In the left model the periodically repeated CO adsorption dominates the scattering region much more than in the right model, leading to wrong results as the description of a *single* scatterer is desired.

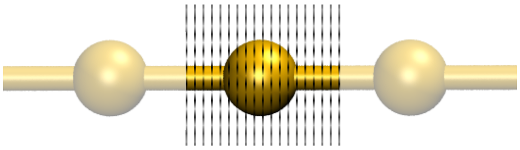

Figure 2.6: Exemplary division of an unit cell of an infinite gold chain into 18 slabs.

$V_{\mathrm{loc}}(\mathbf{G})$ is transformed into $V_{\mathrm{loc}}(\mathbf{G}_\perp, z)$ by dividing the unit cell into N slabs with z-independent local potential (cf. Fig. 2.6)[15]. Thereby N denotes the number of FFT supporting points of the local potential along the z axis.

Every slab gets a z-independent potential $V_p(\mathbf{G}_\perp)$ assigned which is obtained by inverting the following equation

---

[15] It is also possible to make use of the equation $V_{\mathrm{loc}}(\mathbf{G}_\perp, z) = \sum_{G_z} V_{\mathrm{loc}}(\mathbf{G}) e^{iG_z z}$, however, Ref. 37 considers this way as numerical less accurate. This is caused by the fact that numeric is always less accurate than analytic evaluation which is used in the following.

$$V_{\text{loc}}(\mathbf{G}) = \sum_{p=1}^{N} \left[\frac{1}{L_z} \int_{z_{p-1}}^{z_p} e^{-iG_z z} dz \right] V_p(\mathbf{G}_\perp), \tag{2.47}$$

where $z_p = pL_z/N$ denotes the z coordinate of the right boundary of the p^{th} slab.

After this partition, the wave function ψ_n^p belonging to the p^{th} slab has the conditional equation

$$\begin{aligned} E\psi_n^p(\mathbf{G}_\perp, z) = \frac{\hbar^2}{2m} &\left\{ -\frac{d^2}{dz^2} + |\mathbf{k}_\perp + \mathbf{G}_\perp|^2 \right\} \psi_n^p(\mathbf{G}_\perp, z) \\ &+ \sum_{\mathbf{G}'_\perp} V_p(\mathbf{G}_\perp - \mathbf{G}'_\perp) \psi_n^p(\mathbf{G}'_\perp, z). \end{aligned} \tag{2.48}$$

Eq. 2.48 needs the second derivative with respect to z which is a numerical problem[16]. Therefore, the ansatz

$$\psi_n^p(\mathbf{G}_\perp, z) = \sum_\lambda \Psi_\lambda^p(\mathbf{G}_\perp) \{ a_{\lambda n}^p e^{ik_\lambda^p (z - z_{p-1})} + b_{\lambda n}^p e^{-ik_\lambda^p (z - z_p)} \} \tag{2.49}$$

is used for the wave function with $k_\lambda^p = \sqrt{2m(E - E_\lambda^p)}/\hbar$. $\Psi_\lambda^p(\mathbf{G}_\perp)$ and E_λ^p are obtained by solving the z-independent eigenvalue equation

$$E_\lambda^p \Psi_\lambda^p(\mathbf{G}_\perp) = \frac{\hbar^2}{2m} |\mathbf{k}_\perp + \mathbf{G}_\perp|^2 \Psi_\lambda^p(\mathbf{G}_\perp) + \sum_{\mathbf{G}'_\perp} V_p(\mathbf{G}_\perp - \mathbf{G}'_\perp) \Psi_\lambda^p(\mathbf{G}'_\perp). \tag{2.50}$$

This equation can be rewritten as a matrix system for $\mathbf{G}_\perp = G_{x_n, y_m}$ where $\Psi_\lambda^p(\mathbf{G}_\perp)$ denotes the solution vector. With the abbreviated form $a_{x_{\mathbf{n}}, y_{\mathbf{m}}} = \frac{\hbar^2}{2m} |\mathbf{k}_\perp + G_{x_{\mathbf{n}}, y_{\mathbf{m}}}|^2 + V_p(0)$ for the diagonal elements and $b_{x_{\mathbf{n}}, y_{\mathbf{m}}; x'_{\mathbf{r}}, y'_{\mathbf{q}}} = V_p(G_{x_{\mathbf{n}}, y_{\mathbf{m}}} - G'_{x'_{\mathbf{r}}, y'_{\mathbf{q}}})$ for the non-diagonal elements, one obtains

$$E_\lambda^p \begin{pmatrix} \Psi_\lambda^p(G_{x_{\mathbf{1}}, y_{\mathbf{1}}}) \\ \Psi_\lambda^p(G_{x_{\mathbf{2}}, y_{\mathbf{1}}}) \\ \vdots \\ \Psi_\lambda^p(G_{x_{\mathbf{n}}, y_{\mathbf{n}}}) \end{pmatrix} = \begin{pmatrix} a_{x_{\mathbf{1}}, y_{\mathbf{1}}} & b_{x_{\mathbf{1}}, y_{\mathbf{1}}; x'_{\mathbf{2}}, y'_{\mathbf{1}}} & \cdots & b_{x_{\mathbf{1}}, y_{\mathbf{1}}; x'_{\mathbf{n}}, y'_{\mathbf{n}}} \\ b_{x_{\mathbf{2}}, y_{\mathbf{1}}; x'_{\mathbf{1}}, y'_{\mathbf{1}}} & a_{x_{\mathbf{2}}, y_{\mathbf{2}}} & \cdots & b_{x_{\mathbf{2}}, y_{\mathbf{1}}; x'_{\mathbf{n}}, y'_{\mathbf{n}}} \\ \vdots & \vdots & \ddots & \ddots \\ b_{x_{\mathbf{n}}, y_{\mathbf{n}}; x'_{\mathbf{1}}, y'_{\mathbf{1}}} & b_{x_{\mathbf{n}}, y_{\mathbf{n}}; x'_{\mathbf{2}}, y'_{\mathbf{1}}} & \cdots & a_{x_{\mathbf{n}}, y_{\mathbf{n}}} \end{pmatrix} \cdot \begin{pmatrix} \Psi_\lambda^p(G_{x_{\mathbf{1}}, y_{\mathbf{1}}}) \\ \Psi_\lambda^p(G_{x_{\mathbf{2}}, y_{\mathbf{1}}}) \\ \vdots \\ \Psi_\lambda^p(G_{x_{\mathbf{n}}, y_{\mathbf{n}}}) \end{pmatrix}. \tag{2.51}$$

The dimension of the matrix is determined by the number of $\mathbf{G}_\perp$ vectors which will be denoted as N_{2D} in the following. An eigenvalue problem solver provides the N_{2D} eigenvalues E^p_λ and eigenvectors $\Psi^p_\lambda(\mathbf{G}_\perp)$ numerically. Inserting this into the original ansatz in Eq. 2.49 yields the wave function for slab p which still contains the undetermined coefficients $a^p_{\lambda n}$ and $b^p_{\lambda n}$. As λ sums over all N_{2D} eigenvalues in ansatz 2.49, there will be N_{2D} $a^p_{\lambda n}$'s and $b^p_{\lambda n}$'s per slab. Eq. 2.48 has to be solved for each slab to obtain the wave function $\psi_n(\mathbf{G}_\perp, z)$ over the full unit cell. This increases the number of undetermined coefficients by the factor N (number of slabs). All together there are $2 \cdot N_{2D} \cdot N$ unknowns which have to be determined to obtain an unambiguous wave function $\psi(\mathbf{G}_\perp, z)$. This is accompanied by two equations for each $\mathbf{G}_\perp$ due to the required continuity of the wave function and its derivative at the interfaces between the slabs. As there are $N-1$ interfaces between N slabs (cf. Fig. 2.6), $2 \cdot N_{2D} \cdot (N-1)$ unknowns can be determined from this equations[17]. Hence, $2N_{2D}$ degrees of freedom are remaining which can be used to construct $2N_{2D}$ linear independent solutions for $\psi_n(\mathbf{G}_\perp, z)$.

---

[16] It is of course possible to determine the derivative by difference quotients, however, this would also couple different z coordinates to each other (instead of only the $\mathbf{G}_\perp$'s). The dimension M of the resulting matrix system would increase by a factor of N while the computational effort is $\mathcal{O}(M^3)$. This is asymptotically much slower than the method presented in this section which offers a linear scaling with the number of slabs N.

Solution of the inhomogeneous equation

Solving the inhomogeneous equation 2.43 requires a similar procedure like the one for the homogeneous equation (described in the previous section). Analog to the homogeneous wave function in Eq. 2.45, the inhomogeneous wave function $\psi_{\alpha,l,m}(\mathbf{r})$ is expanded in plane waves

$$\psi_{\alpha,l,m}(\mathbf{r}) = \sum_{\mathbf{G}_\perp} \psi_{\alpha,l,m}(\mathbf{G}_\perp, z) e^{i(\mathbf{k}_\perp + \mathbf{G}_\perp)\cdot \mathbf{r}_\perp}. \tag{2.52}$$

Inserting into the inhomogeneous conditional equation 2.43 and splitting into N slabs results in

$$\begin{aligned} E\psi^p_{\alpha,l,m}(\mathbf{G}_\perp, z) = {} & \frac{\hbar^2}{2m}\left\{-\frac{d^2}{dz^2} + |\mathbf{k}_\perp + \mathbf{G}_\perp|\right\}\psi^p_{\alpha,l,m}(\mathbf{G}_\perp, z) \\ & + \sum_{\mathbf{G}'_\perp} V_p(\mathbf{G}_\perp - \mathbf{G}'_\perp)\psi^p_{\alpha,l,m}(\mathbf{G}'_\perp, z) \\ & + Z^\alpha_l W^\alpha_{lm}(\mathbf{k}_\perp + \mathbf{G}_\perp, z - \tau^\alpha_z) e^{-i(\mathbf{k}_\perp + \mathbf{G}_\perp)\cdot \tau^\alpha_\perp}. \end{aligned} \tag{2.53}$$

Again, to numerically stabilize the differentiation with respect to z, an ansatz for the wave function $\psi^p_{\alpha,l,m}$ is used

$$\psi^p_{\alpha,l,m}(\mathbf{G}_\perp, z) = \sum_\lambda \Psi^p_\lambda(\mathbf{G}_\perp)\left\{f^p_{\lambda,\alpha,l,m} + a^p_{\lambda,\alpha,l,m} e^{ik^p_\lambda(z - z_{p-1})} + b^p_{\lambda,\alpha,l,m} e^{-ik^p_\lambda(z - z_p)}\right\}. \tag{2.54}$$

---

[17] Further details about the determination of the unknowns by the continuity conditions can be found in Refs. 37 and 38.

Here, $\Psi_\lambda^p(\mathbf{G}_\perp)$ denotes the eigenvector solution of Eq. 2.50, which was determined in the previous part to construct the homogeneous solution. $f^p_{\lambda,\alpha,l,m}$ is the particular solution which can be obtained with the following equation

$$\left\{\frac{\hbar^2}{2m}\frac{d^2}{dz^2} + E - E_\lambda^p\right\} f^p_{\lambda,\alpha,l,m}(z) = Z_l^\alpha \sum_{\mathbf{G}_\perp} [\Psi_\lambda^p(\mathbf{G}_\perp)]^* W^\alpha_{lm}(\mathbf{k}_\perp + \mathbf{G}_\perp, z - \tau_z^\alpha) e^{-i(\mathbf{k}_\perp+\mathbf{G}_\perp)\cdot\tau_\perp^\alpha}. \tag{2.55}$$

E_λ^p is the eigenvalue which belongs to the eigenvector $\Psi_\lambda^p(\mathbf{G}_\perp)$. This equation can be solved with the Green's function

$$g_\lambda^p(z) = \begin{cases} e^{ik_\lambda^p z}/(2ik_\lambda^p) & z \geq 0 \\ e^{-ik_\lambda^p z}/(2ik_\lambda^p) & z < 0 \end{cases} \tag{2.56}$$

as resolvent for the operator $\left\{\frac{\hbar^2}{2m}\frac{d^2}{dz^2} + E - E_\lambda^p\right\}$ which results in

$$f^p_{\lambda,\alpha,l,m} = Z_l^\alpha \sum_{\mathbf{G}_\perp} [\Psi_\lambda^p(\mathbf{G}_\perp)]^* e^{-i(\mathbf{k}_\perp+\mathbf{G}_\perp)\cdot\tau_\perp^\alpha} \int_{z_{p-1}}^{z_p} dz' g_\lambda^p(z-z') W^\alpha_{lm}(\mathbf{k}_\perp + \mathbf{G}_\perp, z' - \tau_z^\alpha). \tag{2.57}$$

The coefficients $a^p_{\lambda,\alpha,l,m}$ and $b^p_{\lambda,\alpha,l,m}$ of the ansatz 2.54 are again determined by the continuity conditions for the wave function $\psi_{\alpha,l,m}(\mathbf{G}_\perp, z)$ and its derivative at the interface between two adjacent slabs. Here, the Green's function 2.56 is only used to solve Eq. 2.55. It has nothing to do with the common method which calculates the quantum transport directly with the help of Green's functions[35,39].

This section dealt with the solution of the homogeneous (2.42) and the inhomogeneous equation 2.43. The general solution for Eq. 2.40 is obtained by superposition of both solutions (cf. Eq. 2.44). The remaining degrees of freedom have to be chosen in order to construct a wave function which is continuously differentiable at the boundaries between the contacts and the scattering region.

2.5.3.2 Calculating the complex band structure in the contacts

This section covers the second of all in all three steps to solve the scattering problem. Therefore, the wave functions in the contacts are assumed to be periodic with the unit cell length L_z. Applying the Bloch theorem yields

$$\psi_k(\mathbf{G}_\perp, z + L_z) = e^{ikL_z}\psi_k(\mathbf{G}_\perp, z). \tag{2.58}$$

This condition can be used to determine the current carrying, propagating modes in the contacts. These modes are characterized by a real valued k $(= k_z)$ and constitute eigenstates of an infinite, periodically repeated contact. Moreover, Eq. 2.58 gives also modes with complex k - those are called evanescent modes[18]. Due to the complex k, the absolute value of the corresponding wave function ψ_k increases or decreases (depends on the sign of the imaginary part) in each unit cell. That is why those modes cannot be eigenstates of an infinite system. However, here in the third step they have to be taken into account as the interface between contacts and scattering region disturbs the periodicity, causing the existence of those imaginary modes.

The k modes, which fulfill the Bloch theorem 2.58, are obtained by inserting the basis sets $\{\psi_n\}$ and $\{\psi_{\alpha,l,m}\}$, calculated in the previous sections, in the ansatz

$$\psi_k = \sum_{n=1}^{2N_{2D}} a_{n,k}\psi_n + \sum_{\alpha=1}^{N_a}\sum_{l}\sum_{m=-l}^{l} C_{\alpha,l,m,k}\psi_{\alpha,l,m}. \tag{2.59}$$

Here, N_a denotes the number of atoms whose augmentation region lies in the unit cell range $0 \leq z \leq L_z$. An atom is even included in N_a if it is not itself positioned in the range $0 \leq z \leq L_z$, but its augmentation sphere extends into the considered region. In particular one has to take care of the periodicity of the atoms. This leads to a double counting of atoms whose augmentation region cuts the left or right boundary. For instance, one periodic replica of an atom whose sphere cuts the $z = 0$ plane, will cut the $z = L_z$ plane - hence, there are contributions from two atoms.

All together $2N_{2D}$ coefficients for $a_{n,k}$ and $N_a \sum_l (2l+1)$ coefficients for $C_{\alpha,l,m,k}$ have to be determined. The periodic boundary conditions give for each of the N_{2D} $\mathbf{G}_\perp$'s two conditional equations by using the Bloch theorem

$$\begin{aligned} \psi_k(\mathbf{G}_\perp, L_z) &= e^{ikL_z}\psi_k(\mathbf{G}_\perp, 0) \quad \text{and} \\ \psi'_k(\mathbf{G}_\perp, L_z) &= e^{ikL_z}\psi'_k(\mathbf{G}_\perp, 0), \end{aligned} \tag{2.60}$$

where ψ'_k denotes the derivative of ψ_k with respect to z. Hence, there are $N_a \sum_l (2l+1)$ conditions missing to determine a mode ψ_k uniquely. The missing conditions are given by the previously mentioned Eq. 2.41

$$C_{\alpha,l,m,k} = \int d^3\mathbf{r}[W^{\alpha}_{l,m}(\mathbf{r} - \boldsymbol{\tau}^{\alpha})]^* \psi_k(\mathbf{r}), \tag{2.61}$$

whereby the integral is over the total real space. However, as the pseudopotential projectors $W^{\alpha}_{l,m}(\mathbf{r} - \boldsymbol{\tau}^{\alpha})$ are only non-zero inside an (atom centered) augmentation region, the effective integration area can be strongly reduced. Nevertheless one has to take care of projectors $W^{\alpha}_{l,m}(\mathbf{r} - \boldsymbol{\tau}^{\alpha})$ which are non-zero outside the interval $0 \leq z \leq L_z$ since the ψ_n's and $\psi_{\alpha,l,m}$'s are only defined inside this interval. This problem can be solved by using the Bloch theorem $\psi_k(\mathbf{G}_\perp, z) = e^{-ikL_z}\psi_k(\mathbf{G}_\perp, z + L_z)$ for the region

---

[18] disappearing, volatile partial waves

$-L_z \leq z \leq 0$ and $\psi_k(\mathbf{G}_\perp, z) = e^{ikL_z}\psi_k(\mathbf{G}_\perp, z - L_z)$ for $L_z \leq z \leq 2L_z$. Therefore, equation

$$\begin{aligned} C_{\alpha,l,m,k} = &\int_0^{L_z} dz \int d^2\mathbf{r}_\perp [W^\alpha_{l,m}(\mathbf{r} - \boldsymbol{\tau}^\alpha)]^* \psi_k(\mathbf{r}) \\ &+ e^{-ikL_z} \int_0^{L_z} dz \int d^2\mathbf{r}_\perp [W^\alpha_{l,m}(\mathbf{r} - \boldsymbol{\tau}^\alpha - \mathbf{e}_z L_z)]^* \psi_k(\mathbf{r}) \end{aligned} \tag{2.62}$$

can be used instead of Eq. 2.61 for atoms whose augmentation sphere cuts the $z = 0$ plane. Similarly, one obtains

$$\begin{aligned} C_{\alpha,l,m,k} = &\int_0^{L_z} dz \int d^2\mathbf{r}_\perp [W^\alpha_{l,m}(\mathbf{r} - \boldsymbol{\tau}^\alpha)]^* \psi_k(\mathbf{r}) \\ &+ e^{ikL_z} \int_0^{L_z} dz \int d^2\mathbf{r}_\perp [W^\alpha_{l,m}(\mathbf{r} - \boldsymbol{\tau}^\alpha + \mathbf{e}_z L_z)]^* \psi_k(\mathbf{r}) \end{aligned} \tag{2.63}$$

for atoms whose augmentation region cuts the $z = L_z$ plane. The number of these atoms cutting either the $z = 0$ or $z = L_z$ plane will be denoted with N_c in the following. For those N_c atoms the equations 2.62 and 2.63 are used while Eq. 2.61 is valid for the remaining $N_a - N_c$ atoms.

Inserting ansatz 2.59 into the conditions Eqs. 2.60 - 2.63 gives a generalized eigenvalue problem of the form $AX = e^{ikL_z}BX$ where A and B are quadratic matrices. The eigenvector X contains the desired coefficients $a_{n,k}$ and $C_{\alpha,l,m,k}$. The eigenvalues e^{ikL_z} constitute the complex band structure by resolving to k. Eq. 2.61 plays a special role for the generalized eigenvalue problem as it does not contain a e^{ikL_z} factor. After inserting ansatz 2.59, this equation gives $(N_a - N_c)\sum_l (2l + 1)$ conditions which couple the $a_{n,k}$ and $C_{\alpha,l,m,k}$ to each other

$$\begin{aligned} C_{\alpha',l',m',k} = &\sum_n a_{n,k} \int d^3\mathbf{r} [W^\alpha_{l,m}(\mathbf{r} - \boldsymbol{\tau}^\alpha)]^* \psi_n(\mathbf{r}) \\ &+ \sum_{\alpha,l,m} C_{\alpha,l,m,k} \int d^3\mathbf{r} [W^\alpha_{l,m}(\mathbf{r} - \boldsymbol{\tau}^\alpha)]^* \psi_{\alpha,l,m}(\mathbf{r}). \end{aligned} \tag{2.64}$$

This equation can be resolved to $C_{\alpha,l,m,k}$ for $(N_a - N_c)$ atoms in dependence on the other coefficients. Inserting these equations into the generalized eigenvalue problem reduces its dimension by $(N_a - N_c)\sum_l (2l + 1)$ to $(2N_{2D} + N_c \sum_l (2l + 1))$.

All together one can determine $(2N_{2D} + N_c \sum_l (2l + 1))$ k modes ψ_k in the contacts which can be divided into propagating and evanescent modes, depending on the imaginary part of the corresponding k value. If only evanescent modes are found, the calculation can be stopped for the originally given energy channel E, as only propagating modes can extend itself over a semi infinite contact, thereby carrying a current.

Finally, only the determination of the transmission probability is still missing which will be covered in the following section.

2.5.3.3 Determination of transmission and reflection coefficients

Based on the results of the previous sections, the transmission and reflection coefficients can be determined for each propagating mode ψ_k. The possibility of one mode to scatter into another is thereby automatically included in the calculation.

For the sake of simplicity, it is temporarily assumed that both contacts are equal here. Similar to the simple potential barrier (cf. Sec. 2.5.2), one can use an ansatz for the wave function Ψ in the three sectors *contact–scattering region–contact* for each propagating (real-valued) k in the left contact

$$\Psi = \begin{cases} \psi_k + \sum\limits_{\Im(k')\leq 0} r_{k,k'}\psi_{k'} & z < 0 \\ \sum\limits_{n} a_n\psi_n + \sum\limits_{\alpha,l,m} C_{\alpha,l,m}\psi_{\alpha,l,m} & 0 \leq z \leq L \\ \sum\limits_{\Im(k')\geq 0} t_{k,k'}\psi_{k'} & z > L \quad . \end{cases} \tag{2.65}$$

$\Im(k') \leq 0$ comprises all left running modes in the left contact and $\Im(k') \geq 0$ all right running modes in the right contact. The left and right propagating modes ($\Im(k) = 0$) are distinguished according to the sign of their probability current in z direction

$$\begin{aligned} I_k(z) = \Im\Bigg[&\frac{\hbar}{m}\int d^2\mathbf{r}[\psi_k(\mathbf{r})]^*\frac{\partial}{\partial z}\psi_k(\mathbf{r}) \\ &+\frac{2}{\hbar}\sum_{\alpha,l,m} Z_l^\alpha C^*_{\alpha,l,m}\int_{-\infty}^{z} dz'\int d^2\mathbf{r}'_\perp[W^\alpha_{l,m}(\mathbf{r}'-\boldsymbol{\tau}^\alpha)]^*\psi_k(\mathbf{r}')\Bigg] \, . \end{aligned} \tag{2.66}$$

In a system without pseudopotentials, the first part of Eq. 2.66 is equivalent to the integrated quantum-mechanical probability current density. However, since ψ_k is a pseudo wave function, one has to add the subsequent correction term[37] here.

In the following, the determination of the unknowns in Eq. 2.65 is presented. There are all in all $(2N_{2D} + N_c\sum_l (2l+1))$ k modes (cf. previous section), a value which coincidences with the joined number of $r_{k,k'}$ and $t_{k,k'}$. Moreover, there are $2N_{2D}$ plus $N_a\sum_l (2l+1))$ degrees of freedom due to the a_n's and $C_{\alpha,l,m}$'s, respectively. In summary, this results into the need for $4N_{2D} + (N_c + N_a)\sum_l (2l+1)$ conditional equations.

The requirement of a continuously differentiable wave function at the boundaries between the three regions results in two conditions per $\mathbf{G}_\perp$ for each interface. These are sufficient to determine $4N_{2D}$ unknowns. Inserting the ansatz 2.65 for the scattering region into Eq. 2.41 gives $N_a \sum_l (2l+1)$ further conditions

$$C_{\alpha,l,m} = \sum_n a_n \int d^3\mathbf{r}[W^{\alpha}_{l,m}(\mathbf{r}-\boldsymbol{\tau}^{\alpha})]^*\psi_n(\mathbf{r}) + \sum_{\alpha',l',m'} C_{\alpha',l',m'} \int d^3\mathbf{r}[W^{\alpha}_{l,m}(\mathbf{r}-\boldsymbol{\tau}^{\alpha})]^*\psi_{\alpha',l',m'}(\mathbf{r}). \tag{2.67}$$

In Sec. 2.5.3.1 it was mentioned that parts of the contacts have to be included also into the scattering region. This improves the transition between scattering region and contacts and reduces the systematic inaccuracy due to the periodicity of the scattering region's potential in z direction. In the previous section, atoms, whose augmentation sphere cuts the $z=0$ plane, generated $N_c/2$ equations. Further $N_c/2$ equations were generated by cuts through the $z=L_z$ plane (cf. Eqs. 2.62 and 2.63). Since several contact unit cells are included in the scattering region, the same kind of atoms cut the $z=0$ and $z=L$ plane[19] as in the periodically continued contacts in the previous section.

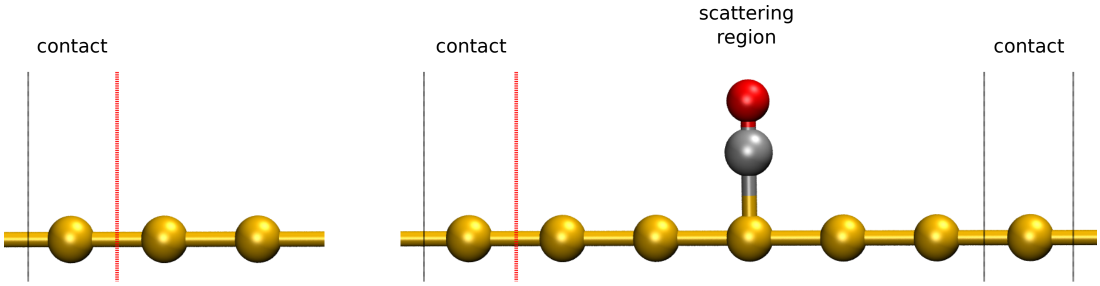

Figure 2.7: The red marked interface is surrounded by the same atoms in the periodically continued contact (*left*) and the full scattering system (*right*).

Fig. 2.7 visualizes the situation using the example of an infinite gold chain with CO adsorption. Since there are the same atoms around the red marked boundary in the ideal contact as well as in the full scattering system, the corresponding $C_{\alpha,l,m}$'s in the contacts and in the scattering region have to be equal. After inserting the ansatz 2.59 for ψ_k in Eq. 2.65 on gets $N_c/2\sum_l (2l+1)$ conditions for the $z=0$ plane by coefficient comparison

$$C_{\alpha,l,m} = C_{\alpha,l,m,k} + \sum_{\Im(k')\leq 0} r_{k,k'} C_{\alpha,l,m,k'}. \tag{2.68}$$

By the same arguments, further $N_c/2\sum_l (2l+1)$ conditions are obtained for the $z=L$ plane

$$C_{\alpha,l,m} = \sum_{\Im(k')\geq 0} t_{k,k'} C_{\alpha,l,m,k'}. \tag{2.69}$$

---

[19] interfaces between the three sectors; scattering region has length L while contacts have length L_z

Altogether one has $4N_{2D} + (N_c + N_a)\sum_l (2l+1)$ conditional equations forming an equation system for the unknowns $r_{k,k'}$, a_n, $C_{\alpha,l,m}$ and $t_{k,k'}$. Solving this system gives the desired transmission coefficients $t_{k,k'}$. These coefficients have to be weighted with the probability current I_k (cf. Eq. 2.66) to obtain the transmission for a propagating mode ψ_k

$$T_k = \frac{1}{I_k}\left(\sum_{k'} I_{k'}|t_{k,k'}|^2\right). \tag{2.70}$$

The sum runs over all right propagating modes k' in the right contact. This is equivalent to a real valued k' and a probability current $I_{k'} > 0$ for the belonging mode $\psi_{k'}$.

Generalization of Eq. 2.35 gives the conductivity for the originally selected energy channel (given by the parameter E in Eq. 2.38)

$$G = \frac{2e^2}{h}\sum_k T_k. \tag{2.71}$$

The full procedure can be repeated to obtain the conductivity for other energy channels E.

A scattering region without defects, i.e., without scatterer, constitutes a limiting case in which one has $t_{k,k'} = \delta_{k,k'}$. This reduces the quantum conductance to the strict ballistic regime with

$$G(E) = \frac{2e^2}{h}\sum_k 1 = \frac{2e^2}{h}\cdot N_k(E), \tag{2.72}$$

i.e., it corresponds simply to the number of bands $N_k(E)$ at the given energy E. This ballistic conductor is solely limited by the contact resistance (cf. Sec. 2.5.1). Eqs. 2.70 and 2.71 describe thereby the defect induced deviations from the strict ballistic limit in Eq. 2.72 due to scatterers. In this sense, the present approach goes beyond the ballistic regime, whereby temperature dependent effects and a finite bias can be partially taken into account in linear response by[35]

$$I = \frac{2e}{h}\int\sum_k T_k(E)\cdot(f_\mu(E) - f_\nu(E))dE. \tag{2.73}$$

Here, $f_{\mu/\nu}$ are the Fermi distributions (at arbitrary temperatures) with the chemical potentials μ and ν in the left & right contacts[20], respectively. μ and ν can be unequal due to an applied bias $U = \frac{\mu-\nu}{e}$. If the transmission is approximately constant over the energy range where the transport occurs, one can rewrite Eq. 2.73 as[35]

---

[20] Here it is assumed that the transmission probability from left to right equals the one in the opposite direction (right to left).

$$I \approx \frac{2e}{h}\sum_k T_k(E_f)\int (f_\mu(E)-f_\nu(E))dE = \frac{2e}{h}\sum_k T_k(E_f)\cdot(\mu-\nu)$$
$$\Rightarrow G = \frac{2e^2}{h}\sum_k T_k(E_f). \tag{2.74}$$

This equation accounts for the temperature broadening of the Fermi distribution while the described scattering mechanisms are restricted to static defects. Dynamic scattering effects due to electron-phonon interactions are investigated with a different approach which is presented in the following section.

2.6 Temperature dependent mobility

The previous section described a possibility to calculate the quantum conductance through a scattering region. This method is well suited to analyze the influence of static defects suppressing the transport. However, for dynamic distortions, e.g., caused by phonons, this concept is not appropriate. The temperature dependent transport is analyzed to full extend by taking all phonons into account, which requires a new theoretical transport description. Therefore, the formalism presented in Refs. 40 & 41 is used to investigate the charge carrier mobility in organic crystals. This formalism has already proven to successfully describe the transport properties of naphthalene[42,43], durene[43,44] and guanine[43,45] in the relevant temperature regime. In the following, this theoretical framework is shortly sketched, for details the reader is referred to the original publications 40 and 41.

The temperature dependent mobility tensor $\mu_{\alpha\beta}$ can be theoretically accessed by a current-current correlation function by means of the Kubo formula[46]

$$\mu_{\alpha\beta} = \frac{1}{eN_c}\frac{1}{2k_BT}\int_{-\infty}^{\infty}\langle j_\alpha(t)j_\beta(0)\rangle_H\,dt. \tag{2.75}$$

Here, N_c denotes the number of charge carriers contributing to the current density j. Equation 2.75 is evaluated by calculating the operator of the current density $\mathbf{j}$

$$\mathbf{j} = \frac{d\mathbf{P}}{dt} = \frac{1}{i\hbar}[\mathbf{P}, H], \tag{2.76}$$

where $\mathbf{P} = e\sum_M \mathbf{R}_M a_M^\dagger a_M$ expresses the polarization operator in second quantization using the particle annihilation (creation) operators $a_M^{(\dagger)}$ in real space (located at site $\mathbf{R}_M$). The commutator in Eq. 2.76 contains the Hamilton operator which can also be expressed in second quantization

$$H = \sum_{M,N} \epsilon_{M,N} a_M^\dagger a_N + \sum_{\mathbf{Q}} \hbar\omega_{\mathbf{Q}} \left(b_{\mathbf{Q}}^\dagger b_{\mathbf{Q}} + \frac{1}{2} \right) + \sum_{M,\mathbf{Q}} \hbar\omega_{\mathbf{Q}} g_{M,M}^{\mathbf{Q}} \left(b_{\mathbf{Q}}^\dagger + b_{-\mathbf{Q}} \right) a_M^\dagger a_M . \tag{2.77}$$

The Hamiltonian consists of a pure electronic part with the transfer integrals $\epsilon_{M,N}$, a pure phononic part, where a harmonic oscillator is assumed, and a coupling between both parts weighted with the electron-phonon (el-ph) coupling constant $g_{M,M}^{\mathbf{Q}}$. Note that $\mathbf{Q}$ is a macro index summing over the phonon wave vectors $\mathbf{q}$ as well as over all phonon modes λ.

This Hamiltonian can be approximately diagonalized by introducing the polaron quasiparticle, describing the charge carriers dressed by phonons

$$\tilde{H} = \sum_{M,N} a_M^\dagger \tilde{\epsilon}_{M,N} a_N + \sum_{\mathbf{Q}} \hbar\omega_{\mathbf{Q}} \left(b_{\mathbf{Q}}^\dagger b_{\mathbf{Q}} + \frac{1}{2} \right), \tag{2.78}$$

with the polaron transfer integrals

$$\tilde{\epsilon}_{M,N} = \epsilon_{M,N} \exp \left[- \sum_{\mathbf{Q}} \left(\frac{1}{2} + N_{\mathbf{Q}} \right) |g_{M,M}^{\mathbf{Q}} - g_{N,N}^{\mathbf{Q}}|^2 \right], \tag{2.79}$$

where $N_{\mathbf{Q}}$ is the phonon occupation number according to the Bose-Einstein statistics $N_{\mathbf{Q}} = \left(\exp\left[\frac{\hbar\omega_{\mathbf{Q}}}{k_B T} \right] - 1 \right)^{-1}$. As can be seen from Eq. 2.79, the polaron transfer integrals are smaller than the bare charge carrier transfer integrals $\epsilon_{M,N}$, leading to a decreased band curvature (dispersion) and therefore to an increased effective mass of the polarons. This effect is also known as band narrowing[40,41].

Transferring the polaron part of the Hamiltonian in Eq. 2.78 from real to reciprocal space gives

$$\tilde{H} = \sum_{\mathbf{k}} \tilde{\epsilon}(\mathbf{k}) a_{\mathbf{k}}^\dagger a_{\mathbf{k}} + \sum_{\mathbf{Q}} \hbar\omega_{\mathbf{Q}} \left(b_{\mathbf{Q}}^\dagger b_{\mathbf{Q}} + \frac{1}{2} \right), \tag{2.80}$$

with the polaron band structure $\tilde{\epsilon}(\mathbf{k})$, which can be calculated from the polaron transfer integrals

$$\tilde{\epsilon}(\mathbf{k}) = \sum_{N'} \tilde{\epsilon}_{M,N'} e^{-i\mathbf{k}\mathbf{R}_{N'}} = \sum_{N'} \tilde{\epsilon}_{0,N'-M} e^{-i\mathbf{k}\mathbf{R}_{N'-M}} \overset{L=N'-M}{\widehat{=}} \sum_{L} \underbrace{\tilde{\epsilon}_{0,L}}_{\tilde{\epsilon}_L} e^{-i\mathbf{k}\mathbf{R}_L} . \tag{2.81}$$

Here, it was used that the transfer integral $\epsilon_{M,N}$, describing the charge transfer from a molecule in unit cell M to one in unit cell N, depends only on the relative distance between M and N. Therefore, for the sake of simplicity, one index can be suppressed by making the coordinates relative to a molecule located at the origin.

Evaluating now Eq. 2.75 including a thermal average results into two mobility contributions, which describe different transport regimes

$$\mu_{\alpha\beta} = \mu_{\alpha\beta}^{(\mathrm{coh})} + \mu_{\alpha\beta}^{(\mathrm{inc})}. \tag{2.82}$$

The coherent contribution ("band transport") is given by

$$\begin{aligned} \mu_{\alpha\beta}^{(\mathrm{coh})} = -\frac{e}{2N_c k_B T \hbar^2} \sum_{L,M,N} R_{L,\alpha}\tilde{\epsilon}_{0,L} R_{N,\beta}\tilde{\epsilon}_{0,N} \frac{1}{N_\Omega} \sum_{\mathbf{k}_1,\mathbf{k}_2} e^{-i\mathbf{k_1}(\mathbf{R}_M+\mathbf{R}_N)} e^{i\mathbf{k_2}(\mathbf{R}_M-\mathbf{R_L})} \\ \times n(\mathbf{k}_1)\left(1-n(\mathbf{k}_2)\right) \int_{-\infty}^{\infty} e^{(it/\hbar)[\tilde{\epsilon}(\mathbf{k}_1)-\tilde{\epsilon}(\mathbf{k}_2)]} dt, \end{aligned} \tag{2.83}$$

where the sums L, M and N run over the nearest neighbors with lattice vectors $\mathbf{R}_{L/M/N}$. N_Ω is the number of unit cells and $n(\mathbf{k})$ the Fermi-Dirac distribution

$$n(\mathbf{k}) = \left(\exp\left[\frac{\tilde{\epsilon}(\mathbf{k}) - \zeta}{k_B T} \right] + 1 \right)^{-1}, \tag{2.84}$$

with the temperature and charge carrier number dependent chemical potential $\zeta(T, N_c)$. The sums over $\mathbf{k}_1$ and $\mathbf{k}_2$ can be interpreted as an scattering event from initial momentum $\mathbf{k}_1$ to final momentum $\mathbf{k}_2$. The probability for such an event is proportional to the occupation number $n(\mathbf{k}_1)$ of the state $\mathbf{k}_1$ times the probability of the final state $\mathbf{k}_2$ being empty $(1 - n(\mathbf{k}_2))$ which is also known as Pauli blocking. The sum index M occurs only in the exponentials which can be simplified to a Kronecker delta $\delta_{\mathbf{k}_1,\mathbf{k}_2}$, showing the momentum conservation for the coherent transport. This implies that $\tilde{\epsilon}(\mathbf{k}_1) = \tilde{\epsilon}(\mathbf{k}_2)$, which leads to an infinite mobility due to the time integral over t. However, this is expected for the coherent transport without any scattering mechanism. This is also in accordance with the quantum conductance formalism presented in the previous section since the intrinsic resistance of a quantum wire without defects is zero (cf. Eq. 2.36) and the current is only limited by the contact resistance. As the approach of this section does not explicitly take the contact interface into account and since there are always scatterers in real crystals, one can assume a dephasing time τ which renders the coherent mobility finite

$$\mu_{\alpha\beta}^{(coh)} = \frac{\sqrt{\pi} e \tau}{2N_c k_B T} \sum_{\mathbf{k}_1} n(\mathbf{k}_1)(1 - n(\mathbf{k}_1)) \tilde{v}_\alpha(\mathbf{k}_1) \tilde{v}_\beta(\mathbf{k}_1), \tag{2.85}$$

with the polaron band velocity

$$\tilde{v}_\alpha(\mathbf{k}) = \frac{1}{\hbar} \frac{\partial \tilde{\epsilon}(\mathbf{k})}{\partial k_\alpha}. \tag{2.86}$$

The second contribution to the total mobility is the phonon-assisted incoherent hopping transport

$$
\begin{aligned}
\mu_{\alpha\beta}^{(\mathrm{inc})} =& -\frac{1}{eN_c 2k_BT}\left(\frac{e}{\hbar}\right)^2 \sum_{L,M,N} R_{L,\alpha}\tilde{\epsilon}_{0,L} R_{N,\beta}\tilde{\epsilon}_{0,N} \\
&\times \frac{1}{N_\Omega}\sum_{\mathbf{k}_1,\mathbf{k}_2} e^{-i\mathbf{k}_1(\mathbf{R}_M+\mathbf{R}_N)} e^{i\mathbf{k}_2(\mathbf{R}_M-\mathbf{R}_L)} n(\mathbf{k}_1)(1-n(\mathbf{k}_2)) \int\limits_{-\infty}^{\infty} e^{(it/\hbar)[\tilde{\epsilon}(\mathbf{k}_1)-\tilde{\epsilon}(\mathbf{k}_2)]} \\
&\times \left\{\exp\left[-\left(\delta_0^M - \delta_L^M - \delta_{-N}^M + \delta_{L-N}^M\right)\sum_\lambda \Phi_\lambda(t) g_\lambda^2\right] - 1\right\} e^{-(t/\tau)^2} dt,
\end{aligned}
\tag{2.87}
$$

with $\Phi(t) = N_\lambda e^{i\omega_\lambda t} + (1+N_\lambda)e^{-i\omega_\lambda t}$. Note that these expressions have been simplified by restricting to optical phonons which are assumed dispersionsless ($\mathbf{q}$ independent).

As the el-ph coupling constants for the polymer P3HT are very large (cf. Sec. 3.2), there exists an approximation for Eq. 2.87 which becomes more and more accurate with increasing temperature. It is based on the fact that the exponential factor in Eq. 2.79 leads to a strongly reduced bandwidth compared to the pure electronic band. Hence, one approximates $\tilde{\epsilon}(\mathbf{k}_1) = \tilde{\epsilon}(\mathbf{k}_2)$. Accordingly, the Fermi distribution becomes a constant ($n_\mathbf{k} \to c$). This leads to the so-called Narrow Band Approximation[40]

$$
\mu_{\alpha\beta}^{(\mathrm{NBA})} = \frac{e_0(1-c)}{2\hbar^2 k_BT}\sum_L \mathbf{R}_{L\alpha}\mathbf{R}_{L\beta}\tilde{\epsilon}_L^2 \int_{-\infty}^{\infty} \exp\left[2\sum_\lambda \Phi_\lambda(t) g_\lambda^2\right] e^{-(t/\tau)^2} dt. \tag{2.88}
$$

Based on this approximation, one can apply further approximations to evaluate the mobility for two phonon modes analytically. The integrand $\exp\left[2g_1^2\Phi_1(t) + 2g_2^2\Phi_2(t)\right] e^{-(t/\tau)^2}$ with $\Phi_\lambda(t) = N_\lambda e^{i\omega_\lambda t} + (1+N_\lambda)e^{-i\omega_\lambda t}$ can be rewritten[47] in order to expand it into modified Bessel functions I_n

$$
\begin{aligned}
\mu \sim& \frac{\tilde{\epsilon}^2}{k_BT}\int_{-\infty}^{\infty} \exp\left[2g_1^2\Phi_1(t) + 2g_2^2\Phi_2(t)\right] e^{-(t/\tau)^2} dt \\
=& \frac{\tilde{\epsilon}^2}{k_BT}\int_{-\infty}^{\infty} e^{z_1\cos[\Theta_1(t)] + z_2\cos[\Theta_2(t)]} e^{-(t/\tau)^2} dt \\
=& \frac{\tilde{\epsilon}^2}{k_BT}\int_{-\infty}^{\infty} \sum_{n_1=-\infty}^{\infty} I_{n_1}(z_1) e^{n_1\Theta_1(t)} \sum_{n_2=-\infty}^{\infty} I_{n_2}(z_2) e^{n_2\Theta_2(t)} e^{-(t/\tau)^2} dt,
\end{aligned}
\tag{2.89}
$$

with $z_\lambda = 4g_\lambda^2\sqrt{N_\lambda^2 + N_\lambda}$ and $\Theta_\lambda(t) = \omega_\lambda t + i\frac{\hbar\omega_\lambda}{2k_BT}$. This integral can be evaluated analytically. By inserting Eq. 2.79 for the polaron transfer integrals and taking only $I_0(z_\lambda)$ as dominating order in the Bessel expansion into account, one receives

$$
\mu \sim \frac{\epsilon^2\sqrt{\pi}\tau}{2k_BT} \cdot e^{-2g_1^2(1+2N_1)} I_0(z_1) \cdot e^{-2g_2^2(1+2N_2)} I_0(z_2). \tag{2.90}
$$

The exponential terms originate from the band narrowing in Eq. 2.79, leading to lower mobilities at higher temperatures as the effective masses of the polarons increases with the number of coupling phonons N_λ. The leftover Bessel functions originate from the integral and increase with the temperature as more phonons are available to contribute to the hopping process. Hence, there are two competing processes which either decrease or increase the mobility.

The analytic results are further analyzed by assuming that $\hbar\omega_1 < k_BT$ and $\hbar\omega_2 \gg k_BT$. This allows for an investigation of soft phonon modes and high-frequency modes, respectively. For the first mode one can approximate $I_0(z_1) = e^{z_1}/\sqrt{2\pi z_1}$, which is valid for large z_λ. For the second mode, z_2 is close to zero as this mode is nearly unoccupied ($N_2 \approx 0$). Therefore, one can approximate $I_0(z_2) \approx 1$ leading to

$$\mu \sim \frac{\epsilon^2\sqrt{\pi}\tau}{2k_BT} \cdot e^{-2g_1^2 \tanh\left(\frac{\hbar\omega_1}{4k_BT}\right)} \sqrt{\frac{\sinh\left(\frac{\hbar\omega_1}{2k_BT}\right)}{4\pi g_1^2}} e^{-2g_2^2}. \tag{2.91}$$

This equation will be used in Sec. 3.2.4.1 to analyze the influence of different phonon modes.

2.7 Bonding analysis

As described in Sec. 2.4 about pseudopotentials, this work employs plane waves as basis set to expand the Kohn-Sham orbitals, which allows for an efficient and reliable control of the numerical convergence. Moreover, plane waves do not suffer from the basis set superposition errors occurring for bases formed from a finite number of localized atom-centered functions. However, they are delocalized and, thus, do not give immediate access to electron partitioning and bonding information. This is in contrast to an atomic orbital description of the electronic structure[48–51], where this information can be obtained in a more straightforward way. A bonding analysis can also be performed for plane-wave calculations by applying projection techniques[52–58].

One important bond analysis tool is the crystal orbital Hamilton population (COHP), proposed by Dronskowski and Blöchl[50] using a linear muffin-tin orbital (LMTO) approach. It has been identified as a successful bonding indicator for extended structures and is based on a rewriting of the band-structure energy as a sum of orbital pair contributions. Calculating the energy dependent COHP(E) diagram within a specified energy range allows for the identification of bonding, nonbonding and antibonding states in the band structure for selected bonds. Moreover, the total bond strength can be accessed by an energy integral of COHP(E).

A scheme to calculate COHP diagrams within plane-wave frameworks based on Blöchl's projector augmented wave method[59] has been proposed in Refs. 57 and 58. They offer also a free binary of their implementation (called `LOBSTER`) developed at the RWTH Aachen. The following methodology and own implementation is based on their published results and achieved a substantial speedup (several orders of magnitudes faster, cf. Fig. 2.9 in the next section) in the COHP calculation. This enormous improvement allows an application of the formalism also for large systems like the indium nanowires presented in Sec. 4. The remarkable speedup is achieved by making use of a rigorous application of the PAW formalism, presented in Sec. 2.4, and simplifications coming with norm-conserving pseudopotentials as will be described in the following.

According to Blöchl[50], crystal orbital Hamilton population is formally defined as

$$\begin{aligned}&\mathrm{COHP}_{\mu\vec{T},\nu\vec{T}'}(E) = \\ &\quad H_{\mu\vec{T},\nu\vec{T}'} \sum_{j,\vec{k}} f_j(\vec{k}) C^*_{\mu\vec{T},j}(\vec{k}) C_{\nu\vec{T}',j}(\vec{k}) \delta(\epsilon_j(\vec{k}) - E),\end{aligned} \tag{2.92}$$

where $C_{\mu\vec{T},j}$ denotes the expansion coefficient of the jth band in terms of the atomic orbital μ at the atomic position $\vec{T}$. $H_{\mu\vec{T},\nu\vec{T}'}$ are the matrix elements of the Hamiltonian in atomic orbitals, $\epsilon_j(\vec{k})$ is the eigenvalue corresponding to the jth electron state and $f_j(\vec{k})$ its occupation number. In extended systems, a frequently used bonding indicator are the off-site COHP quantities[50,56,57] with $\vec{T} \neq \vec{T}'$. Note that the occupation number in Eq. 2.92 may be omitted, e.g., for characterizing also the bonding character of conduction states. In plane-wave calculations, the expansion coefficients $C_{\mu\vec{T},j}$ are obtained by projecting the latter onto atomic orbitals in a postprocessing step. The choice of the atomic orbitals is thereby not unambiguously – one possibility are Bloch sums[60] $\chi_\mu(\vec{k})$ set up from contracted multiple-ζ Slater-type orbitals as suggested in Ref. 57. The all-electron (AE) PAW wave functions $|\phi_j^{\mathrm{AE}}(\vec{k})\rangle$ are projected onto such an atomic basis via

$$T_{\mu j}(\vec{k}) = \langle \chi_\mu(\vec{k}) | \phi_j^{\mathrm{AE}}(\vec{k}) \rangle \,. \tag{2.93}$$

Thereby the AE wave function $|\phi_j^{\mathrm{AE}}(\vec{k})\rangle = \mathcal{T}\,|\phi_j^{\mathrm{PS}}(\vec{k})\rangle$ is reconstructed from the PAW pseudo wave function $|\phi_j^{\mathrm{PS}}(\vec{k})\rangle$ as already derived in Sec. 2.4 using the transformation $\mathcal{T}$ (Eqs. 2.23 & 2.24)

$$\mathcal{T} = 1 + \sum_{\mu,\vec{T}} \left(|\Phi_{\mu\vec{T}}\rangle - |\tilde{\Phi}_{\mu\vec{T}}\rangle \right) \langle \tilde{p}_{\mu\vec{T}}| \,. \tag{2.94}$$

Here, $|\Phi_{\mu\vec{T}}\rangle$ and $|\tilde{\Phi}_{\mu\vec{T}}\rangle$ denote the all-electron and pseudo partial waves, respectively and $\langle \tilde{p}_{\mu\vec{T}}|$ the projector function. Thus, the atomic orbital projection formalism presented in Ref. 57 involves three distinct scalar products (indicated below) which have to be evaluated on different grids for accurate results

$$
\begin{aligned}
T_{\mu j}(\vec{k}) = {} & \overbrace{\langle \chi_\mu(\vec{k}) | \phi_j^{\mathrm{PS}}(\vec{k}) \rangle}^{(1)} \\
& + \sum_{\mu,\vec{T}} \underbrace{\langle \chi_\mu(\vec{k}) | \left(|\Phi_{\mu\vec{T}}\rangle - |\tilde{\Phi}_{\mu\vec{T}}\rangle \right)}_{(2)} \underbrace{\langle \tilde{p}_{\mu\vec{T}} | \phi_j^{\mathrm{PS}}(\vec{k}) \rangle}_{(3)} .
\end{aligned}
\tag{2.95}
$$

Especially the part including the sums becomes more and more time consuming with increasing system size as the number of scalar products increases with the number of orbitals μ. In order to reduce the number of scalar products to be evaluated, a different application of the PAW projection is used here. Instead of using contracted multiple-ζ Slater-type orbitals as atomic wave functions, the $|\Phi_{\mu,\vec{T}}\rangle$, already contained in the PAW pseudopotential, are utilized to set up the Bloch sums

$$
|\chi_\mu(\vec{k})\rangle = \frac{1}{\sqrt{N_{\vec{T}}}} \sum_{\vec{T}} e^{i\vec{k}\vec{T}} \, |\Phi_{\mu\vec{T}}\rangle . \tag{2.96}
$$

This approach requires pseudopotentials with atomic wave functions generated on a sufficiently large radial grid (the standard used in the `Quantum Espresso` pseudopotential database is large enough). As will be derived in the following, the use of the wave functions contained in the pseudopotentials in combination with norm-conserving pseudopotentials is an important key to drastically reduce the computational effort. Inserting Eq. 2.96 into Eq. 2.93 yields

$$
\begin{aligned}
T_{\mu j}(\vec{k}) &= \frac{1}{\sqrt{N_{\vec{T}}}} \sum_{\vec{T}} e^{-i\vec{k}\vec{T}} \, \langle \Phi_{\mu\vec{T}} | \phi_j^{\mathrm{AE}}(\vec{k}) \rangle \\
&= \frac{1}{\sqrt{N_{\vec{T}}}} \sum_{\vec{T}} e^{-i\vec{k}\vec{T}} \, \langle \tilde{\Phi}_{\mu\vec{T}} | \mathcal{T}^\dagger \mathcal{T} | \phi_j^{\mathrm{PS}}(\vec{k}) \rangle ,
\end{aligned}
\tag{2.97}
$$

where the $\mathcal{T}^\dagger\mathcal{T}$ transformation can be expressed as

$$
\mathcal{T}^\dagger\mathcal{T} = 1 + \sum_{\mu,\nu,\vec{T}} |\tilde{p}_{\mu\vec{T}}\rangle \underbrace{\left(\langle \Phi_{\mu\vec{T}} | \Phi_{\nu\vec{T}} \rangle - \langle \tilde{\Phi}_{\mu\vec{T}} | \tilde{\Phi}_{\nu\vec{T}} \rangle \right)}_{\Delta S_{\mu,\nu,\vec{T}}} \langle \tilde{p}_{\nu\vec{T}} | . \tag{2.98}
$$

With this reformulation, Eq. 2.97 can be solely evaluated on the Fourier grid using the pseudopotential specific constants $\Delta S_{\mu,\nu,\vec{T}}$, the pseudo wave functions $|\phi_j^{\mathrm{PS}}(\vec{k})\rangle$ (and $|\tilde{\Phi}_{\mu\vec{T}}\rangle$) and the projector functions $|\tilde{p}_{\mu\vec{T}}\rangle$. Strictly speaking, the whole projection evaluation is now rigorously based on information included in the pseudopotentials. An enormous speedup can be gained by taking advantage of the fact that all constants $\Delta S_{\mu,\nu,\vec{T}}$ vanish for norm-conserving PAW pseudopotentials. Hence, the projection scheme is reduced to a single scalar product of $|\tilde{\chi}_\mu(\vec{k})\rangle$ (containing the pseudo partial waves $|\tilde{\Phi}_{\mu\vec{T}}\rangle)$ with the pseudo wave function $|\phi_j^{\mathrm{PS}}(\vec{k})\rangle$. This makes the sum over the scalar products (2) and (3) in Eq. 2.95 obsolete, therefore saving an increasing number of scalar products with growing system size. The implementation presented in the next subsection is able to reduce the overall runtime for the COHP calculation by about 90 % for the indium nanowires (cf. Sec. 4) due to this property of norm-conserving pseudopotentials. This improvement enables the usage of the COHP bonding analysis as a standard post-processing tool for which the implementation is presented in the following section.

2.7.1 Technical Implementation in Fortran

The methodology described above was implemented as post-processing tool for the `Quantum Espresso`-package including an input file description and an user guide for other users. The application flow chart is depicted in Fig. 2.8. The starting point is the computation of the Bloch sums from the atomic pseudo wave functions $|\tilde{\Phi}_{\mu\vec{T}}\rangle$ (used as atomic orbitals (AO)), which yields a $\mathbf{k}$-dependent basis set (cf. first block in Fig. 2.8). In the next step, this basis set is orthonormalized to use it for the determination of the expansion coefficients[21] $\mathbf{C}(\mathbf{k})$.

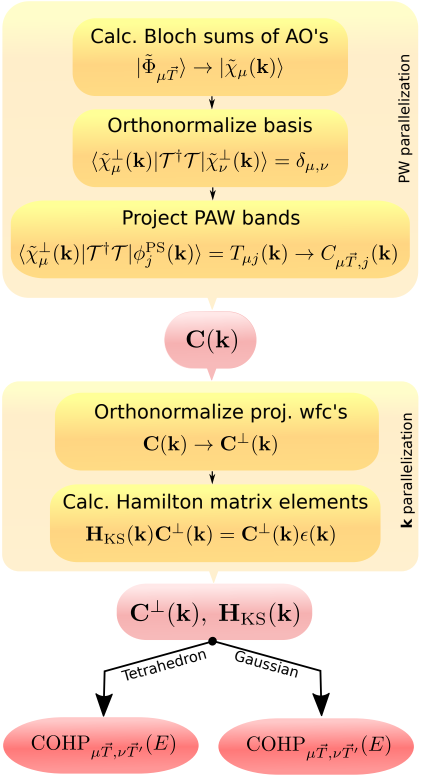
Calc. Bloch sums of AO's
$|\tilde{\Phi}_{\mu\vec{T}}\rangle \rightarrow |\tilde{\chi}_\mu(\mathbf{k})\rangle$
Orthonormalize basis
$\langle\tilde{\chi}_\mu^\perp(\mathbf{k})|\mathcal{T}^\dagger\mathcal{T}|\tilde{\chi}_\nu^\perp(\mathbf{k})\rangle = \delta_{\mu,\nu}$
Project PAW bands
$\langle\tilde{\chi}_\mu^\perp(\mathbf{k})|\mathcal{T}^\dagger\mathcal{T}|\phi_j^{\mathrm{PS}}(\mathbf{k})\rangle = T_{\mu j}(\mathbf{k}) \rightarrow C_{\mu\vec{T},j}(\mathbf{k})$
PW parallelization
$\mathbf{C}(\mathbf{k})$
Orthonormalize proj. wfc's
$\mathbf{C}(\mathbf{k}) \rightarrow \mathbf{C}^\perp(\mathbf{k})$
Calc. Hamilton matrix elements
$\mathbf{H}_{\mathrm{KS}}(\mathbf{k})\mathbf{C}^\perp(\mathbf{k}) = \mathbf{C}^\perp(\mathbf{k})\epsilon(\mathbf{k})$
k parallelization
$\mathbf{C}^\perp(\mathbf{k}),\ \mathbf{H}_{\mathrm{KS}}(\mathbf{k})$
Tetrahedron
Gaussian
$\mathrm{COHP}_{\mu\vec{T},\nu\vec{T}'}(E)$
$\mathrm{COHP}_{\mu\vec{T},\nu\vec{T}'}(E)$

Figure 2.8: Flowchart for the calculation of $\mathrm{COHP}(E)$.

Thereby, the application of Löwdin's symmetric orthonormalization procedure ensures that the wave function modifications are limited to a minimum[61]. The calculations are parallelized by the implementation which makes use of the Message Passing Interface (MPI). The scalar products calculated in the first steps in Fig. 2.8 are thereby parallelized over plane waves. Note that the calculation of the coefficients $\mathbf{C}(\mathbf{k})$ was not parallelized with respect to $\mathbf{k}$ points[22], as this would lead to considerable more random-access memory (RAM) needed for large systems. Nevertheless, once the $\mathbf{C}(\mathbf{k})$ are determined, there are no plane-wave dependent data to be processed anymore.

---

[21] $\mathbf{C}(\mathbf{k}) = C_{\mu\vec{T},j}(\mathbf{k})$ and $T_{\mu j}(\mathbf{k})$ differ only by a complex factor for orthogonalized basis sets (cf. Ref. 57 for more details).

[22] No usage of the standard "pool" parallelization of the `Quantum Espresso` package.

Hence, the following block in Fig. 2.8 makes use of an explicit efficient parallelization with respect to $\mathbf{k}$ points. This concerns the re-orthonormalization of the projected wave function – the orthonormality of the PAW bands might be lost due to the projection – and the calculation of the Hamiltonian matrix elements $\mathbf{H}_{\mathrm{KS}}$. Here $\epsilon(\mathbf{k})$ denote the Kohn-Sham eigenvalues from the density functional theory.

With respect to the used $\mathbf{k}$-point sampling, two ways were implemented to obtain the COHP quantity: The tetrahedron method[59,62] offers a highly accurate way to visualize the results, but needs at least four $\mathbf{k}$ points. As an alternative, especially for molecules, a Gaussian broadening visualization was also added.

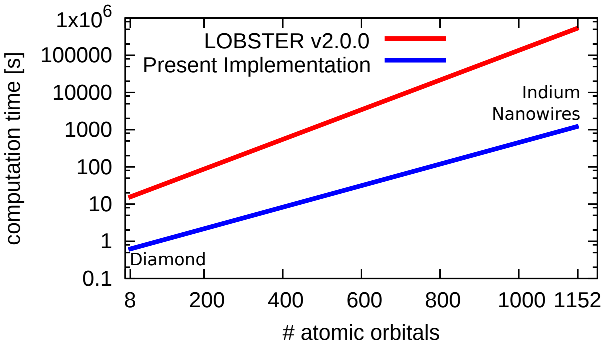

Figure 2.9: Computation time needed to determine a COHP diagram using `LOBSTER` and the present implementation for bulk diamond and indium nanowires with 8 and 1152 atomic orbitals, respectively (calculated on a single node with 24 cores; note the logarithmic scale).

The presented implementation and projection scheme was optimized in a way to offer best balance between memory consumption and speedup as the former limits the number of parallel processes per node for large systems. A comparison of the computation times between the presented implementation and the original projection scheme of Ref. 57 (`LOBSTER`) is made in Fig. 2.9. For the sake of comparability, both implementations were executed on a single compute node with 24 cores as `LOBSTER` makes solely use of Open Multi-Processing (OpenMP) parallelization which is restricted to shared memory. The computation time is evaluated for two systems, bulk diamond and the indium nanowires presented in Sec. 4.

As can be seen in Fig. 2.9, the present implementation is considerably faster than `LOBSTER`. The absolute as well as the relative speed difference between both implementations increases more and more with increasing number of atomic orbitals due to more and more saved scalar products in the present projection scheme. Moreover, one has to mention again that the present approach is not restricted to shared memory so that a further speedup can be achieved by using several nodes in parallel.

To answer the question how the results obtained with the present implementation compare with the ones from the `LOBSTER` code, a COHP calculation was performed for bulk diamond as a simple and well defined model system. For the present implementation, the DFT electronic structure is obtained by the `Quantum Espresso` package within the generalized gradient approximation in form of the PBE functional[13,14]. The Kohn-Sham orbitals are expanded in plane waves up to an energy cutoff of 400 eV and the Brillouin zone is sampled with a 23×23×23 tetrahedron grid.

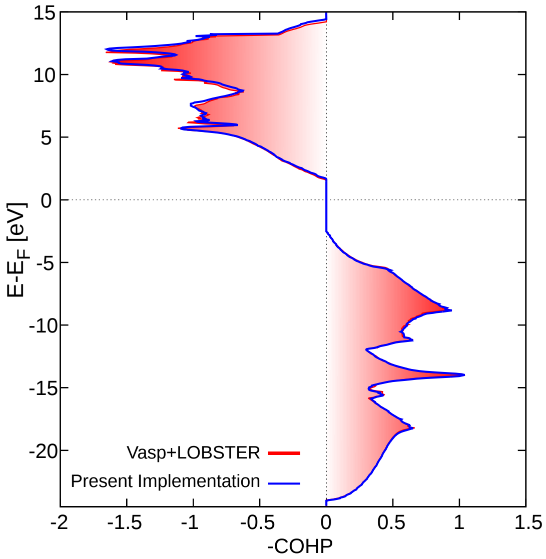

Figure 2.10: Chemical bonding results for a carbon-carbon bond in diamond with comparison between Ref. 57 (red) and the present implementation for the `Quantum Espresso` package (blue). Tetrahedron smearing is used in both cases to obtain smooth curves. Note that the x axis plots the negative COHP quantity to have antibonding left and bonding states right.

The COHP diagram is compared with the results of the `LOBSTER` program for which the electronic structure was obtained by the Vienna Ab initio Simulation Package (`VASP`) using the same convergence parameters. The results are in good agreement as can be seen in Fig. 2.10, although both programs use a different atomic basis set.

Negative and positive COHP values indicate bonding and antibonding contributions of electronic states within a specific energy interval. Hence, all occupied diamond valence states have a bonding contribution while the conduction states above the band gap are antibonding. Therefore, the present result suggests that doping or an electronic excitation will lead to a decreased carbon-carbon bond strength in bulk diamond.

3

Transport properties of Poly(3-hexylthiophene) (P3HT)

The first part of this work deals with the characterization of the *p*-type transport properties of the polymer Poly(3-hexylthiophene) (P3HT). P3HT belongs to one of the most studied organic semiconductors with various application, e.g., in field-effect transistors (FETs) as well as solar cells. To optimize these devices, it is very important to understand the transport limiting processes like disorder, imperfections and lattice vibrations in P3HT.

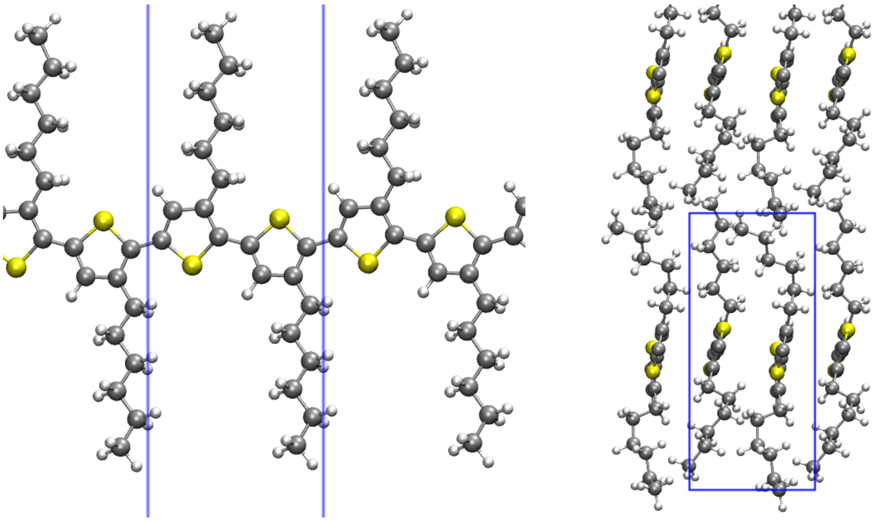

Figure 3.1: *Left:* P3HT single chain, *Right:* Model for a bulk P3HT crystal from side view with two monomers per unit cell (blue).

Fig. 3.1 depicts the structure of an ideal P3HT polymer chain on the left. It consists of thiophene rings in alternating transformation to which hexyl side chains are attached. Two adjacent thiophene rings and their hexyl side chains make up one P3HT monomer which can be stringed together to form a P3HT chain. These single chains can further be combined to a P3HT crystal - thereby the hexyl side chains interdigitate slightly. These interdigitated polymer layers are further stacked along the normal vector of the thiophene rings (interchain direction). Moreover, every second of these layers is shifted around one half of the unit cell size in intra-chain direction.

The conductivity of P3HT has been already addressed by numerous publications. It has been reported that high molecular weight (long continuous polymer chains) P3HT films show improved transport properties[63–66]. This has been associated with the efficient band transport in intrachain direction in these films[67], while for low molecular weight films hopping processes dominate. In addition, the conductivity in high molecular-weight polycrystalline P3HT films has been found to be highly anisotropic with a mobility parallel to the chains larger than perpendicular to them[68–70].

The transport characterization of P3HT is divided here into two parts: First, the influences of static disorder such as chain deformations, displacements and impurities like oxygen degenerations are analyzed with the help of the presented quantum conductance framework. Second, also dynamic effects like the interaction of charge carriers with phonons are considered to determine the temperature-dependent mobility of P3HT.

3.1 Influence of structural defects

In previous studies on the electronic properties of P3HT it has been found that the molecular electron and hole wave functions are delocalized over several thiophene rings. These wave functions can become spatially confined due to ring torsions and chain bendings[71–73] as well as fluctuations of the electrostatic potential caused by adjacent polymer chains[74].

When modeling different kinds of defects in P3HT, one has to keep in mind that the P3HT potential energy surface depends critically on the side chain formations, which have a significant influence onto ring torsions and chain bendings. Moreover, the system cannot be "downsized", e.g., by using bithiophene[75] as a simplified substitute, since this leads to other torsional angle distributions causing different atomic orbital overlaps. The related transfer integrals are very sensitive to torsional angles[69,76,77] so that such simplifications would severely influence the calculated transport properties. Hence, much attention is paid to a realistic modeling of the details of the molecular geometry within periodic boundary conditions. This is necessary to achieve an accurate solution of the scattering problem[35] based on the electronic structure obtained within density functional theory.

In this section several kinds of defects are investigated, thereby calculating the quantum conductance for various systems. The formalism used here and presented in Sec. 2.5, can in principle take moderate bias voltage effects into account by using different Fermi-levels in the contacts, thereby neglecting dissipative scattering effects. This restricts meaningful quantitative predictions to conditions with small bias but should not affect qualitative trends like the influence of, e.g., structural deformations onto the conductance. In particular, the systems analyzed in this section model the contacts as ideal, infinite P3HT polymers which offer strongly dispersive and well separated valence bands (cf. section 3.1.4). Therefore, p-type conductance suppressing bias voltage effects can be expected to be small.

Moreover, the approach used in this section is exclusively restricted to structural and electronic scattering centers as, e.g., inelastic scattering with phonons is neglected. Hence, temperature-dependent effects beyond thermal occupation of the one-particle levels according to the Fermi-Dirac statistics are not part of this section. However, to analyze also temperature-dependent effects, a different approach was used for which the results are presented in Sec. 3.2. Nonetheless, even without an explicit temperature treatment, the obtained results, e.g., for chain torsions are in excellent agreement with previous reports based on transfer integral calculations. Furthermore, the quantum conductance formalism is used to investigate defects which cannot that easily be described with transfer integral methods.

In this section, the density functional theory implemented in the `Quantum Espresso` package is used to calculate the ionic & electronic ground states for the following transport calculations. The wave functions are expanded in a plane-wave basis set up to an energy cutoff of 40 Ry. For the exchange & correlation functional the PBE parametrization [13,14] of the generalized gradient approximation (GGA) is used. Since dispersion interaction plays an important role in soft matter such as P3HT aggregates [78], the so-called DFT-D2 approach, i.e., a semi-empirical London-type correction term [79–81] with the parameters suggested by Grimme [27], is taken into account to obtain the correct ionic ground state. The Brillouin zone in polymer chain direction is sampled by 14 equidistant Monkhorst-Pack [82] $\mathbf{k}$ points for a single monomer while the $\mathbf{k}$-point mesh in the other directions and for larger unit cells is adjusted accordingly.

The results of this section are divided into four subsections to investigate the influence of layer displacements, torsions, bendings and oxygen degeneration separately. It starts with an offset between two P3HT layers since for this model it exists an analytic approximative description which illustrates the concept of the quantum conductance by means of a real system.

3.1.1 P3HT layer displacements

To start this chapter about quantum conductance in an illustrative way, a defective P3HT bulk crystal is used. The crystal is made of polymer strands which arrange in layers perpendicular to the thiophene rings. To model a dislocation, the distance between one layer pair is varied (cf. lower part of Fig. 3.2). Such displacements might be caused by defects embedded in the solid state matrix.

The upper part of Fig. 3.2 depicts the self-consistently calculated effective electron potential evaluated along a line marked in red.

To calculate the quantum conductance, one has to set up an arrangement of left & right contact as well as a scattering region (cf. Sec. 2.5). Ideal bulk P3HT unit cells are used as contacts which sandwich the scattering region that effectively contains three bulk P3HT unit cells with one displaced layer in the middle (cf. Fig. 3.2). After a self-consistent run for each region, the quantum conductance for the interchain direction (= stacking direction) can be evaluated. As the hole transport in P3HT occurs mainly in the valence band maximum (VBM), the following calculations are energetically determined for the VBM. The results are shown in Fig. 3.3 for varying layer spacings between two crystal layers in red.

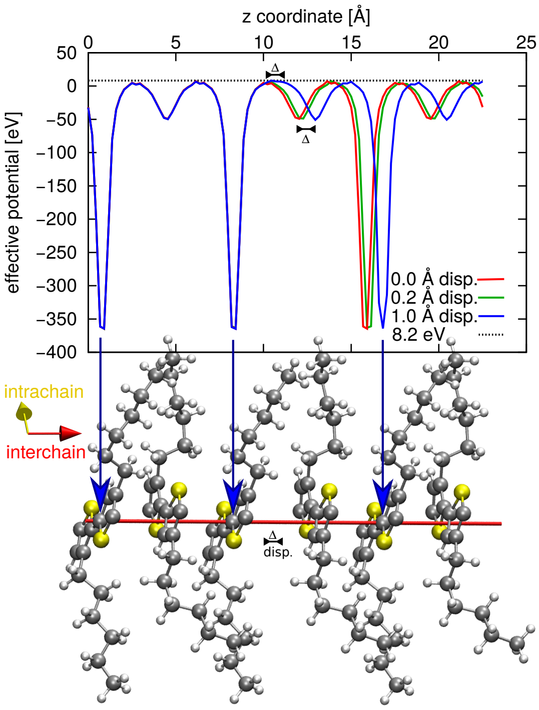

Figure 3.2: The effective electron potential (*top*) is calculated along a line through the thiophene rings for various displacements between two molecular layers (*bottom*).

As expected, the transmission follows a roughly exponential decay with increasing layer spacing caused by a reduced overlap of the molecular orbitals in transport direction. Notably, the conductance is reduced by about one order of magnitude already for displacements of 0.5 Å. Hence, it is expected that crystallographic defects, causing such a displacement, can dramatically reduce the cross-sectional area available for hole transport.

The results can be illustrated by thinking of the transport as a tunneling through the lattice spacing. This can approximately described by the Wentzel-Kramers-Brillouin

(WKB) approximation[83]

$$T = e^{-2\int_{z_1}^{z_2}\sqrt{\frac{2m}{\hbar^2}(V(z)-E)}dz}, \tag{3.1}$$

where the transmission is determined from a potential barrier $V(z)$ which separates the propagating modes with energy E in the left and right crystalline regions. For the sake of simplicity it is assumed that $V(z)$ is constant in the displaced region of length Δ and equal to the maximum of the self-consistently calculated value along the line depicted in Fig. 3.2. The mode's energy E is taken from the valence band maximum.

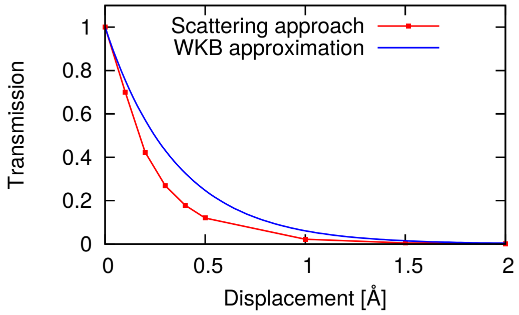

Figure 3.3: Quantum conductance perpendicular to the P3HT layers in dependence on the additional offset between two layers. Red: results of the full scattering approach. Blue: values obtained within the WKB approximation.

As can bee seen by the blue line in Fig. 3.3, this simple approximation describes the transmission dependence upon increased layer spacing in reasonable agreement with the more sophisticated scattering approach.

However, this simple approximation in Eq. 3.1 is not versatile enough to be applied to more complicated defects like chain torsions and bendings. Hence, after this illustrative example for the interchain transport, the scattering approach is exclusively used in the following to investigate the intrachain transport of P3HT in the next subsections.

3.1.2 Chain Torsions

It has been found by electrodeless conductivity measurements using charges produced by pulse radiolysis that conjugated polymer chains are characterized by large carrier mobilities ($\sim 10^3\ \mathrm{cm}^2/\mathrm{Vs}$)[84] which will also be confirmed by the temperature-dependent calculations in Sec. 3.2. However, due to conformational imperfections likely occurring in actual blends[85,86] as well as molecular impurities, e.g., by exposure to ambient conditions[87], the mobility may be drastically reduced from its ideal value.

Therefore, the following subsection addresses the influence of twisted P3HT chains onto the quantum conduction. The system's setup, to determine the transport properties along the structural defects, is shown in Fig. 3.4.

The scattering region consists of 6 P3HT monomers where the atoms of the outermost monomer on each side are kept fixed during the relaxation. This ensures that the

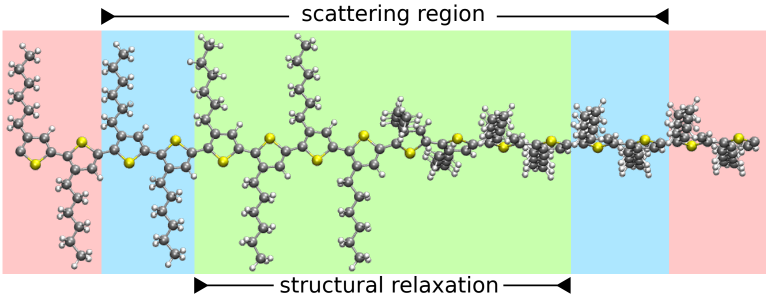

Figure 3.4: System setup for quantum conductance calculations across a chain torsion. Note that the atoms of the outer two monomers (shaded blue) of the scattering region are kept frozen during structural relaxation to guarantee a consistent structural interface between the scattering region and the ideal contacts. Moreover, two monomers outside the scattering region are added (shaded red) to decouple the torsion from its periodic images in the self-consistent calculations.

enforced overall torsion is not reversed by the relaxation. Furthermore, the fixing is necessary to have a continuous potential transition between contacts and scattering region.

Due to the employed periodic boundary conditions in the present calculations, one additional monomer is added on each side outside the scattering region, to improve the decoupling of the torsional defect from its periodic images. All in all the total region used in the self-consistent calculation contains 400 atoms in a cell which is about 63 Å long. After the electronic structure is determined, only the potential of the 6 innermost monomers is used for the transport calculations. The potential of the extra added monomers outside the scattering region is dismissed as they suffer most from the used periodic boundaries. To be able to calculate the quantum conductance only for a selected

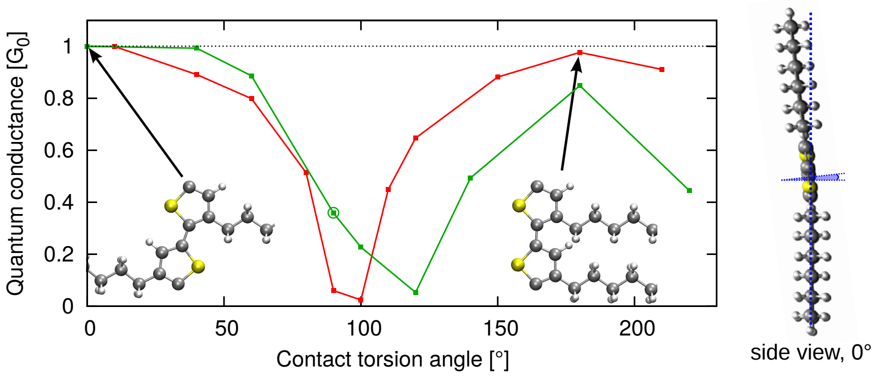

Figure 3.5: Calculated quantum conductance along single twisted thiophene-thiophene bonds (red) and configurations which distribute the total torsion angle over several thiophene-thiophene linkages due to structural relaxation (green). The geometries for zero and 180° rotation (indicated by arrows) are shown as insets, respectively. The encircled data point (90°) corresponds to the configuration shown in Fig. 3.8.

range, the available `PWCond` source code was extended by a suitable implementation. The extension allows for a combination of calculations with differently dimensioned systems for self-consistent field (scf) and transport calculations, respectively. This is especially necessary for scattering regions which offer no intrinsic periodic behavior, like the one in this subsection:

As a starting point, the torsion affecting only a single thiophene-thiophene bond is considered. Since the p-type conductivity of P3HT is governed by the states close to the VBM, it is expected that the transport results will strongly depend on the original shape of the valence band. This band corresponds to overlapping p_z orbitals of the thiophene rings that are perpendicular to the thiophene plane. This overlap of the p_z orbitals is directly affected by the torsion. Hence, one can expect a strong decrease of the quantum conductance with increasing torsion angle, as shown earlier by transfer integral calculations[69,76,77].

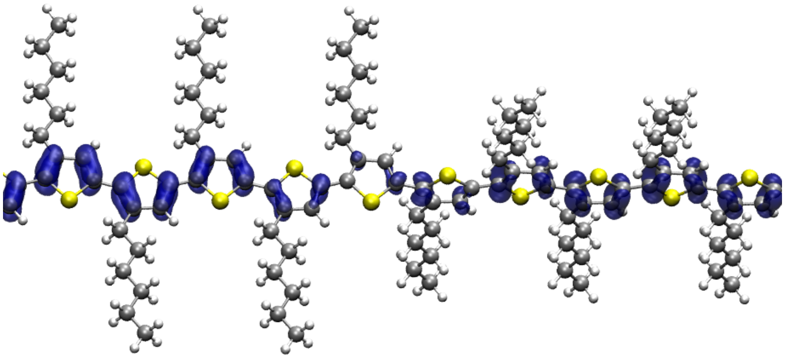

Figure 3.6: Depiction of a charge density isosurface of the highest valence band (HVB) for a structure with a 90° torsion between two thiophene rings.

The calculated quantum conductance through single twisted thiophene-thiophene bonds is depicted in Fig. 3.5 in red. It shows indeed a strong reduction with increasing twist angle. The curve offers thereby a pronounced minimum for square angles which expresses the fact that no delocalized π-bonds can be formed anymore. Beyond the vanishing orbital overlap directly at the twisted bond, one can also observe a fragmentation of the highest valence band (HVB) in the adjacency of the defect in Fig. 3.6. The results for a single twisted thiophene-thiophene bond (red) are more or less symmetric with respect to its minimum. The slight differences are caused by the fact that the 0° and 180° torsions are not identical configurations (cf. insets in Fig. 3.5). Additionally the angles 140° and 220° are not equivalent as the polymer is slightly bent (cf. side view in Fig. 3.5). The total energy as a function of a single twist angle (cf. red line in Fig. 3.7) shows this asymmetry more obviously.

In Fig. 3.7 a steep increase of the total energy for torsion angles exceeding 130° can

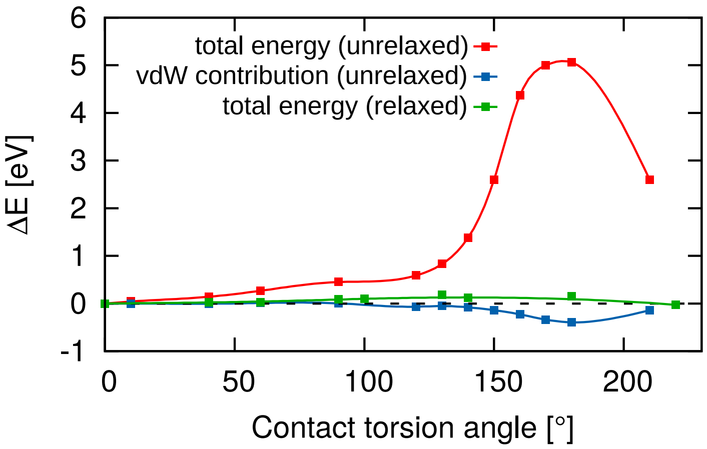

Figure 3.7: Bond twisting induced change in the total energy for the case that only a single bond is twisted (red) and for the configurations in which the torsion is realized by a sequence of twists (green). Dispersion contributions to the single bond twisting are shown in blue.

be observed (red curve). This effect is caused by the steric repulsion of the hexyl side chains which is not compensated by attractive van der Waals (vdW) forces (blue curve in Fig. 3.7). The green curve shows the total energy for polymer geometries resulting from structural relaxations where the overall torsion angle is enforced by fixed outer two monomers. The relaxation distributes the overall twisting angle over all freely moving monomers, which models a chain that is not constrained by the surrounding polymer matrix. Moreover, the hexyl side chains can evade each other to reduce the steric repulsion. An example of such a relaxed structure is depicted in Fig. 3.8.

Both energy curves (red and green) exhibit a very shallow increase at small torsions in Fig. 3.7 which suggests angles of about 20° due to thermal activation at room temperature if the chain motion is not strongly constrained otherwise. This result is in accordance with previous molecular dynamic simulations[88].

Since the red conductance curve in Fig. 3.5 suggests that only torsions larger than about 60° affect the polymers conductance in an appreciable way, one can suppose that the conductance decrease will be less severely if the overall torsion is distributed from one single bond to several ones, making up a sequence of twists. Therefore, by determining also the quantum conductance for the relaxed structures, a remarkably difference to the corresponding curve for single bond twists is found, cf. green curve in Fig. 3.5. One can see that the conductance drop at small angles is reduced and its onset is shifted to larger angles. Moreover, the minimum of the transmission curve has shifted from nearly square angles to about 120°. These findings can be explained with the angle distribution depicted in Fig. 3.8 as inset. It can be seen that the maximum angle between adjacent thiophene rings is usually much smaller than the

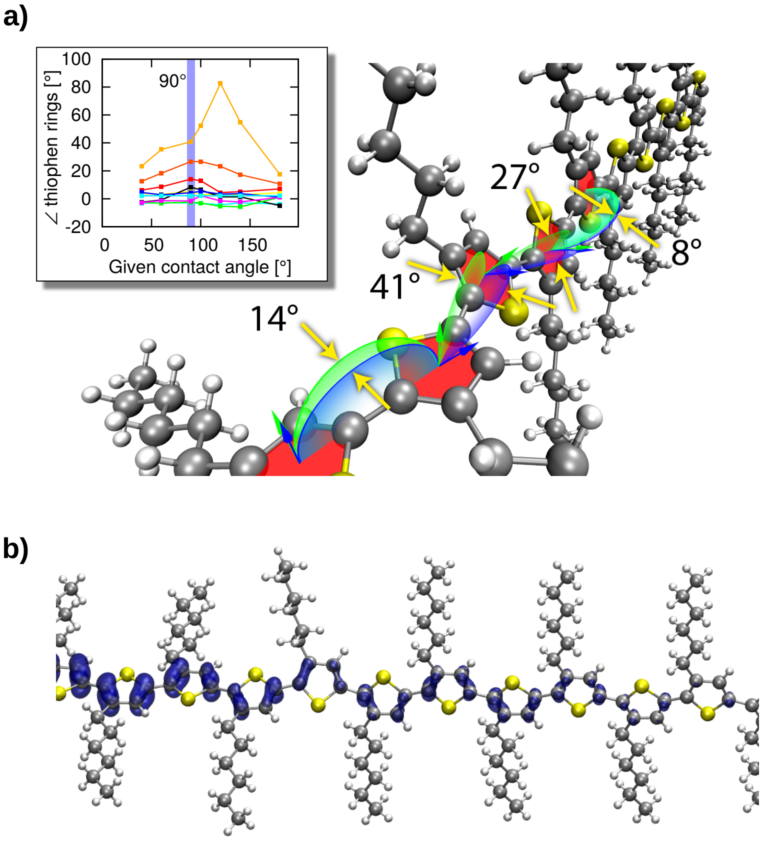

Figure 3.8: a) Relaxed atomic structure for an overall torsion angle of 90° forced by the fixed boundary monomers. The resulting twist angles between adjacent thiophene rings are highlighted. The data point, belonging to the calculated quantum conductance for this configuration, is marked with a circle in Fig. 3.5. The inset depicts the twist angle distributions calculated for various torsions. b) Visualization of the HVB by an isosurface overlaying the same structure as above.

enforced total torsional angle. For instance, for the 90° case the maximum twist angle between two adjacent thiophene rings is 41° (cf. Fig. 3.8**a)**). This leads still to a slight delocalization of the wave function along the polymer chain, which results into a larger transmission than in the case, where a full 90° torsion is located on one bond (cf. Fig. 3.5). However, for total torsions as large as 120°, maximum twist angles of about 83° occur in the relaxed structure which quenches the conductance severely due to the vanishing overlap of the carbon p_z orbitals and a strongly fragmented highest valence band (cf. fragmentation in Fig. 3.8**b)** for a total torsion of 90°). Therefore, both findings can be well rationalized by an analysis and comparison of the atomic configurations.

Since the atoms of the inner monomers are allowed to move freely, the overlap across thiophene-thiophene linkages might not only be reduced by a torsion. A possible additional interference might arise from an out-of plane movement of linking carbon atoms which would cause sp^3 hybridized configurations. An analysis showed a maximum out-of plane movement of about 0.04 Å which can be expected to have a subsidiary influence estimated from results of the following subsection 3.1.3 (chain bendings).

One might calculate the product of the transmission coefficients determined for single twists as an approximation to the transmission through a complete chain including several torsional defects. This is though only a rough approximation as, e.g., the product of the transmission coefficients for the relaxed 90° case is about twice as large as the transmission coefficient obtained by solving the complete scattering problem of this structure, cf. encircled data point in Fig. 3.5. The difference might be related to the fact that in case of extended defects, the HVB is much stronger fragmented and interrupted than one might expect (cf. Figs. 3.6 and 3.8 **b)**). This additional fragmentation effect cannot attributed for by simply analyzing only the angles between next-nearest neighbors. Therefore, the approximation mentioned above provides only an upper limit for the transmission. This has to be kept in mind when performing common transfer integral approaches for such kinds of complex deformation patterns: Only in case of single confined twists one can attribute the reduced charge transfer solely to the narrowed orbital overlap between neighboring thiophene rings.

One has to mention that the present total energy calculations depicted in Fig. 3.7 suggest that the minimum energy configuration for a fixed overall torsion angle is given by a sequence of single twists of similar angles, i.e., a helix configuration. To confirm this assumption, the total energy for such an atomic configuration was calculated for comparison with the results shown as green curve in Fig. 3.7. Thereby it was found that the energy gain upon helix formation is small, as it is only of the order of a few meV. Moreover, the formation of such regular structures will in general be prevented by the surrounding P3HT matrix, e.g., resulting in chain bending.

3.1.3 Chain Bending

A common defect in P3HT next to chain torsions is the polymer chain bending[89]. To model this defect, several folded P3HT chains were analyzed and characterized by the respective minimum curvature radius along the polymer chain. The geometric setups are structurally relaxed, whereas the atoms of the inner 5 monomers (250 atoms) are free to move and the outer 2 monomers are kept frozen. An example of such a polymer geometry is shown in Fig. 3.9.

It is found that structures characterized by small curvatures are rather regular with straight and ordered hexyl side chains. With increasing curvature additional disorder including torsional defects is observed, see Fig. 3.9.

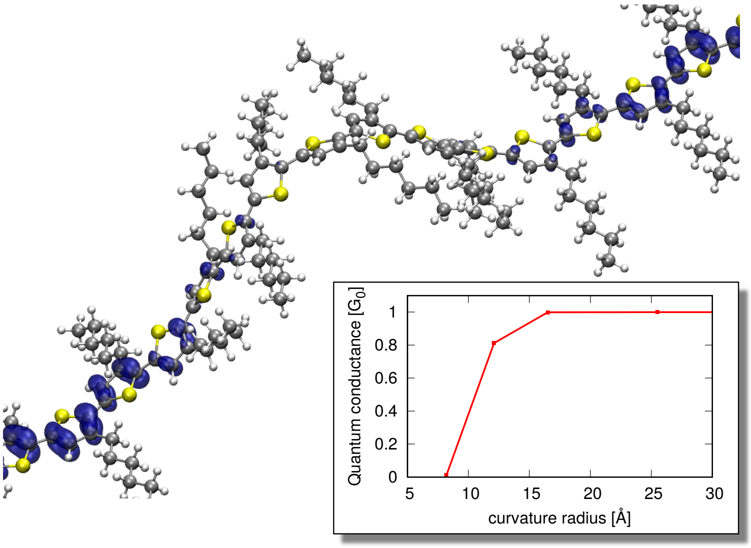

Figure 3.9: A relaxed bended chain with a minimum curvature radius of 8 Å. The HVB is indicated by a blue isosurface. The quantum conductance in dependence on different curvature radii is shown in the inset.

The quantum conductance results are shown in the inset in Fig. 3.9. It is remarkably that the conductance stays nearly unaffected by the structural deformations for curvature radii larger than about 17 Å. This can be attributed to an observed very efficient local relaxation mechanism which smooths the polymer structure, thereby preventing sharp kinks which would drastically influence the overlap between adjacent carbon p_z-orbitals. Moreover, the chain bending is less serious than the chain torsions as the former leads to an overlap decrease/increase on opposite polymer sides.

Nevertheless, the calculated conductance is strongly quenched for small curvature radii which can be expected to arise, e.g., when two polymer chains cross each other. In Fig. 3.9 one can also observe bond twists (in addition to the bending) caused by structural relaxations in response to hexyl side chain related strain. This critical influence of the hexyl side chains onto the backbones planarity has already been pointed out in Ref. 86. Therefore, one can define a curvature radius of about 12 Å as critical chain bending similar to the 60° angle found for chain torsions. In addition, similarly as observed for torsion patterns, a HVB fragmentation can be seen upon bending in Fig. 3.9 (shown for a 8 Å curvature radius).

3.1.4 Isomer defect

So far, only regioregular head-to-tail P3HT (rr-HT-P3HT) was investigated since this isomer is of particular interest for organic semiconductor devices due to its large carrier mobility. The identifier head and tail refers to the coupling between two thiophene

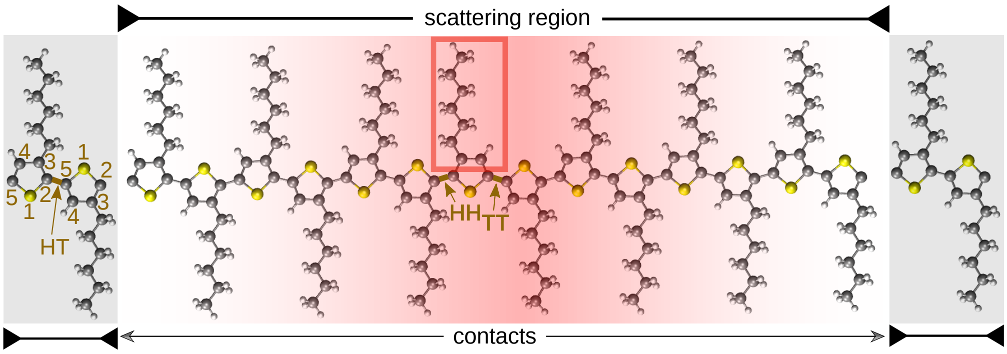

Figure 3.10: Setup to determine the transport across an isomer defect. The defect consists of a so-called HH-TT linkage between the thiophene rings which is caused by a swapped position of a hexyl side chain (red rectangle). The contacts are made of ideal regioregular HT-P3HT. In the left contact the atomic numbering is indicated. H denotes the second and T the fifth position.

rings where H denotes the second and T the fifth position on the ring, with numeration starting at the sulfur atom as shown in Fig. 3.10. The numeration direction is chosen in the way that the hexyl side chain is at the third position (poly-$\underline{3}$-hexyl-thiophene).

The influence of an isomer defect onto the transport properties can, e.g., be investigated by changing the position of the hexyl side chain as depicted in Fig. 3.10. This leads to a head-to-head (HH) and tail-to-tail (TT) coupling aberrant from the ideal head-to-tail (HT) connection. Thereby ideal head-to-tail P3HT (HT-P3HT) monomers are used to contact the isomer defect. As done for the other quantum conductance calculations, additional HT coupled P3HT segments are included in the scattering region, in order to allow for a realistic modeling of the geometric and electronic environment of the defect embedded in the polymer.

The resulting quantum conductance across the isomer defect (red) is compared in Fig. 3.11 with the quantum conductance of an ideal P3HT chain (blue line in the middle of the left figure). The latter can easily be obtained by Eq. 2.72, which reduces the calculation to a counting of the number of bands at a given energy (cf. blue band structure on the left-hand side in Fig. 3.11).

Since the holes will almost exclusively move at the Fermi edge in the p-type conducting P3HT, a maximum quantum conductance of $1\ G_0 = \frac{2e^2}{h}$ is found for a single, ideal (HT)-P3HT chain.

Figure 3.11 depicts also the electronic band structure (green and orange) for two scattering regions used for the transport calculation in intrachain direction (Γ–X), only differing by the number of ideal HT-P3HT monomers included. Note that the green curve thereby exhibits several small gaps between the bands at the Γ and the X point in the Brillouin zone (exemplary marked with red circles). However, these gaps are not

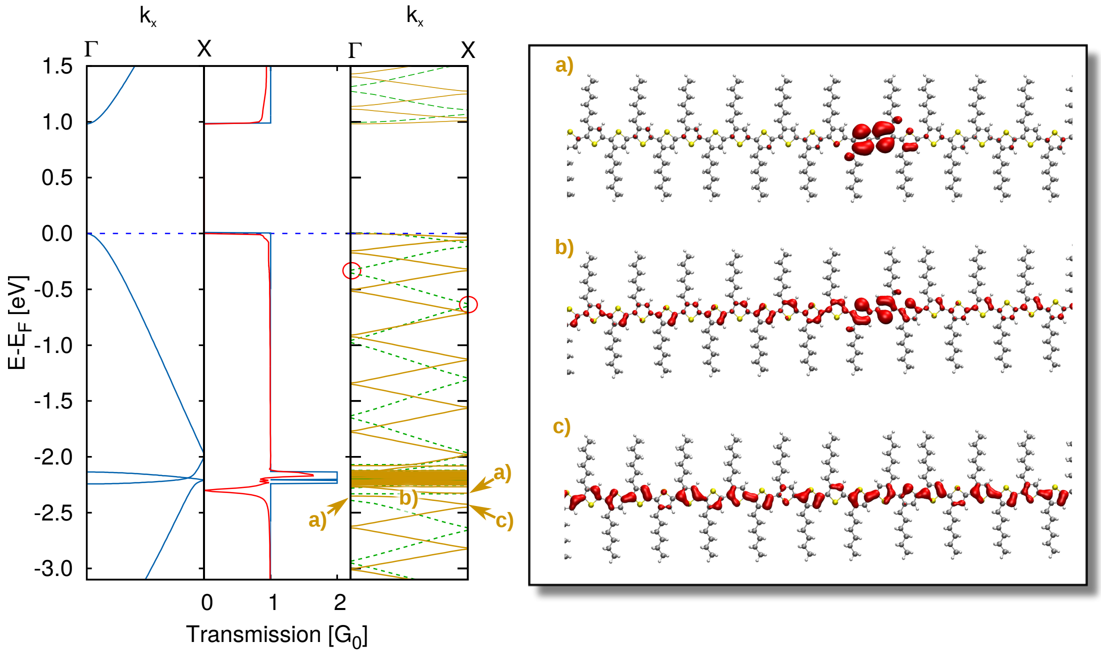

Figure 3.11: *Lhs, left part:* Band structure of rr-HT-P3HT (blue) in intrachain direction. *Lhs, middle part:* Ideal quantum conductance for rr-HT-P3HT (blue) compared to calculations for a single isomer defect shown in Fig. 3.10 (red). *Lhs, right part:* Band structure of the scattering region used for the transport calculation (green) and a second region extended by additional two contact monomers on each side (orange). *Rhs:* Orbital character of selected states labeled a), b), and c) in the right band structure on the left hand side.

reflected by the red transmission curve. This can be understood if one remembers the setup for the quantum conductance calculation. The transmission is determined for a system consisting of a single defective scattering region, surrounded by semi-infinite, ideal contacts. In contrast to this, the band structure of the scattering region belongs to a periodically repeated defect. One can decrease the influence of the periodicity by increasing the distance between two defects by including additional ideal contact monomers in the scattering region. For instance, the orange band structure includes two ideal monomers on each side more than the green one. As this scattering region comes closer to the actual transport system, the orange curve matches better the red transmission results, i.e., the gaps are smaller and will disappear in the limit of infinite contacts.

The red transmission curve in Fig. 3.11 on the left shows a small defect induced conductance reduction close to the Fermi edge. Apart from that only for energies at about 2.3 eV below the valence band maximum a notable drop occurs due to the isomer defect. This conductance modification is far below the hole transport channel at the VBM and will therefore barely affect the charge carrier transport. Nonetheless, it is interesting to clarify the physical origin of this striking, sharp drop. The right part of Fig. 3.11 shows that the effect is related to a strong wave function localization at the defect for this special energy. The localization changes from strongly localized (close to the defect, cf. Fig. 3.11 **a)**) via an intermediate localization (Fig. 3.11 **b)**) to delocalization along the whole thiophene chain (Fig. 3.11 **c)**) depending on the energy.

Nevertheless, as already mentioned above, the isomer defect has only minor influences onto the transport properties which confirms that the P3HT conductance is mainly determined by the thiophene rings rather than the hexyl side chains. This weak impact onto the electronic properties is also desirable as the hexyl side chains are usually intended to improve the processing properties of polythiophene[90] exclusively.

In summary, in this subsection it is found that the conductance is relatively robust with respect to isomer defects. However, such defects affect the bulk morphology[91] and increase the disorder in the material. Hence, even if such isomer defects have only minor direct influence onto the quantum conductance, they might attract other defects which more strongly influence the electronic performance of the polymer.

3.1.5 Oxygen impurities

The previous subsections investigated the influence of structural defects onto the quantum conductance of P3HT. To analyze also the impact of impurity atoms, several types of oxygen degenerations are modeled. Such defects might originate from an unintentionally exposure to ambient atmosphere and aging. Thereby O_2 can undergo chemical reactions forming covalent bonds with the carbon and sulfur atoms of P3HT[92]. The formation of R-SO_x and R-COOH compounds has been detected experimentally by X-ray photoelectron spectroscopy[93]. This has a serious impact onto the charge

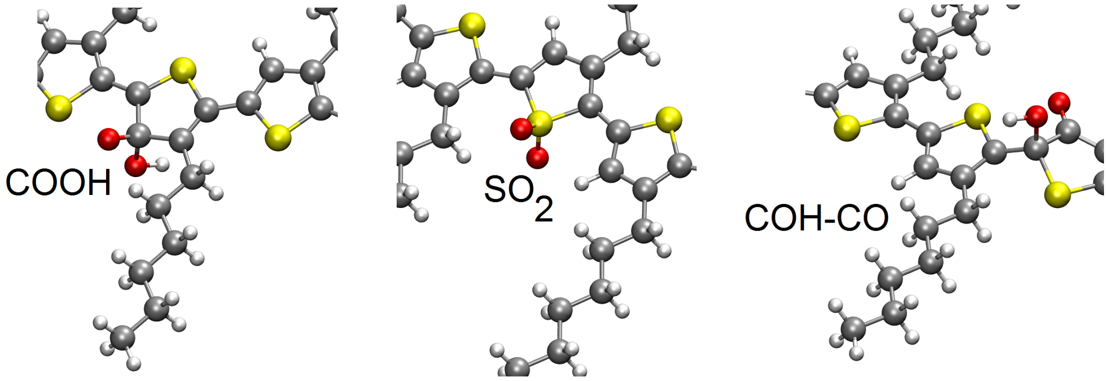

Figure 3.12: Three investigated oxygen impurities in P3HT. The COOH and SO_2 defects have been identified by Ref. 87 as stable oxygen-chemisorbed structures while the additionally investigated defect labeled COH-CO turns out to be even more stable. This defect has a stronger influence onto the geometry than the other two since the OH molecule pulls the attached carbon atom out of the thiophene ring plane.

defect	infinite chain DFT-D2	molecular crystal DFT-D2	 LDA
2 SO	0.89	0.80	1.30
COOH	2.01	2.16	2.85
SO_2	2.39	2.53	2.44
COH-CO	2.91		
R-COOH	3.17		

Table 3.1: Calculated binding energies (in eV, with respect to gas phase O_2) for various defect configurations. The results are compared with the values obtained for molecular crystals in Ref. 87.

carrier mobility and organic solar cell efficiency which have been found to decrease when P3HT is simultaneously exposed to light and oxygen[94–99].

As depicted in Fig. 3.12 three different kinds of oxygen adsorptions are investigated. The notation follows the one of Ref. 87 which identified the two defects “SO_2” and “COOH” as stable oxygen-chemisorbed structures by molecular dynamic (MD) simulations. Additionally, a further alternative labeled COH-CO in Fig. 3.12 is investigated here, which turns out to be even more stable (by about 0.5 eV) than the structures found in Ref. 87. The binding energies of all investigated oxygen defects are tabulated in Tab. 3.1 on the left where they are compared with Ref. 87 on the right.

The higher stability of the COH-CO defect results from a double bond formation

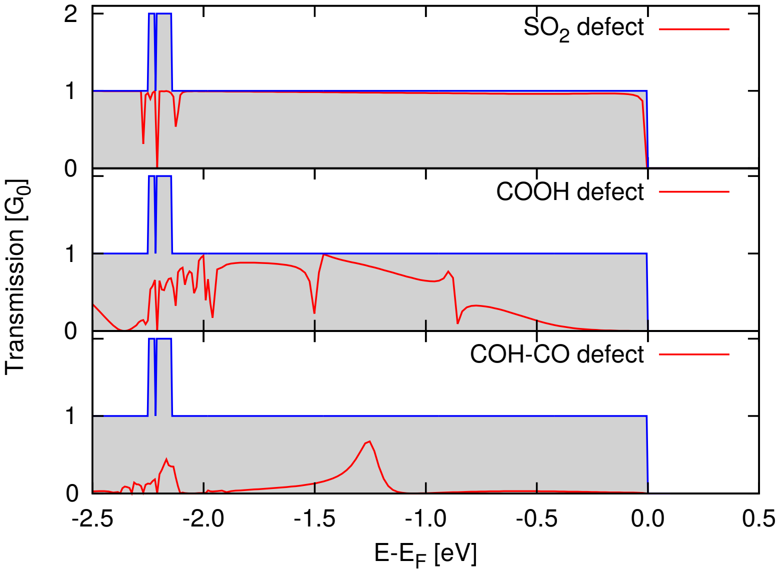

Figure 3.13: Transport results for a SO_2 (*top*), a COOH (*middle*) and a COH-CO defect (*bottom*). The shaded region is the maximum possible quantum conductance for rr-HT-P3HT (cf. previous subsection 3.1.4).

between the carbon and oxygen and a notably relaxation of the connected thiophene ring and its neighborhood. Thereby it is found that the COOH defect distorts the affected thiophene ring structure only slightly while the OH molecule pulls the bound carbon atom away from the ring plane in the more stable COH-CO defect. This results into a sp^3 hybridized configuration accompanied by a 34° kink in the polymer plane, leading to a kind of local chain bending (cf. subsection 3.1.3).

Following the system setup of the previous sections, the influence of the various oxygen related defects onto the charge transport properties are determined for a defective scattering region of 6 monomers sandwiched between ideal rr-HT-P3HT contacts. The obtained quantum conductance for all defects is shown in Fig. 3.13. Note that the gray shaded area indicates the conductance of an ideal P3HT chain. Thereby it becomes obvious that the defects differ strongly in their impact onto the transport properties. Similar to the isomerism defect, the SO_2 impurity barely influences the transport. Only around 2.2 eV below the VBM sulfur related conduction channels are broken. The COOH and COH-CO defects in contrast behave remarkably different as they significantly reduce the quantum conductivity over a broad energy range. Especially the transport through a chain with a COH-CO defect is nearly completely quenched. Only around 2.2 eV and 1.3 eV below the VBM residual channels of minor transmission are found. An almost as strong quenching of the hole transport is also observed for the planar COOH, though it is mainly restricted to about 0.8 eV below the VBM. This defect

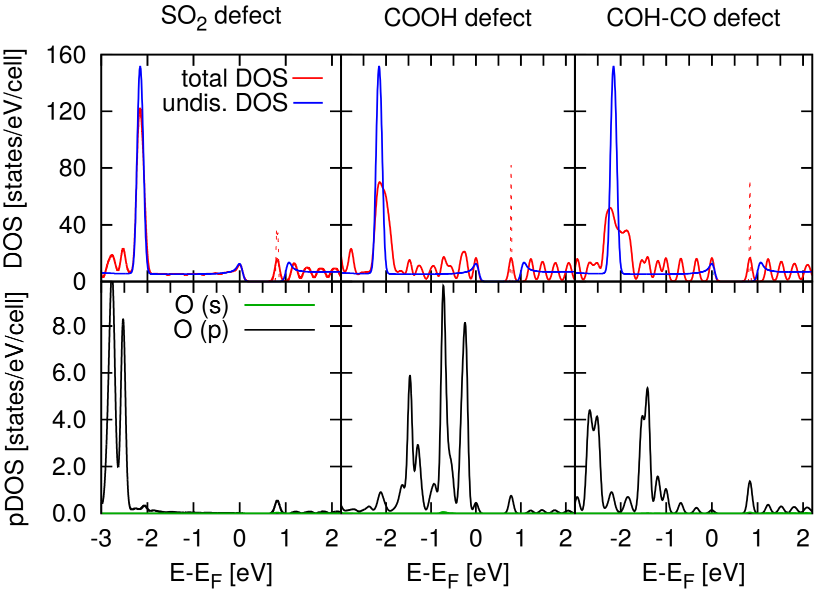

Figure 3.14: *Top:* Density of states calculated for chains containing oxygen impurities (gap states highlighted with dashed lines) in comparison to the pure P3HT polymer. *Bottom:* pDOS projected onto the *s* (green) and *p* (black) states of the two oxygen atoms. The *s* contribution is negligible in the investigated energy range.

causes also a sharp drop of the conductance at around 1.5 eV below the VBM. This effect is similar to the case analyzed for the isomer defect (cf. Fig. 3.11) as this drop is also induced by a charge carrier localization which is caused by the p electrons of the impurity O atoms (see also Fig. 3.14).

The observed different behavior of the SO_2 defect on the one hand and the defects attacking the thiophene carbon atoms on the other hand can be explained by an analysis of the density of states (DOS) and projected density of states (pDOS). All considered oxygen impurities have in common that they induce electronic states in the upper half of the gap which is indicated by dashed lines in the DOS in the upper part of Fig. 3.14. Apart from that and small oxygen-localized p states below -2.4 eV, the SO_2 DOS nearly matches the respective calculations for the ideal polymer. This is in large contrast to the much stronger deviations in the case of the COOH and COH-CO impurities. These defects show a widely modified valence band DOS along with additional oxygen p states. This large contrast is though expected as the P3HT valence band is formed by p_z orbitals of the conjugated chain which is little influenced by adsorption to the sulfur, but heavily affected by a direct oxidation of a thiophene group carbon atom. Hence, the latter have a major influence onto the transport in the valence band.

Moreover, in Fig. 3.15 a strong HVB fragmentation at the position of the oxygen impurity can be observed, extending over almost two monomers for the COH-CO defect.

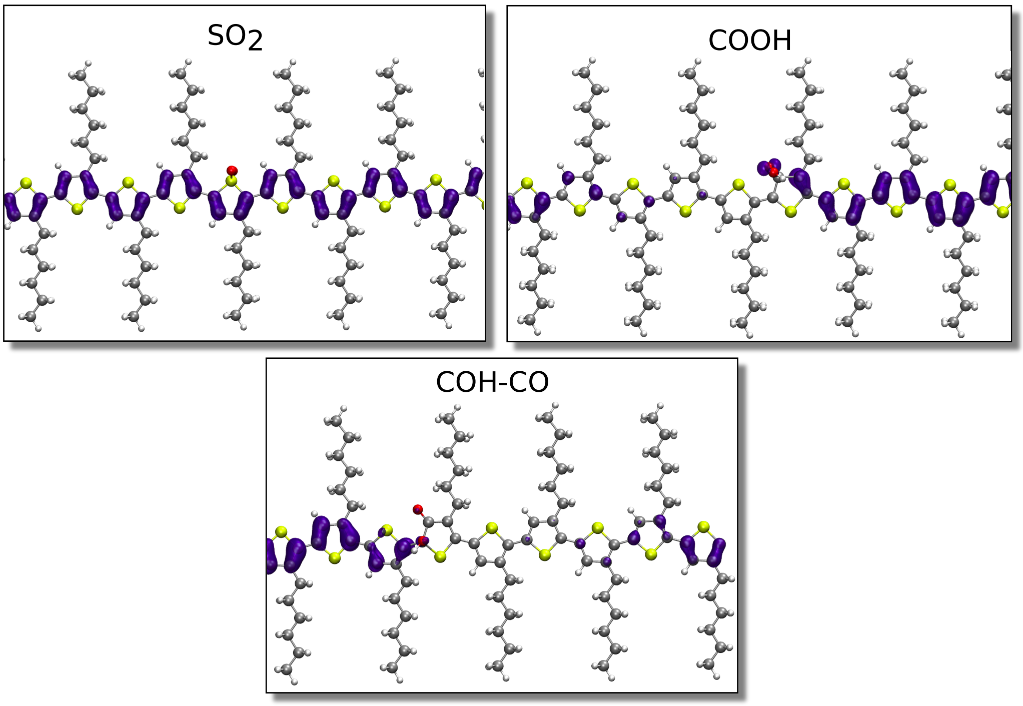

Figure 3.15: HVB indicated as isosurface for the three investigated defects.

Note that this observed fragmentation is not restricted to the HVB and leads to a dramatic reduction of the quantum conductance over a broad energy range.

This localization can be evident in varying degree, depending on the structural perturbation of the polymer chains, which also explains differences in the transport properties of the COOH and the COH-CO defect. Since the COH-CO defect is located at two thiophene ring carbon atoms and leads to a noticeable local chain bending, it lowers the conductivity along the chain most efficiently among all investigated impurity defects. Fig. 3.13 shows that the COH-CO defect blocks the hole transport nearly completely for an energy window extending several eV below the Fermi level.

This section dealt with the influence of static defects like disorder and impurities onto the coherent quantum conductance. Another application of the used transport formalism are interfaces between different compounds like P3HT and Phenyl-C61-butyric acid methyl ester (PCBM) which is a typical material combination in organic solar cells[100]. The p-type conducting polymer P3HT creates electron-hole pairs upon absorption of light and transfers the electrons to the PCBM. The hybridized state between P3HT and PCBM is expected to be decisive for the required fast transport through the interfaces[101]. We have still work in progress to model the interface as a scatterer, using the results of the quantum conductance formalism as a measure for the quality of the interface.

Since temperature-dependent effects play also a crucial role for technical applications, the next section makes use of a different approach to determine a temperature-dependent mobility. The mobility μ is linked to the specific conductance via $\sigma = qn\mu$ where q is the charge and n the charge carrier concentration[1]. Note that the gained results for the influence of static disorder and impurity effects in the last section can be expected to remain important at room temperature since the identified modifications of the HVB will affect the mobility strongly. This is supported by the results of the following section which clearly show a strong influence of phonon modes which deform the HVB.

---

[1] G and σ are linked by a factor depending on the geometry of the conductor - e.g., $G = \sigma \cdot A/l$ for a homogeneous conductor with constant cross section A and length l.

3.2 Temperature-dependent hole mobility of P3HT

Several studies attacked the temperature influence onto the transport properties of P3HT which is mainly characterized by the influence by phonons. Therefore, molecular dynamic simulations have been performed to analyze the structure and transfer integrals[102–105]. Another approach is to fit analytical expression to experimental conductivities, extracting physical quantities from the gained models parameters. A model, which is often used, is based on one effective vibration and the associated phonon frequency and electron-phonon (el-ph) coupling constant, cf. Refs. 64,106 & 107. Another approach is called mobility edge model which accounts also for disorder effects by separating the density of states into immobile (trapped) and mobile states to reproduce experimental data[108–110] with fitted parameters. This method is able to give first indications of the maximum intrinsic carrier mobilities of P3HT films with a much fewer number of traps than experimental realizable today. Nevertheless, theoretical models, relying on fits to experimental data, suffer from the difficulty to separate the respective influence of disorder and intrinsic polaronic effects on the mobility[111]. Therefore, this work takes a different approach: Instead of relying on fits to experimental data, the polaronic effects in an idealized P3HT crystal are analyzed by a *first principles* tight-binding description (cf. Sec. 2.6). The required material parameters including all optical phonon frequencies and electron-phonon coupling constants are obtained from density functional theory (DFT), which is described in the following in more detail.

3.2.1 Tight-binding band structure

The density functional theory implemented in the Vienna Ab initio Simulation Package (`VASP`) is used to calculate the required material properties like phonon frequencies & patterns, el-ph coupling constants and transfer integrals for an idealized P3HT crystal with one monomer (50 atoms) per unit cell from ab initio. The crystal structure depicted in Fig. 3.16 makes use of periodic boundary conditions and is based on the results of Ref. 78. The technical parameters are chosen in accordance with the previous section: Wave functions are expanded in a plane-wave basis set up to an energy cutoff of 400 eV. The

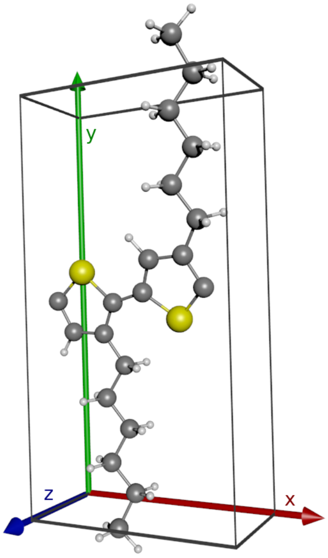

Figure 3.16: P3HT monomer in its unit cell.

exchange & correlation functional is given by the GGA in form of the PBE parametrization[13,14]. Dispersion interaction is again taken into account by the so-called DFT-D2 approach, i.e., a semi-empirical London-type correction term[79–81] with the parameters suggested by Grimme[27]. Since P3HT bulk is considered in this section, the 3D Brillouin zone is now sampled by an equidistant Monkhorst-Pack[82] $\mathbf{k}$-point mesh with 16 $\mathbf{k}$ points in interchain direction ($\mathbf{z}$), 8 in intrachain ($\mathbf{x}$) and 4 $\mathbf{k}$ points along the hexyl side chain direction ($\mathbf{y}$) (cf. axes labels in Fig. 3.16).

The P3HT band structure in intrachain direction is depicted in Fig. 3.17, left. The highest valence band offers a large dispersion which is responsible for the hole transport in P3HT. To determine the tight-binding material properties, this HVB can be fitted to a tight-binding band structure. Thereby one obtains the transfer integrals which enter the mobility framework described in Sec. 2.6. As the dispersion in the direction of the hexyl side chains turned out to be negligible, the analytic tight-binding expression used here includes only transfer integrals in inter- and intrachain direction

$$\begin{aligned}\epsilon(\mathbf{k}) = \epsilon_0 + 2\epsilon_a \cos(\mathbf{k}\cdot\mathbf{a}) + 2\epsilon_c \cos(\mathbf{k}\cdot\mathbf{c})& \\ + 2\epsilon_{2c}\cos(2\mathbf{k}\cdot\mathbf{c}) + 2\epsilon_{3c}\cos(3\mathbf{k}\cdot\mathbf{c}),&\end{aligned} \tag{3.2}$$

where ϵ_0 is an energy offset that does not influence the result and $\mathbf{a}$ and $\mathbf{c}$ denote the lattice vectors in $\mathbf{z}$ and $\mathbf{x}$ direction. Figure 3.17 depicts the tight-binding fit together with the original DFT results on the right. The transfer integrals obtained by this fit are $\epsilon_a = 162$ meV, $\epsilon_c = 421$ meV, $\epsilon_{2c} = -26$ meV and $\epsilon_{3c} = 22$ meV which reflects the much larger dispersion in intrachain (c) than in interchain (a) direction.

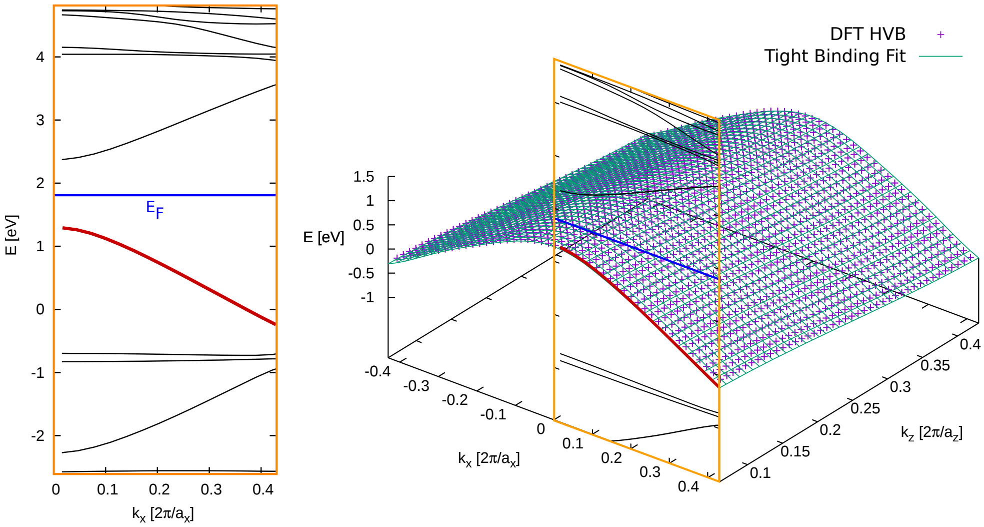

Figure 3.17: *Left:* P3HT band structure in intrachain direction. *Right:* Highest valence band (labeled HVB) together with the tight-binding band fit across the Brillouin zone.

3.2.2 Electron-phonon coupling constants

The P3HT unit cell used here contains 50 atoms which results into 150 phonon modes, there of which three are acoustic and the rest are optical ones. The frequencies ω_λ and displacement patterns of all these modes are determined by DFT calculations for the first time. Moreover, the electron-phonon coupling constants g_i^λ for all optical phonons λ and all directions ($i = 0$ for local coupling and $i = \mathbf{a}, \mathbf{c}, \mathbf{2c}, \mathbf{3c}$ for nonlocal coupling) are obtained by numerical differentiation of the transfer integrals ϵ_i to the (square root) mass weighted phonon displacement $\mathbf{X}$[112]

$$g_i^\lambda = \frac{\partial \epsilon_i}{\partial \mathbf{X}_\lambda} \cdot \frac{1}{\sqrt{2\omega_\lambda^3 \hbar}}. \tag{3.3}$$

The dispersion of the phonon modes is neglected as the determination of the full **q**-dependence of all electron-phonon interaction parameters for all modes would be a prohibitive expensive task. This approximation has also been used in Refs. 40,41,45,47 & 112.

The obtained coupling constants g_i^λ are used to determine an effective coupling constant g_λ^2 for each individual mode λ

$$g_\lambda^2 = 2\sum_i \left(g_i^\lambda\right)^2. \tag{3.4}$$

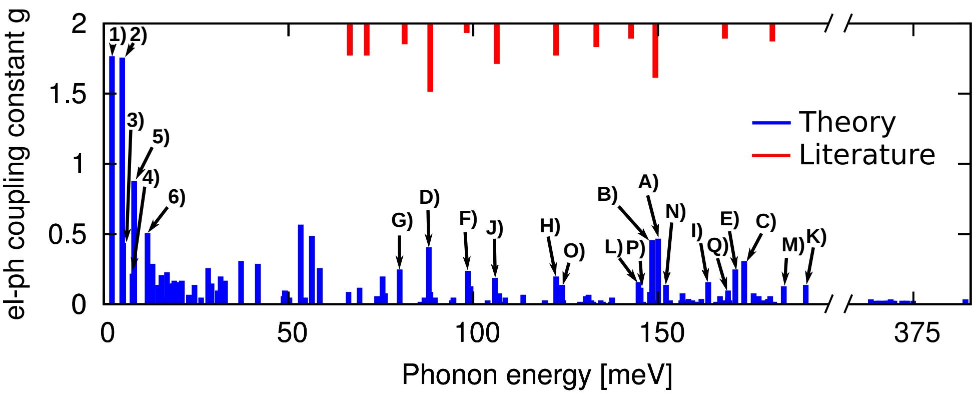

Figure 3.18: Electron-phonon coupling constants calculated for P3HT (blue) by the method described above. The bars shown in red belong to results derived from model fits to experimental data from Refs. 113 and 114 (redshifted by 4 meV). Note that the references (i) provide relative coupling strengths only and (ii) are restricted to phonon energies above 70 meV. The labeled phonon modes are further discussed in Sec. 3.2.4.1 and visualized in Figs. 3.23 and 3.24. The DFT calculations suggest a phonon gap between 190 meV and 363 meV which is suppressed in the figure.

The calculated electron-phonon (el-ph) coupling constants are summarized in Fig. 3.18 and are compared to present literature data. Unfortunately this data is only available for phonon frequencies above 70 meV. Though, the phonon frequencies and coupling strengths calculated here agree well with the available and 4 meV redshifted parameters determined in Refs. 113 & 114. However, one has to mention that their experimental fit parameters contain one prominent mode at about 250 meV. This does neither match the experimental frequencies nor the present calculations which predict a phonon gap between 190 meV and 363 meV, in agreement with Raman and Fourier transform infrared spectroscopy (FTIR) measurements in Ref. 115. The mode might either be an artifact of the fitting procedure or belongs to a defect related local vibrational mode or an unknown defect.

The calculated vibrational spectrum shows dominating strongly coupling modes at low energies (indicated as modes **1)** to **6)** in Fig. 3.18). Their large coupling strength is a consequence of their low frequency, which enters inversely as a pre-factor in the coupling constant calculation (cf. Eq. 3.3). Nevertheless, also at higher frequencies strong coupling modes can be found which are further analyzed in section 3.2.4.1.

3.2.3 Temperature-dependent chemical potential

After the determination of all material parameters, one has to calculate the temperature-dependent chemical potential $\zeta(T, N_c)$ which enters into the Fermi-Dirac distribution $n\left(\tilde{\epsilon}(\mathbf{k}), T, N_c\right)$ (cf. Eq. 2.84 which is used in Eqs. 2.85 and 2.87 for the calculation of the total mobility). In accordance with previous publications[40,45,116], a very low charge carrier concentration of $N_c/N_\Omega = 10^{-6}$ holes per unit cell is used.

The position of the chemical potential $\zeta(T, N_c)$ for a given temperature and hole concentration can be determined by asserting that

$$N_c \overset{!}{\widehat{=}} \int_{BZ} n\left(\tilde{\epsilon}(\mathbf{k}), T, N_c\right) d^3\mathbf{k}. \tag{3.5}$$

Note that $\tilde{\epsilon}(\mathbf{k})$ is the polaron band structure introduced in Eq. 2.81.

To determine the chemical potential $\zeta(T, N_c)$, a bisection algorithm was implemented which basically evaluates the number of charge carriers per unit cell for different chemical potentials (starting with guesses). Based on these results, the choice of the chemical potential is refined till the evaluated number of charge carriers has converged to the chosen N_c (within a relative tolerance of 10^{-4}). This procedure has to be repeated for a representative set of temperatures as the polaron band structure $\tilde{\epsilon}(\mathbf{k})$ as well as the Fermi-Dirac distribution are temperature dependent. Figure 3.19 shows the distribution for two different temperatures on the right hand side (chemical potentials denoted as ζ and ζ‘). Due to the increased smearing at higher temperatures the chemical potential must increase in energy to keep the charge carrier concentration constant.

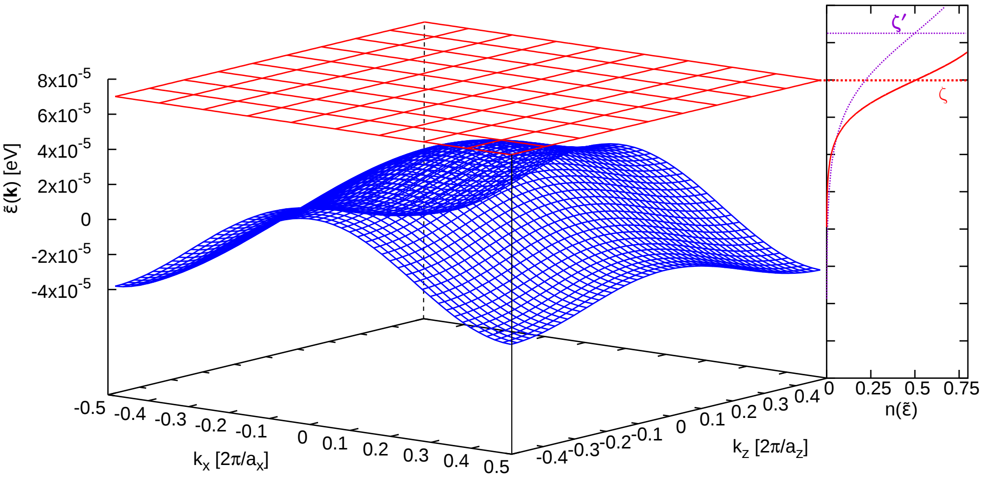

Figure 3.19: Polaron band structure with sketched Fermi-Dirac distribution on the right hand side. The chemical potential is indicated in red while the two curves on the right hand side represent the Fermi-Dirac distribution at different temperatures with their respective chemical potential ζ and ζ‘.

3.2.4 Temperature-dependent hole mobilities

Based on the material parameters gained above, the hole mobility in P3HT can be calculated according to Eqs. 2.85 and 2.87. Therefore, the equations were implemented in `C++`, which also allows to determine the temperature-dependent chemical potential. The dephasing time $\hbar/\tau = 0.1$ meV is a small parameter which is chosen within the limit of ultrapure crystals. Beyond being a mere numerical parameter in the first place, τ can also be assigned an additional role as effective scattering time, which then describes scattering mechanisms not explicitly treated in the formalism.

The integral in Eq. 2.87 was evaluated using the `gsl_integration_qag` routine of the GNU Scientific Library (GSL). Unfortunately, the integrand oscillates rapidly due to the $\Phi_\lambda(t)$ function in the exponent, which requires many integration steps to achieve accurate results. As this integral is the inner part of the sums over $L, M, N, \mathbf{k}_1$ and $\mathbf{k}_2$ it needs to be evaluated many times, making the evaluation of Eq. 2.87 very time consuming. To speedup the calculation a different way was devised, defining a new function

$$I(E,J) = \int_{-\infty}^{\infty} e^{(it/\hbar)E} \left\{ \exp\left[-J \cdot \sum_{\lambda} \Phi_\lambda(t) g_\lambda^2 \right] - 1 \right\} e^{-(t/\tau)^2} dt, \tag{3.6}$$

where the parameter E substitutes the expression $[\tilde{\epsilon}(\mathbf{k}_1) - \tilde{\epsilon}(\mathbf{k}_2)]$ and J the term $\left(\delta_0^M - \delta_L^M - \delta_{-N}^M + \delta_{L-N}^M\right)$. This Eq. 3.6 can be tabulated (for each temperature), making use of the fact that the range of E can be calculated from the maximum and minimum of the polaron band structure and J can adopt only the values $\{-2, -1, 0, 1, 2\}$. Moreover, the range spanned by E decreases with increasing temperature due to the band narrowing (cf. Eq. 2.79).

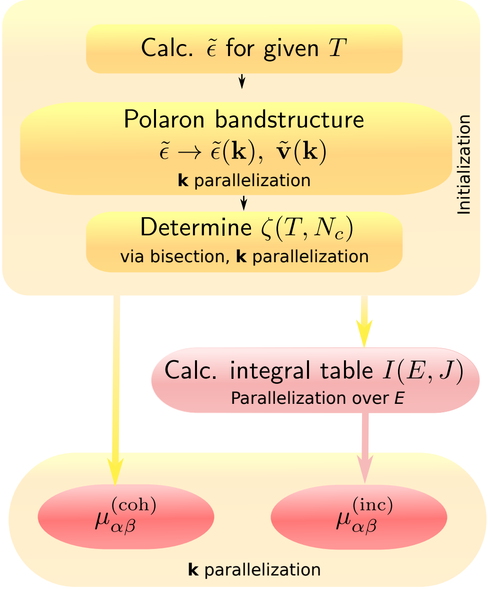
Calc. $\tilde{\epsilon}$ for given T
Polaron bandstructure
$\tilde{\epsilon} \rightarrow \tilde{\epsilon}(\mathbf{k})$, $\tilde{\mathbf{v}}(\mathbf{k})$
k parallelization
Determine $\zeta(T, N_c)$
via bisection, **k** parallelization
Initialization
Calc. integral table $I(E, J)$
Parallelization over E
$\mu_{\alpha\beta}^{(\mathrm{coh})}$
$\mu_{\alpha\beta}^{(\mathrm{inc})}$
k parallelization

Figure 3.20: Flowchart for the calculation of the coherent $\mu_{\alpha\beta}^{(\mathrm{coh})}$ and incoherent $\mu_{\alpha\beta}^{(\mathrm{inc})}$ mobility. This work flow has to be repeated for every temperature value T.

This procedure clearly speeds up the evaluation of the incoherent mobility in Eq. 2.87 as the integral evaluation is reduced to a simple linear interpolation in E between two tabulated values.

The full application flow is depicted in Fig. 3.20, right. The `C++` program makes use of the Message Passing Interface (MPI) to parallelize the work flow without being restricted to shared memory. Thereby it distributes the workload across the large number of $\mathbf{k}$ points. Additionally, the filling of the table, containing the integrals $I(E, J)$, is distributed across all MPI processes to speed up this part of the initialization.

The calculated total mobilities are shown in Fig. 3.21 **a)** and **b)** as linear and Arrhenius plot, respectively. The mobilities increase with temperature, reaching about $50\ \mathrm{cm}^2/(\mathrm{Vs})$. These large intrinsic mobilities are conveyed by the large electronic coupling along the polymer chain in the ideal P3HT crystal with dominating $\varepsilon_c = 421$ meV. Despite this huge transfer integral, the main contribution comes from the phonon-assisted transport (Eq. 2.87), which is large due to the strong coupling modes with low vibrational energies.

Since the material parameters are obtained for a perfect P3HT crystal, the calculated mobilities represent a special case under idealized conditions. This makes it hard to directly compare with experimental measurements, especially as experimentally only an average mobility is measured which accounts also for charge carriers that are trapped[111,117,118]. Thereby one has to keep in mind that already the choice of another solvent for the P3HT-film preparation can change the mobility by several orders of magnitude[119]. Hence, it is reasonable to better compare with experiment-based estimates of the intrinsic mobilities. There are already several publications[67,89,111,119,120]

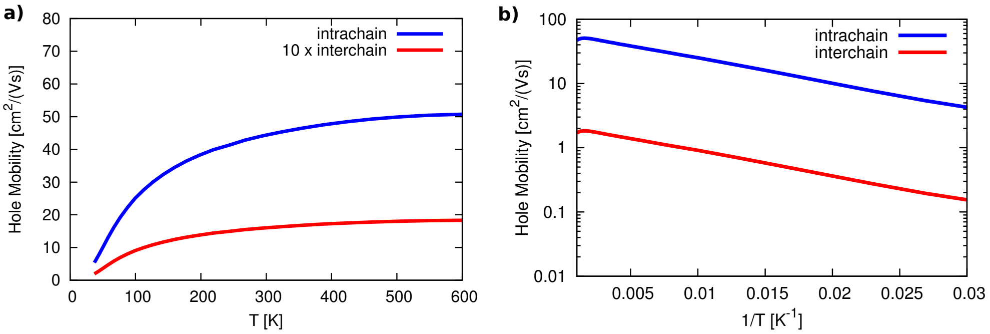

Figure 3.21: a) Total mobility results for a P3HT crystal in intra- and interchain direction. b) Same data as in a) but as Arrhenius plot.

dealing with the experimental challenge to enter the regime of non-trap-limited mobilities in P3HT, thereby attempting to obtain indirect estimates of the intrinsic mobilities. One approach is the fitting of temperature-dependent transport data to a mobility-edge model. This gives intrinsic mobility estimates of about $1\ \mathrm{cm}^2/(\mathrm{Vs})$[109,117] (with some variability) which are orders of magnitude larger than the range of trap-limited values typically encountered[67,89,111,119,120]. Beside the mobility-edge model estimates from trap-limited transport, there is also a theoretical work of Northrup[121] employing an acoustic deformation potential scattering model[122]. He calculated a mobility of $31\ \mathrm{cm}^2/(\mathrm{Vs})$ at room temperature which fits well the present results depicted in Fig. 3.21 ($44\ \mathrm{cm}^2/(\mathrm{Vs})$).

From the Arrhenius dependence over a large temperature range (cf. Fig. 3.21 **b)**), one can extract an activation energy for the transport of about 8 meV. As anticipated, this value is lower than in trap-limited transport regimes which is consistent with the higher mobilities calculated here. Moreover, it was found that experimentally measured activation energies, ranging between 50 and 140 meV[111,123], depend strongly on the presence of defects such as grain boundaries[124–126] which are not taken into account here. In addition, even in high molecular-weight films, the P3HT chains are strongly kinked and folded[120,123], increasing the resistivity and, thus, the activation energy distinctly above its intrinsic value. Chang *et al.*[111] factorized the effective mobility as the product of a disorder and a polaron term yielding activation energies between 5 and 30 meV.

Figure 3.21 depicts also the transport anisotropy for interchain and intrachain mobilities which reaches a factor of about 25, whereas the interchain transport shows a similar temperature activation as the intrachain transport. Experimentally it was found that the intrachain mobility is at least an order of magnitude larger than the interchain mobility[126], similar to the present calculations. Ref. 127 observed that the mobility anisotropy decreases clearly with increasing temperature due to melting effects. These effects as well as thermally induced crystallization and creation of small crystallites with additional grain boundaries and reduced number of bridging chains[128] are not included in the present theory.

In contrast to models relying on fits to experimental data, the ab initio description used here allows for an analysis of the influence of certain phonon modes in more detail. The following subsection examines how low- and high-frequency phonon modes affect the mobility of P3HT, respectively.

3.2.4.1 Characterizing the influence of P3HT phonon modes

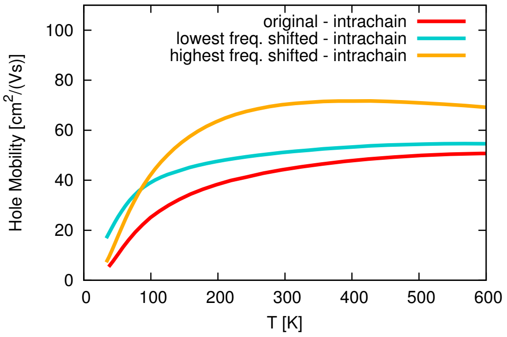

Figure 3.22: Calculated hole mobility assuming that the six lowest phonon frequencies are increased by 10 % (turquoise) or that the phonon frequencies exceeding 80 meV are increased by 10 % (orange) in comparison to the actual values (red).

To get a deeper understanding of the phonons' influence onto the intrinsic charge transport and to possibly assist the molecular design in this regard, the affect of the most relevant phonon modes on the transport characteristics is scrutinized. One possibility to analyze only some selected modes could be realized by reducing their el-ph coupling constant by a certain factor and attribute the change in the calculated mobility to these modes. This approach has the disadvantage that it is not well-suited to give realizable optimization hints for experimentalists, since a direct manipulation solely of the el-ph-coupling constants is hardly possible. Instead, a better way is to blue-shift selected phonon frequencies which can experimentally more easily be achieved by making the polymer matrix more stiff. As the coupling constants depend on the frequencies via $g_\lambda \sim \omega_\lambda^{-3/2}$ (cf. Eq. 3.3), the originally intended goal of reduced coupling constants is also fulfilled with this approach. In the following, the low energy and high-energy modes are modified separately to analyze their individual impact onto the mobility due to reduced el-ph couplings through increased mode frequencies (by 10%).

The resulting temperature-dependent mobilities are depicted in Fig. 3.22. For the orange curve, phonon modes with energies higher than 80 meV are shifted, while for the turquoise curve the lowest six modes are modified. Especially the latter scenario could be realized by making the P3HT polymer backbone less flexible, for instance. Fig. 3.22 shows that a frequency blueshift by 10 % of the lowest six phonon modes (turquoise) increases the low-temperature mobility considerably, but has less influence for temperatures at or above room temperature. Therefore, a stiffening of the polymer matrix, in order to lock torsional modes (cf. Fig. 3.23) or at least increase their vibrational frequency, can indeed moderately improve the P3HT transport properties.

Fig. 3.22 shows a crossing of the orange and turquoise curves at about 80 Kelvin so that a modification of the low-frequency modes yields a more increased mobility for temperatures below 80 K. To understand this effect in the low temperature regime, one can simplify Eq. 2.87 to evaluate it analytically, assuming that there are only two effective phonon modes – one with low frequency ($\hbar\omega_1 < k_B T$) and one with high frequency ($\hbar\omega_2 \gg k_B T$). The mobility depends on the frequencies and coupling constants (g_1 and g_2) according to (cf. Eq. 2.91 in Sec. 2.6 for the derivation)

$$\begin{aligned} \mu \sim \frac{\epsilon^2\sqrt{\pi}\tau}{2k_B T} \cdot \sqrt{\frac{\sinh\left(\frac{\hbar\omega_1}{2k_B T}\right)}{4\pi g_1^2}} e^{-2g_1^2 \tanh\left(\frac{\hbar\omega_1}{4k_B T}\right)} e^{-2g_2^2} \rightarrow \\ \hookrightarrow \quad \sim T^{-\frac{3}{2}} e^{-\frac{\hbar\omega_1 g_1^2}{2k_B T}} \cdot e^{-2g_2^2}. \end{aligned} \tag{3.7}$$

This equation shows that the influence of a mode energetically far above $k_B T$ is roughly independent of temperature and frequency and enters only via its coupling constant (cf. mode 2 in Eq. 3.7). This remaining factor is caused by the zero-point vibration which every quantum mechanical oscillator possess even at "zero" temperature. Nevertheless these zero-point vibrations still have a lowering influence onto the mobility ($e^{-2g_2^2}$), especially for a strong coupling mode.

Since the low frequency modes in P3HT have much larger coupling constants (cf. Fig. 3.18) than the high-frequency ones, a tuning of the former leads to a predominant mobility increase in this low temperature regime. With rising temperatures, the

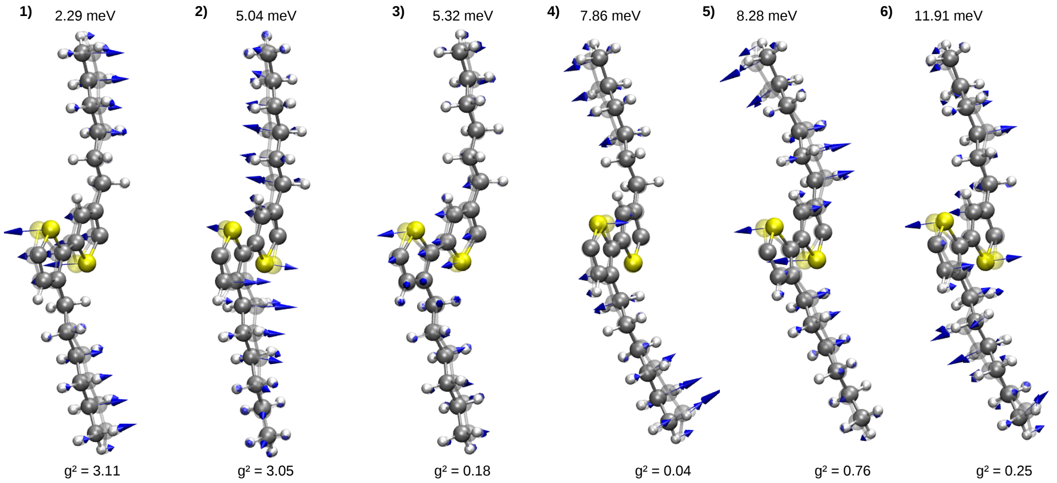

Figure 3.23: Calculated eigenvectors of the lowest frequency phonon modes.

approximation made in Eq. 3.7 for the high-energy modes is not valid any longer so that their high frequency enters the exponent and overcompensates the lower coupling constants. Hence, the blue-shift of the high-frequency modes (orange) leads to considerably increased hole mobilities, in particular at room temperature and above (cf. orange curve in Fig. 3.22). The overall increase of the mobility compared to the unmodified phonon modes (red curve in Fig. 3.22) can also be understood in terms of the polaron binding energy $E_{\text{pol}} = \sum_{\lambda} \frac{1}{2} g_{\lambda}^2 \hbar\omega_{\lambda}$ which decreases with increasing frequency and decreased el-ph coupling constants (according to Eq. 3.3). The polaron binding energy acts as a barrier for the phonon-assisted transport. Since the high-frequency modes contribute more to E_{pol}, the mobility increase is also larger upon tuning those. Moreover, one has to mention that these weakly excited high-energy modes constitute energetic traps due to their large polaron binding energies. Therefore, they do not contribute to an increased hopping rate at room temperature but decrease the mobility by trapping charge carriers. Thus, it is necessary to identify the important high-frequency phonon modes of P3HT and to investigate their displacement patterns in order to potentially modify them in P3HT.

Fig. 3.24 depicts the 17 most relevant high-frequency modes ranked by their contribution to E_{pol}. This rating is different from a sorting by coupling constants as it includes also the frequency dependent pre-factor. The modes **A)** and **B)** are by far the most important ones among the phonons shown in Fig. 3.24. These modes feature strong vibrational amplitudes at the ring carbon atoms and thus affect strongly the upper most valence band (labeled HVB, isosurface shown on the top left in Fig. 3.24) which explains their relevance for the hole mobility. The HVB corresponds to π-states at the $\mathrm{C{=}C}$ ring bonds and has nodes at the interring connection and at the C-C bond opposite to sulfur.

The phonon modes **D)**, **F)**, and **M)** involve also carbon atoms of the thiophene rings but they stretch and compress mainly the node positions of the HVB, hence affecting the transfer integrals somewhat less. The modes **K)** and **N)** influence the transfer integrals also less as their stretching and compression of $\mathrm{C{=}C}$ bonds nearly compensate each other due to the asymmetric nature of the vibration. Moreover, out of plane movements of C atoms (e.g., in mode **J)**) are also of little relevance as they are accompanied by small bond-length changes only.

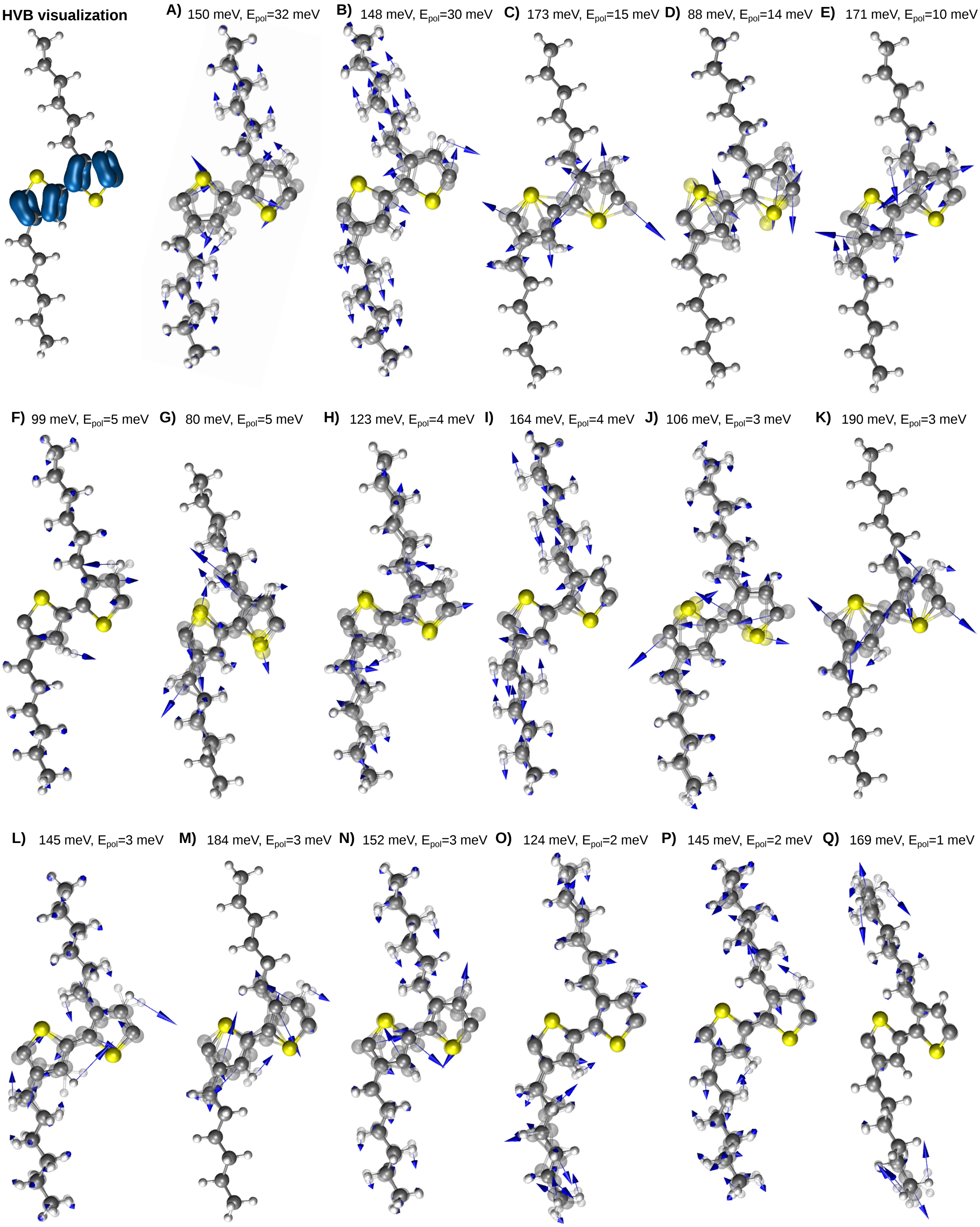
HVB visualization
A) 150 meV, E_pol=32 meV
B) 148 meV, E_pol=30 meV
C) 173 meV, E_pol=15 meV
D) 88 meV, E_pol=14 meV
E) 171 meV, E_pol=10 meV
F) 99 meV, E_pol=5 meV
G) 80 meV, E_pol=5 meV
H) 123 meV, E_pol=4 meV
I) 164 meV, E_pol=4 meV
J) 106 meV, E_pol=3 meV
K) 190 meV, E_pol=3 meV
L) 145 meV, E_pol=3 meV
M) 184 meV, E_pol=3 meV
N) 152 meV, E_pol=3 meV
O) 124 meV, E_pol=2 meV
P) 145 meV, E_pol=2 meV
Q) 169 meV, E_pol=1 meV

Figure 3.24: Calculated eigenvectors of relevant high-energy phonon modes exceeding 80 meV, ordered according to their polaron binding energy. The HVB orbital character is indicated on the top left (relevant for all the modes shown).

Some of the important strong-coupling modes from Fig. 3.18, whose phonon patterns are depicted in Fig. 3.24, have also been identified in experiments: Refs. 115 and 129 find a strong symmetric $\mathrm{C{=}C}$ mode at 179 meV which is in good agreement with the present mode **C)**. Moreover, a weaker antisymmetric $\mathrm{C{=}C}$ mode was reported at 187 meV[115,129] which coincidences well with mode **K)** at 190 meV. Refs. 129 and 115 detected also a C-C stretching mode at 171 meV, perfectly matching the present mode **E)**, where the C-C bonds opposite to the sulfur atom are compressed and stretched. Furthermore, mode **G)** with an energy of 80 meV involves a vibration of the sulfur atoms which is detected in Ref. 115 at 84 meV.

It is found that high-energy modes, involving mainly hydrogen oscillations, are typically negligible for the relevant transfer integrals. This does not apply for mode **F)** at 99 meV (experimentally detected as “CH out of plane bending of the thiophene ring” at 102 meV[115]) as this phonon mode involves also backbone C atoms. Similarly, one finds that the influence of hexyl side chain vibrations on the transfer integrals are minor (cf. modes **O)** – **Q)**) as long as they do not affect carbon backbone atoms as in modes **G)**, **H)** and **L)**.

Summarizing the temperature-dependent transport results of this section, a well defined limit for the mobility in crystalline material including polaron effects was determined. This helps in the interpretation of experimental data, where disorder as well as polaron effects manifest themselves in qualitatively similar ways[111]. Thereby it was found that high-frequency molecular vibrations with strong coupling constants reduce the hole mobility considerably at room temperature. Especially modes deforming the $\mathrm{C{=}C}$ bonds in the thiophene ring are harmful for the charge transport. Hence, one might think about material modifications which reduce the influence of these modes. However, the calculated mobility limit demonstrates that far better improvements can be expected from further increasing the crystallinity of present P3HT-based devices. The comparison of the predicted theoretical limit for ideal crystals with measurements for various P3HT films thereby implies that the experimental samples suffer from significant structural disorder. These imperfections influence the device performance most strongly by decreasing the carrier mobility by more than two orders of magnitude.

4

Indium nanowires on Si(111)

Indium nanowires form by self-assembly upon annealing of a monolayer of indium on a Si(111) surface, thereby having the advantage of easy preparation and reproduction. These atomic-scale wires constitute an important model system since they offer a broad range of interesting physics due to their strongly intertwined structural, vibrational, and electronic properties[130]. It is very beneficial that their physical properties can be accessed by high-resolution surface analysis tools. Furthermore, the wires have long been investigated as model systems for phase transitions in quasi one-dimensional structures and electron transport on the atomic scale[131–140]. The computationally tractable size of the system allows thereby the theoretical analysis of these properties.

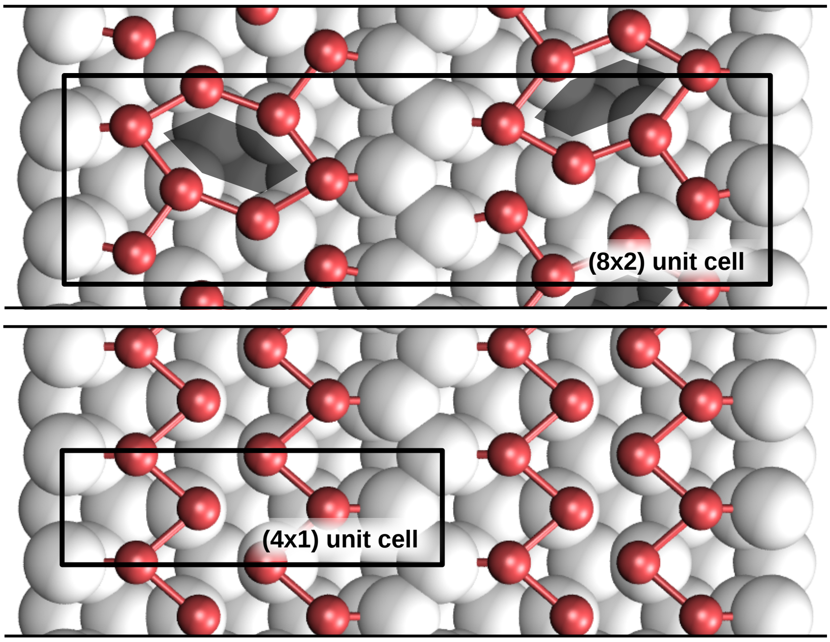

Figure 4.1: (8×2) hexagon low temperature phase (*top*) and (4×1) room temperature phase forming regular zig-zag chains (*bottom*).

The indium nanowires are known to form a low-temperature semiconducting and a room-temperature metallic phase. The former consists of indium hexagons arranged in a 8×2 translational symmetry[141] (cf. Fig. 4.1, top). This phase lowered its energy compared to the metallic phase by opening a band gap[1] of about $E_g \approx 100$ meV[142–144]. Above around $T_c =$120 K a reversible phase transition occurs and the indium atoms arrange into regular zigzag chains with 4×1 symmetry[133,145], see Fig.4.1, bottom. This insulator-metal transition is accompanied by a resistance decrease of about three orders of magnitude[146]. It is found that adsorbates, depending on their species, either decrease[147–151] or increase the critical temperature T_c[151,152]. Besides, also a possible application as a spin filter has been pointed out in Ref. 138 by analyzing the Rashba splitting in the band structure of the nanowires.

This chapter is divided into two parts: The first section analyzes the quantum conductance anisotropy of the metallic 4×1 phase with the formalism already used for P3HT. By other approaches this kind of investigation was prohibitive expensive before so far. The second section takes a closer look on the 8×2 $\rightarrow$ 4×1 transition between the two phases. In contrast to a thermally driven phase transition, the focus is here on a detailed explanation of a phase transition induced upon laser excitation, experimentally observed in Refs. 153 and 145.

4.1 Quantum conductance of regular indium nanowires upon oxygen adsorption

In this section the quantum conductance of the 4×1 regular zig-zag phase is investigated. Thereby special emphasis is given to the conductivity change in inter- as well as intrawire direction upon exposure to oxygen. The results are of particular interest for characterizing the coupling between adjacent indium wires. The formalism applied here follows the one which successfully described the transport properties of oxygen degenerated P3HT in Sec. 3.1.5. It allows for a determination of the coherent transmission coefficients across the oxygen contaminated indium wires.

Density functional theory (DFT) and scanning tunneling microscope (STM) studies[154,155] found that atomic oxygen adsorbs on threefold coordinated intra-chain sites as depicted in Fig. 4.2. The oxygen adsorbs thereby either above or below one of the two zig-zag chains, or between them[154,155].

To answer the question how strongly the adsorbed oxygen affects the transport along and perpendicular to the wire direction, quantum conductance calculations are performed

---

[1] This effect is also called Peierls transition[142,143].

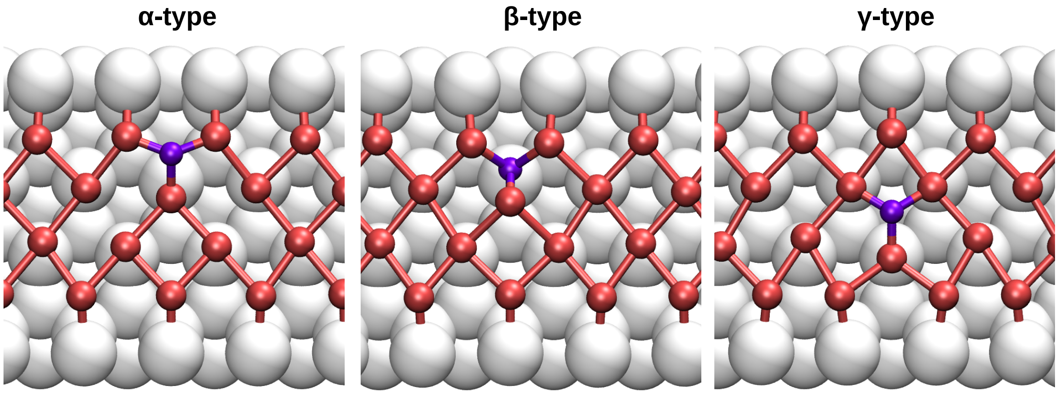
α-type
β-type
γ-type

Figure 4.2: Three different kinds of oxygen defects commonly observed in indium nanowires. The structure and labeling is adopted from Ref. 154 who find a population ratio of $\alpha : \beta : \gamma = 10 : 3 : 1$ by STM measurements for the three kinds of defects.

for the energetically most stable and commonly called α-type oxygen defect. The system setup for the transport in intra- as well as interchain direction is depicted in Fig. 4.3. The composition is similar to the one used in the previous sections: The scattering region contains an adsorbed oxygen atom and is sandwiched between semi-infinite ideal contacts which contain the undisturbed indium nanowires. Several additional ideal unit cells are added to the scattering region, for which the total potential is gained self-consistently (cf. Fig. 4.3), to be able to include also longer-range effects of the oxygen impurity onto adjacent unit cells.

To make the ab initio quantum conductance calculation feasible for such extended

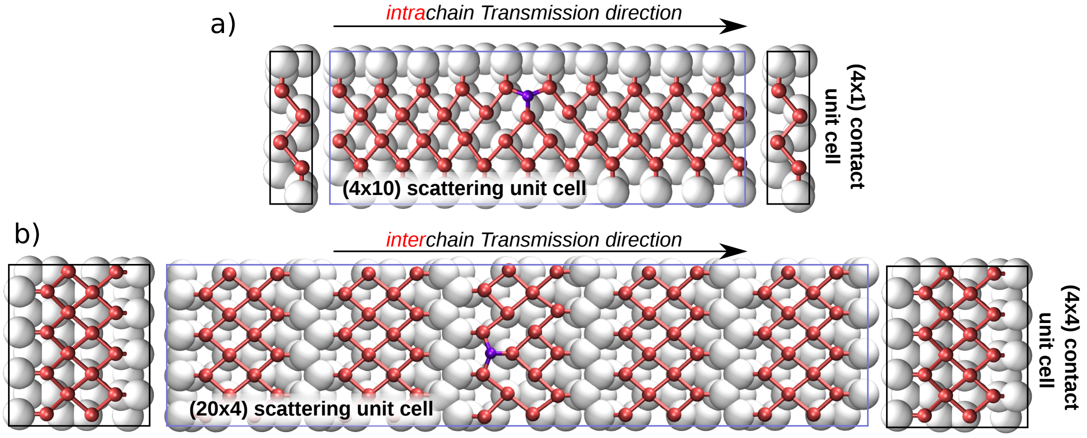
a)
intrachain Transmission direction
(4x10) scattering unit cell
(4x1) contact unit cell
b)
interchain Transmission direction
(20x4) scattering unit cell
(4x4) contact unit cell

Figure 4.3: Schematic setup for the transport calculations along the two directions intra- and interchain. The scattering unit cell containing the oxygen scatterer is sandwiched between ideal wire segments that model semi-infinite ideal contacts.

systems, the silicon substrate is reduced to a single bilayer saturated with hydrogen. A convergence test (for a less extended scattering region) showed that this approximation changes the relative conductivity results ($\sigma_{||}/\sigma_{||}^{\mathrm{pure}}$ and $\sigma_{\perp}/\sigma_{\perp}^{\mathrm{pure}}$) only marginally. This is related to the fact that the reduction of the substrate affects the relevant indium bands only in a minor way compared to a supercell with three double-layers substrate. Moreover, a plane wave energy cutoff of 40 Ry is found to be sufficient enough for the transport description. To sample the 4×1 Brillouin zone (BZ) a 16 (intrachain) × 4 (interchain) × 1 equidistant Monkhorst-Pack[82] $\mathbf{k}$-point mesh is used. The number of $\mathbf{k}$ points is reduced for more extended unit cells accordingly (e.g., the scattering cells).

For the intrawire configuration a significant conductance drop is obtained: The oxygen adsorption decreases the conductance at the Fermi edge to $\sigma_{||}/\sigma_{||}^{\mathrm{pure}} \approx$ 0.65. This ratio agrees quantitatively well with the previous work of Ref. 156 who solely focused onto the intrachain transport, using a Green's function formalism[35,39]. Thereby they showed that mainly two effects cause the strong decrease in the indium nanowire conductivity: On the one hand the oxygen atom forms an effective scatterer due to an induced potential well, on the other hand the impurity leads to deformations of the ideal nanowire structure. The latter was also observed for P3HT in Sec. 3.1.5, where the adsorbed oxygen destroyed the planar polymer backbone, and thus, the conducting delocalized π-system.

In contrast to the previous work[156], here it is also focused onto the comparison of the intra- and interwire transport. Therefore, also the conductivity change in the direction perpendicular to the wires upon oxygen adsorption is determined. A ratio of $\sigma_{\perp}/\sigma_{\perp}^{\mathrm{pure}} \approx$ 0.45 is found which indicates that the coherent transport perpendicular to the wires is slightly more affected than the parallel one. Hence, the results suggest a strong interwire coupling which is disturbed by oxygen adsorption. Here, the available experimental data is controversial since the experiments of Refs. 157 & 158 did not report a change in the $\sigma_{\perp}$ component. However, Ref. 140 finds unambiguously that both the intra- and interwire couplings are affected by adsorption, which is supported by conductivity measurements showing very similar decay rates for the intra- and interwire transport upon oxygen adsorption. The contradicting experimental results might be related to different preparation schemes as it was found that the flash-annealing temperature, used for cleaning and preparation of the Si(111) surface, has a critical influence onto the conductivity perpendicular to the wires[159]. Nevertheless, the calculated changes in the coherent transport are in good agreement with the measurements of Ref. 140 if one considers that a space charge layer, present in the experimental films and causing an isotropic background, is not included in the calculations.

In summary the quantum conductance calculations show a clear effect of single oxygen defects onto the intra- but also onto the interwire electron transport. This reveals an effective interwire coupling which is also supported by experimental measurements of Ref. 140 who find a gradual decrease of $\sigma_\perp$ with increasing oxygen dose.

In the next section it is switched from mainly pure electron dynamics considered so far[2] to a coupled motion of electrons and ions in an insulator-metal transition after optical excitation.

4.2 Optically driven phase transition

Phase transitions between equilibrium states of matter as function of temperature, pressure, magnetics fields, etc. are ubiquitous. However, their direct atomic scale observation is usually not possible. They are typically described in terms of statistical ensembles and phenomenological models, see e.g., Ref. 160. Hence, it is very interesting to analyze phase transitions on the atomic scale. This includes also the detailed investigation of the speed they evolve at and how they can be driven.

Here, the phase transition between the hexagon 8×2 and the metallic 4×1 phase is used as a prototype example to analyze and answer these questions for this broadly studied system. Thereby the focus will be not on the temperature driven phase transition which has been extensively studied in the past[131,136,139,147,148,151,152,161,162], but on the *optically* driven phase transition upon laser excitation which has been experimentally observed (recently) in Refs. 145 and 153. Wall *et al.* & Frigge *et al.* monitored the phase transition using time-resolved reflection high energy electron diffraction (RHEED) on the femtosecond scale. To achieve such a fine time resolution in the pump-probe experiments, an enormous effort was made to tune the experimental setup. For instance, to compensate the velocity mismatch between the laser pump and the RHEED-electron probe pulses, a tilted pump-pulse front[163] was used. This 120 fs pump laser pulse with a photon energy of 1.55 eV turns the low-temperature 8×2 geometry into the room-temperature 4×1 while the measured temperature is far below T_c. Hence, conventional thermal melting can be excluded, suggesting that the phase transition is driven by non-thermal processes[164–169].

The microscopic elucidation of this optically driven phase transition is the central goal of this chapter.

The theoretical description of the system is based on DFT within the local density approximation (LDA) as this functional (in contrast to PBE) is able to predict the relative energies between the phases accurately[130,136,137,145,154,161,170–172].

---

[2] With exception of the polaron quasiparticle description in Sec. 3.2

The surface is modeled within a supercell, containing three bilayers of silicon with a hydrogen saturated bottom layer. It is separated from its periodic image by 15 Å vacuum, cf. Fig. 4.4. Moreover, norm-conserving pseudopotentials in conjunction with a plane-wave basis set limited by a cutoff energy of 50 Ry are employed to describe the electronic structure. A shifted 2×8×1 Monkhorst-Pack mesh[82] is used for BZ sampling.

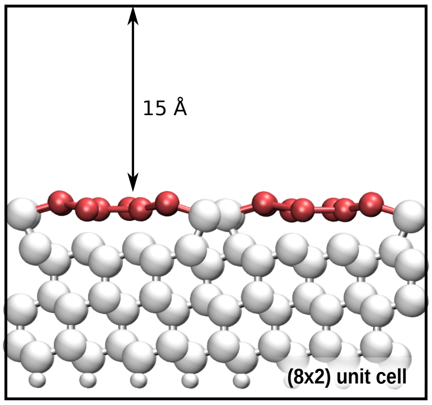

Figure 4.4: Side view onto the surface of the (8×2) hexagon phase modeled by three bilayers of silicon with hydrogen termination and a vacuum spacing of 15 Å.

The following part is divided into four subsections: The system's band structure is analyzed at first to identify states contributing to the phase transition. After this, a detailed bonding analysis is presented, explaining and visualizing the impact of various excited states onto the surface bonds. Next, molecular dynamic (MD) simulations are shown to consider also the time dynamics of the structural phase transition. Finally, the lower and upper excitation thresholds and transition speeds are compared with the experimental results.

4.2.1 Identify contributing states

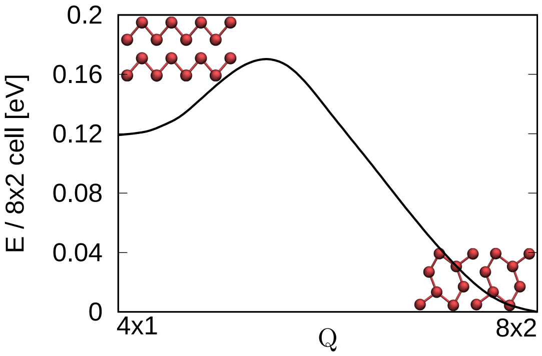

Figure 4.5: Potential energy surface (PES) of the electronic ground state along the energetic minimum path between the 8×2 hexagon (*right*) and the 4×1 regular zig-zag chain phase (*left*).

Potential energy surfaces (PESs) are a well suited tool to characterize the energetic behavior during a phase transition. Figure 4.5 shows the 1D-PES for the electronic ground state at “zero” Kelvin, where the 8×2 hexagon phase clearly constitutes the global minimum. A minor minimum appears also in the shape, corresponding to the room-temperature 4×1 phase, which forms a metastable configuration at “zero” temperature. This phase is separated by a distinct energy barrier of about 50 meV from the global minimum formed by the 8×2 phase. The reaction coordinate Q in Fig. 4.5 was chosen along the minimum energy path on the electronic ground-state PES.

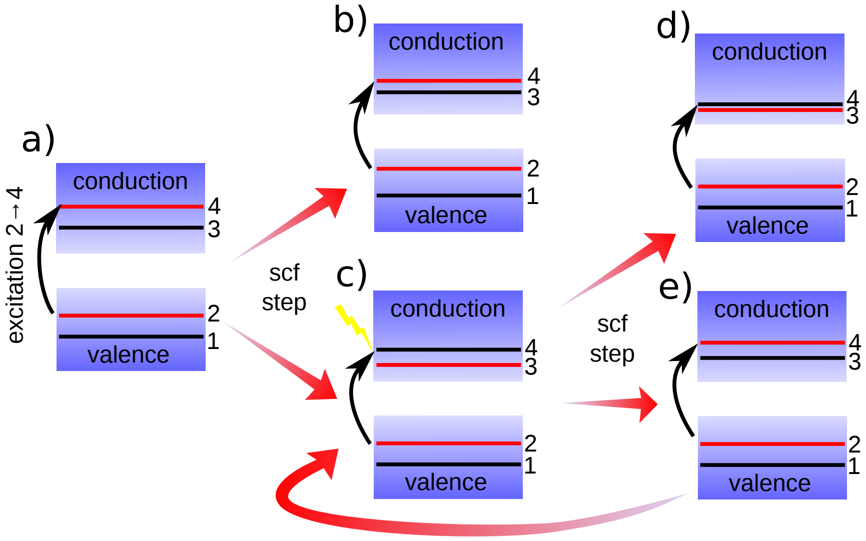

Figure 4.6: Example system in which an excitation from orbital 2 to 4 is modeled. b)–e) show possible configurations which might arise during electronic relaxation. Figures b) and d) constitute thereby converged situations. However, Fig. d) shows an unintentional excited state as the band ordering has changed causing an occupation of different states than selected in a).

To investigate an optically driven phase transition, constrained DFT [173] is used to model laser induced excitations in this work. This means that the occupation numbers of the electronic states are kept frozen to describe a specific excited electron configuration. Thereby different electronic excitations can be analyzed whether they are able to drive the phase transition or not.

As the actual available `Quantum Espresso`-code (v6.0) allows constrained occupation numbers only for calculations with one single $\mathbf{k}$-point, it was extended to support also systems using an arbitrary number of $\mathbf{k}$ points. This implementation allows also to use `Quantum Espresso`'s $\mathbf{k}$-point parallelization and receives the band-, $\mathbf{k}$-point- and occupation-numbers to be modified from a newly defined input card within the standard input file. Figure 4.6 **a)** shows an exemplary system for which the excitation should invert the occupation of orbitals 2 and 4. As such a change in the occupation numbers causes a different potential in the system, the band number of a specific orbital can be different in the ground and the excited state. This leads to the problem that the system can electronically relax into an excited state other than desired. Figures 4.6 **b)** and **c)** show possible configurations how the orbital energies can evolve in following self-consistent field (scf) steps after the occupation numbers were changed to model an excited state. Figure 4.6 **b)** depicts the converged situation where the orbital numbers 2 and 4 still form the desired excited state. In contrast to this, Fig. 4.6 **c)** depicts the case in which the electronic relaxation led to a permutation of band 3 and 4. As the code only excites according to the orbital number, a wrong conductance band is filled now, while the (red marked) originally fourth one is emptied. This reoccupation of the orbitals leads to an abrupt change in the potential which can lead to two consecutive situations: (i) Fig. 4.6 **d)** shows the case in which the system converged into a state in which the undesired fourth state stays filled while (ii) Fig. 4.6 **e)** shows the situation in which the electronic relaxation leads to a re-swapping of the bands again. The latter will usually never converge as the charge is periodically shuffled between the two states which interchange their band number in dependence on their occupation.

Altogether, only the state in Fig. 4.6 **b)** constitutes a desired excited state while the others are unintended or do not converge. This problem occurs more and more frequently, the closer in energy the bands are.

To overcome this problem, the new implementation needed to be modified to guarantee an electronic relaxation into the desired excited state. Therefore, in the present implementation this is now achieved by analyzing the overlap of the wave functions during their self-consistent determination. The new program sequence is sketched in Fig. 4.7.

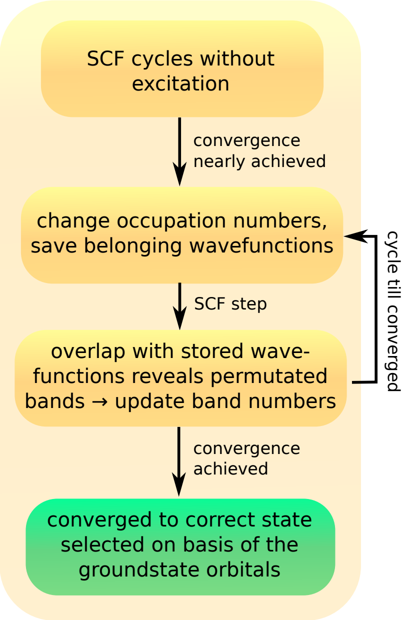
SCF cycles without
excitation
convergence
nearly achieved
change occupation numbers,
save belonging wavefunctions
SCF step
overlap with stored wave-
functions reveals permutated
bands → update band numbers
cycle till converged
convergence
achieved
converged to correct state
selected on basis of the
groundstate orbitals

Figure 4.7: New program flow in order to guarantee a convergence to the desired excited state.

The code expects the band ordering of the ground state in the input file. At the beginning it does not change the occupation numbers according to the input file, hence converging towards the electronic ground state. Shortly before the solver stops due to convergence, the implementation saves the wave functions of the bands to be modified into a separate variable and changes the occupation numbers according to the input file. From now on, the program calculates the overlap of the stored wave functions with the new ones every electronic step and dynamically changes the band number if the overlap reveals a changed band ordering. This way guarantees that always the occupation number of the same orbital is modified and that this orbital coincidences with the one selected for the ground state (cf. Fig. 4.7).

For such realized frozen excited states, 1D-PESs are determined as they allow for an easy classification whether the phase transition is energetically possible and not prevented by an energy barrier. Since the experiment is based on laser excitation, the explored excited electron configurations are restricted to charge neutral ones. Nevertheless, the excited states are not forced to conserve momentum due to possible electronic relaxations caused by scattering processes subsequent to vertical optical excitations. However, the photon energy used to trigger the phase transition in the experiments of Ref. 153 & 145, 1.55 eV, allows for exciting a far larger number of electronic configurations than computationally accessible. Hence, it is necessary to restrict the excited state configurations only to those ones which are long-living enough to drive the phase transition.

The quasiparticle lifetimes due to electron-electron interaction provide corresponding estimates and can be accessed by GW calculations using the imaginary part of the electronic self-energy (cf. Sec. 2.2). Using the $\mathrm{G_0W_0}$ approximation, one can determine the lifetime $\tau_{n\mathbf{k}}$ of a quasiparticle state $\epsilon_{n\mathbf{k}}^{QP,0}$ by[174]

$$\tau_{n\mathbf{k}} = \frac{1}{2\Re\left[Z_{n\mathbf{k}}\right]\Im\left[\Sigma_{n\mathbf{k}}\left(\epsilon_{n\mathbf{k}}^{QP,0}\right)\right]}, \tag{4.1}$$

where $Z_{n\mathbf{k}}$ is only a renormalization factor and $\Sigma_{n\mathbf{k}}$ is the electronic self-energy. Before this approach is applied to the indium nanowires, the quasiparticle lifetimes are calculated in aluminum bulk, which used as a well studied reference system, and compared with literature data. The Brillouin zone of aluminum is sampled with a 12×12×12 Monkhorst-Pack mesh[82] and 32 bands are included in the calculation.

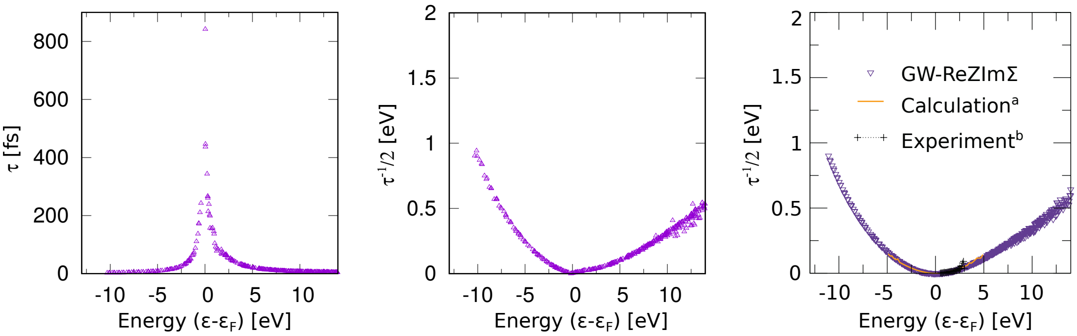

Figure 4.8: *Left/Middle:* Quasiparticle lifetimes calculated for aluminum using Eq. 4.1 (depicted in different units). *Right:* Figure from Ref. 175 showing their $\mathrm{G_0W_0}$ results obtained with the `ABINIT` program package[176] (triangles), older theoretical predictions from Zhukov *et al.*[177] (a) and experimental results by Bauer *et al.*[178] (b).

Figure 4.8, left/middle shows the quasiparticle lifetimes calculated with Eq. 4.1 using the Vienna Ab initio Simulation Package (`VASP`) (depicted in the units [fs] and [eV]). It can be seen that the lifetimes decrease rapidly the further the electron/hole energy is apart from the Fermi level, while directly at the Fermi level infinite lifetimes are possible. A figure from Ref. 175 is depicted on the right hand side of Fig. 4.8, which contains (quasiparticle) lifetimes theoretically as well as experimentally obtained for aluminum. The lifetimes determined with `VASP` agree thereby well with the theoretical and experimental results from the literature. Encouraged by this accordance, the quasiparticle lifetimes are now investigated in the 8×2 indium nanowire phase.

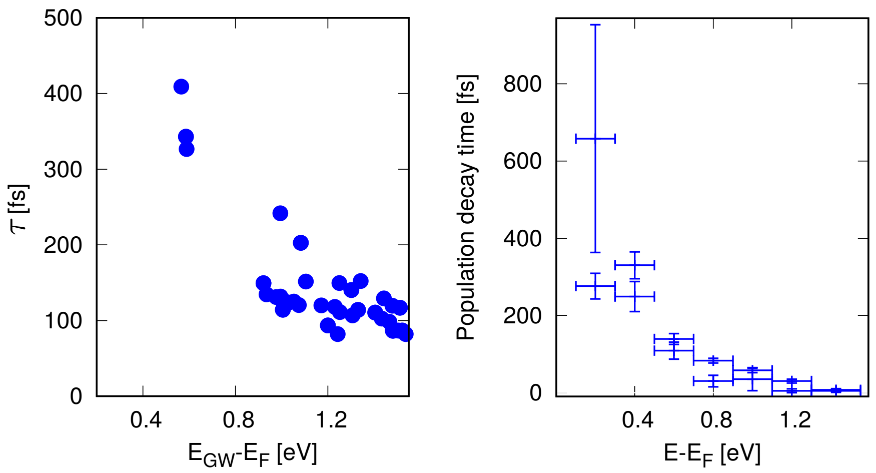

Figure 4.9: G_0W_0 quasiparticle lifetimes (*left*) and the experimentally measured population decay time (*right*, from Ref. 153) for the 8×2 phase.

However, due to the large system size (136 atoms) the G_0W_0 calculation did not complete within the maximum allowed wall clock time. Therefore, the GW implementation of `VASP` had to be modified in order to write arrays containing intermediate results to hard disc drive. With this extension one was able to restart the GW calculation several times after the maximum allowed runtime was reached. The quasiparticle lifetime results are shown in Fig. 4.9, left. The calculations are restricted to 1290 bands (240 occupied + 1050 unoccupied) and 10 $\mathbf{k}$ points due to their enormous expense. However, comparing the G_0W_0 results with experimental measurements of the bands population decay time on the right of Fig. 4.9, the agreement is quite good. This is especially true if one keeps in mind that the quasiparticle lifetimes account not for all possible decay channels covered in the experimental measurements (e.g., electron-phonon, electron-defect scattering and recombinations are not included). Moreover, the GW approximation describes a system including an additional hole (electron) and is therefore related to (inverse) photoemission spectroscopy, respectively[22,179]. This is in contrast to the charge-neutral excitonic excitation experimentally realized here.

Nevertheless, both curves confirm that in particular the electronic states close to the band gap are long-living enough and therefore possible candidates to drive the (8×2) $\longrightarrow$ (4×1) phase transition. In addition, especially the experimental data shows rapidly decreasing lifetimes to only a few femtoseconds for states at higher energies so that these do not have to be considered for the phase transition. The comparably too high quasiparticle lifetimes of those states in the G_0W_0 approximation have also been observed for other systems in Ref. 174 who conclude that "G_0W_0 generally overestimates the lifetime of the quasiparticle states far from the Fermi level".

Due to time reversal symmetry[3], the shifted 2×8×1 Monkhorst-Pack mesh is reduced to 8 $\mathbf{k}$ points in intrachain direction, cf. red line through the sketched Brillouin zone in Fig. 4.10 **a)**. Each $\mathbf{k}$-point represents one of eight sectors used to address different excited state configurations. The potential energy surfaces for some vertical excitations

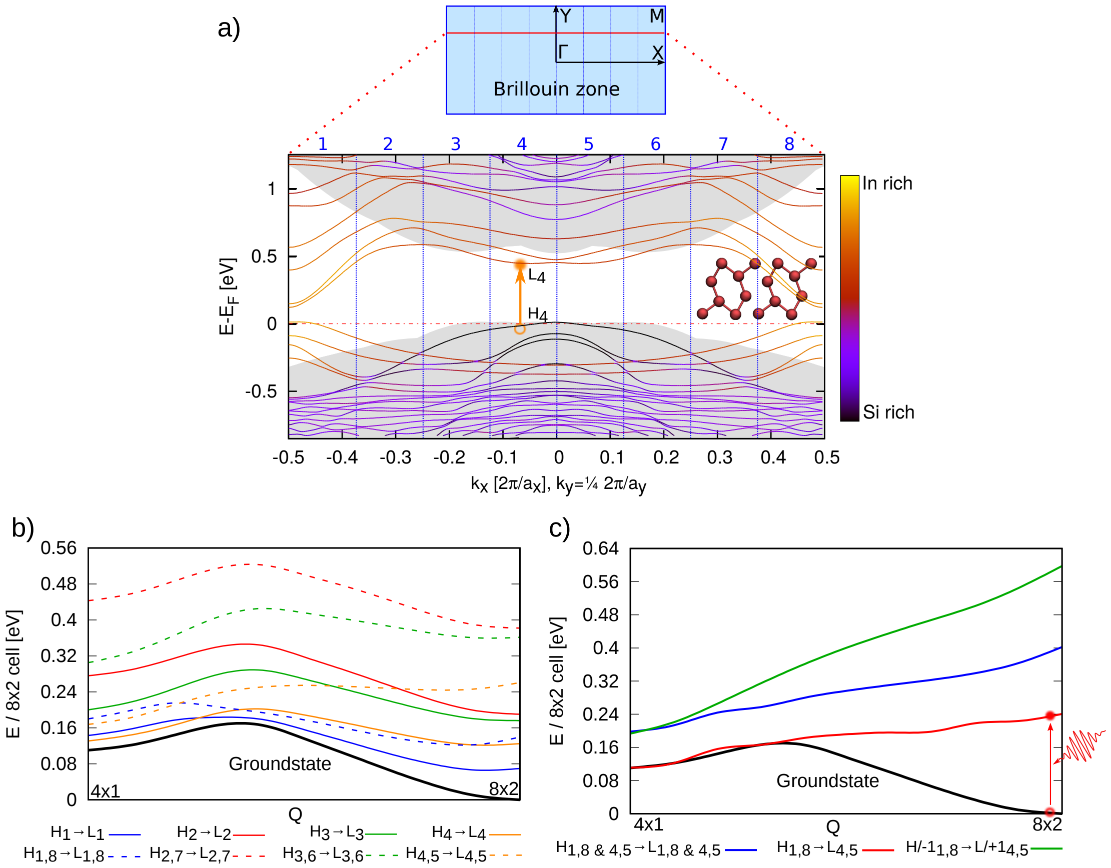

Figure 4.10: a) Cut through the Brillouin zone in intrachain direction. The cut is discretized using 8 $\mathbf{k}$ points, where each represents one sector which is used to address different excited state configurations. The color of the bands indicates whether they originate from the silicon substrate or the indium nanowires while the shaded gray area visualizes the projected silicon bulk band structure. b) Potential energy surfaces for the ground state (known from Fig. 4.5) and different vertical excitations over the band gap. The solid lines excite only between the highest valence band (HVB) and the lowest conduction band (LCB) in one sector (0.25 e^-/8×2 unit cell), while the dashed lines include also the symmetric counterpart (0.5 e^-/8×2 unit cell). The orange arrow in part a) shows exemplary the excitation $H_4 \rightarrow L_4$. c) Further excited state configurations which do not necessarily conserve momentum due to electronic relaxation. The green curve models an excited state with holes in sectors 1 & 8 in the HVB and the underlying HVB-1 and electrons in sectors 4 & 5 in the LCB and LCB+1 (1.0 e^-/8×2 unit cell).

---

[3] Spin-orbit coupling was neglected since it does not noteworthy affect the total energy and forces in the system and has only a slight influence onto the band structure (cf. Ref. 138).

between the valence- and conduction band edges in different sectors are shown in Fig. 4.10 **b)**. The excitation $\mathrm{H}_4 \rightarrow \mathrm{L}_4$, belonging to the orange PES, is sketched in Fig. 4.10 **a)** to clarify the excited configuration labeling. It can be seen that many excitations decrease the barrier between the 8×2 and the 4×1 phase. Though, the 8×2 phase is energetically still favored or an energy barrier hinders a direct transition to the 4×1 phase. Especially an occupation inversion at the smallest band gap in sectors 1 & 8 will not lead to a phase transition as can be seen at the blue curves in Fig. 4.10 **b)**. Only an occupation inversion in the middle of the Brillouin zone in sectors 4 & 5 offers a very small gradient towards the 4×1 phase (cf. orange dashed line). However, there are also several excited state configurations whose PESs show a clear gradient towards the 4×1 phase, hence driving the phase transition as can be seen in Fig. 4.10 **c)**. If one compares the configurations of excited states driving the phase transition, one finds that they have holes in sectors 1&8 at the valence band edge and electrons in sectors

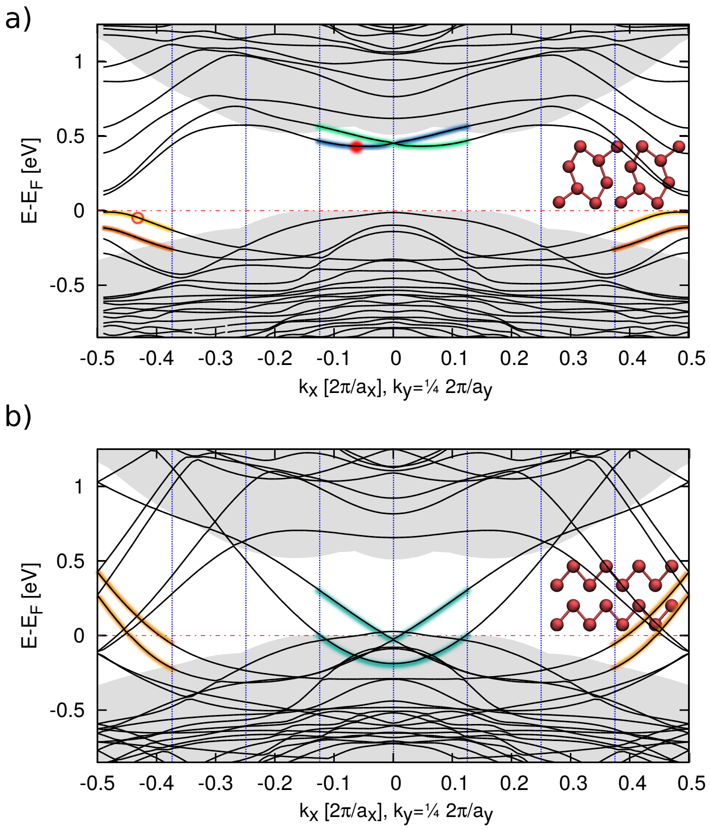

Figure 4.11: a) Band structure of the 8×2 phase as depicted in Fig. 4.10. b) Band structure of the 4×1 phase (in a 8×2 cell for easier comparison). The turquoise highlighted bands correspond to the S_1 and the orange ones to the S_2 band in the 4×1 cell (see, e.g., Refs. 130 & 138 for labeling conventions). All these shaded bands around $\mathrm{k}_\mathrm{x} = 0$ and $\mathrm{k}_\mathrm{x} = \pm 0.5$ constitute the crucial parts in the Brillouin zone for driving the phase transition by excitation.

4 & 5 at the conduction band edge in common. The green PES in Fig. 4.10 **c)** can even considerably increase the energy gradient by taking the underlaying valence band in sectors 1 & 8 and overlaying conduction band in sectors 4 & 5 additionally into account. The excitation of these configurations are clear candidates for driving the (8×2) ⟶ (4×1) phase transition.

One has to mention that excited states composed of several excitations cannot simply be broken down into the PESs corresponding to single excitations. As an example, the $\mathrm{H}_{1,8\,\&\,4,5} \rightarrow \mathrm{L}_{1,8\,\&\,4,5}$ excitation in Fig. 4.10 **c)** is obviously not given by the sum of the $\mathrm{H}_{1,8} \rightarrow \mathrm{L}_{1,8}$ (dashed blue) and $\mathrm{H}_{4,5} \rightarrow \mathrm{L}_{4,5}$ (dashed orange) PESs in Fig. 4.10 **b)**.

The special role of the identified bands and sectors for the phase transition can be understood with the help of Fig. 4.11 **a)** and **b)**, where the band structure of the 8×2 phase is compared with the one of the 4×1 phase, respectively. One finds that the marked excited states in the Brillouin zone center move downwards while the emptied ones at the BZ boundary move upwards during the phase transition. By occupying the downwards moving bands[4], the system gains energy for the phase transition while the states moving upwards[5] are emptied and therefore cannot impede the structural change.

With this explanation one can also understand the physics behind the maximum in the ground-state PES (depicted in Fig. 4.5 and 4.10) which constitutes the potential barrier: For reaction coordinates Q between the 8×2 phase and the maximum, the identified states at the BZ center are empty so that the system does not gain energy upon lowering these states. On the other hand the system needs to pay energy to raise the states at the BZ border which are filled in the ground state. The

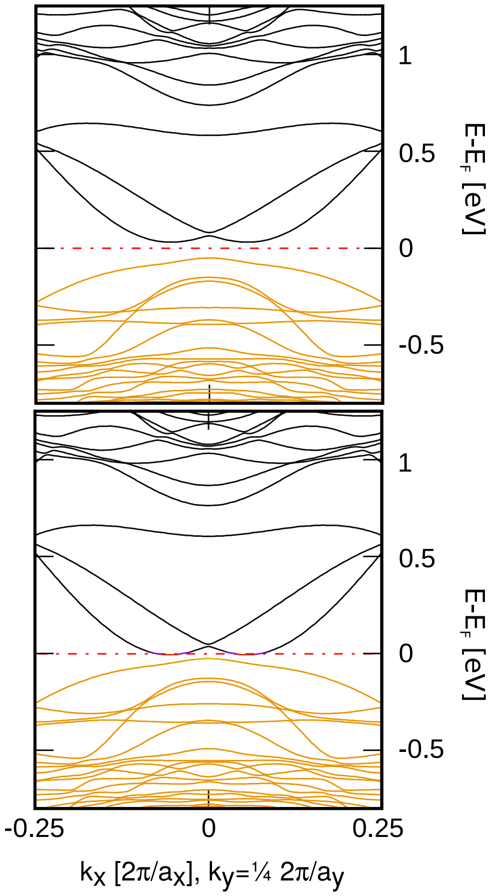

Figure 4.12: Excerpt of the band structure for a structure slightly before (closer to the 8×2 phase, *top*) and after (*bottom*) the maximum of the potential barrier. Orange drawn bands are occupied while black ones are empty.

---

[4] Labeled S_1 in the 4 ×1 cell in the literature[130,133,138], sometimes also m_1, e.g., in Ref. 143

[5] Usually labeled S_2 (m_2) in the 4 ×1 cell

gradient of the PES changes into a falling behavior when the states at the BZ center are lowered so far that they become occupied even in the electronic ground state. An excerpt of the band structure slightly before and after the position of the potential barrier maximum is shown in Fig. 4.12. At the turning point, the Fermi distribution shuffles the charge carriers from the raised states at the BZ border to the center, hence doing exactly the kind of reoccupation which was identified to drive the phase transition. From this critical point on, at which the important states become naturally occupied, the PES shows also in the ground state a clear gradient towards the 4×1 phase (cf. Fig. 4.5).

The orbitals belonging to the marked parts in the band structure in Fig. 4.11 **a)** are depicted in Fig. 4.13 in corresponding colors. As can be seen on the left hand side, the states in the Brillouin center belong to In-In bonds across the hexagons. During the phase transition, the distance between these indium atoms is reduce which explains the observed lowering of the bands in Fig. 4.11. Moreover, the occupation of these bonds results into a force that exerts an attractive interaction between the respective indium atoms and thus actively drives the phase transition. In more detail, the attractive force exerted by exciting electrons in these bonds across parallel In-In zigzag chains excites an In-chain shear phonon mode. This mode occurs at about 28 and 18 cm^{-1} for the (4×1) and (8×2) phase[172], respectively and has also been detected by Raman spectroscopy[180]. The mode is energetically below the phase-transition temperature of about $k_B T = 83$ cm^{-1} and has been suggested to be responsible for the lattice deformation characteristic in the (8×2) $\longrightarrow$ (4×1) phase transition[136,141,181,182]. Additionally, a second important phonon mode, a hexagon rotational mode at about 27

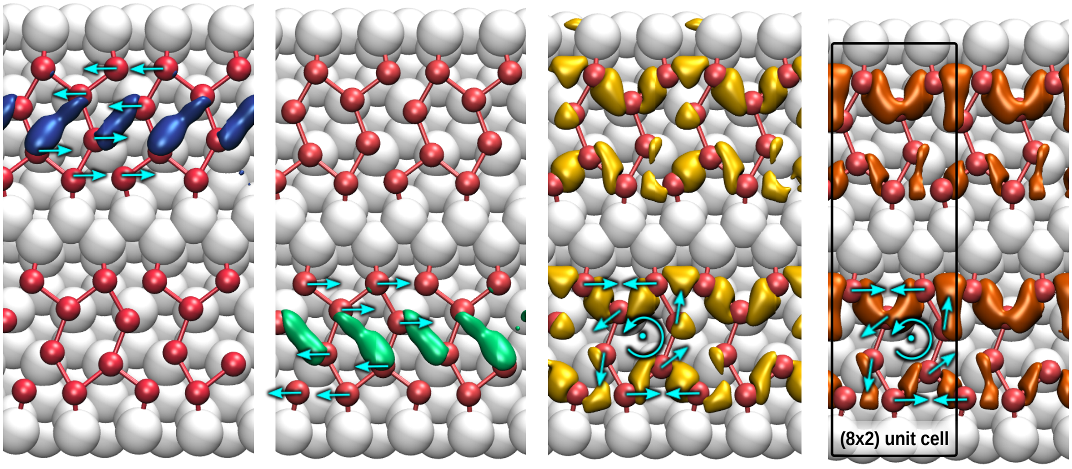

Figure 4.13: Orbitals belonging to the special bands and sectors for the phase transition. The colors correspond to the ones used in Fig. 4.11 to mark the orbitals in the band structure. The arrows indicate two important phonon modes for the phase transition.

cm^{-1} has also been identified[136] to be characteristic for the phase transition. This mode might be excited by a depopulation of the orbitals depicted in Fig. 4.13 on the right as the indium atoms can move more freely in the indicated mode direction.

4.2.2 A detailed bonding analysis

Since the analysis of bond strengths is usually a well suited "measure" for structural phase transitions, this subsection determines the bond strengths upon excitation and during the phase transition to gain further insights.

Therefore, the crystal orbital Hamilton population (COHP) analysis, introduced in Sec. 2.7, is applied as it allows for determining the strength of selected indium-indium bonds within the complicated nanowire structure. Moreover, it is possible to track quantitatively the bond strength changes during the phase transition with this method.

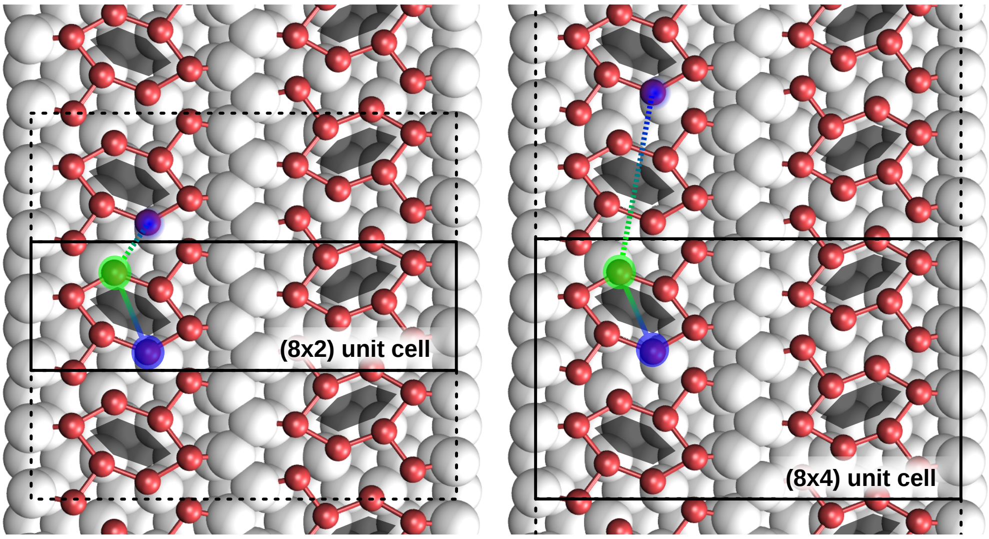

Figure 4.14: *Left:* A COHP bonding analysis between the green and blue marked atoms inside the 8×2 unit cell will include also unwanted but strong contributions from the interaction of the green marked atom with the closer periodic image of the blue atom. *Right:* By extending the unit cell to a 8×4 one, the periodic images are separated far enough to exclude their influence onto the bonding results.

The COHP formalism does not distinguish between a selected atom and its periodic image in other unit cells. Hence, the calculated bond strength between two atoms can contain also unwanted contributions from interactions with the periodic images of the atoms as depicted in Fig. 4.14, left. This problem can be solved by increasing the size of the unit cell in a way that every interaction with a periodic image is negligibly small compared to the one with both atoms in the same unit cell. Therefore, a 8×4 surface unit cell with 272 atoms is used which is depicted in Fig. 4.14, right.

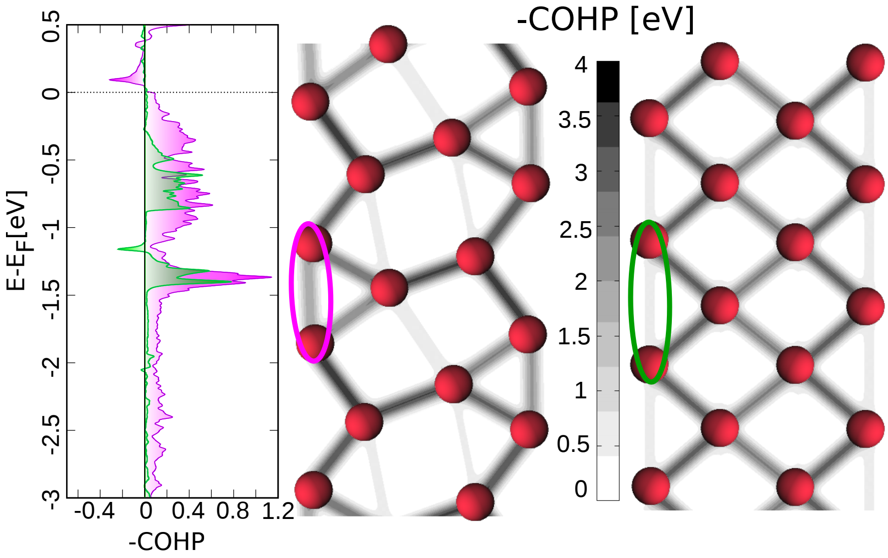

Figure 4.15: Crystal orbital Hamilton population (COHP) analysis for the 8×2 and 4×1 phase. The curves on the left show the COHP results for two selected bonds marked on the right in the same color. COHP values smaller/larger than zero indicate bonding/antibonding states, respectively. The energy integral over such COHP curves weighted with the occupation number of the corresponding states yields the total bond strength. These calculations are performed for all possible atom pairs and are depicted as color coded bonds (*right*), where dark drawn bonds indicate the ones with the largest bond strengths.

The COHP curve for a selected bond once in the 8×2 and once in the 4×1 phase is depicted in Fig. 4.15, left. The results allow for the classification in bonding (COHP < 0) and antibonding (COHP > 0) as well as nonbonding (COHP ≈ 0) states. The integral over such curves (including the occupation number in Eq. 2.92) gives a measure for the bond strength. As the purple marked bond has much larger bonding contributions in the COHP curve on the left, it is notably stronger than the green marked one. These bond strengths are also determined for all other possible In-In interactions and depicted as color code for the (8×2) and (4×1) phase in Fig. 4.15, right. The bonding results for the (8×2) phase coincident well with the commonly assumed indium hexagons (cf. Fig. 4.1). The COHP analysis for the 4×1 phase confirms the typical model of two regular outer zig-zag chains, but with strong bonds between these two rows which are usually omitted in drawings (cf. Fig. 4.1).

To answer the question whether the bond strengths change abruptly or in a rather smooth process, the COHP bond strengths of selected bonds are monitored during the phase transition for the electronic ground state in Fig. 4.16. In contrast to the ground-state PES (also depicted in Fig. 4.16 in black), the bond strengths have no turning point in the curvature but change rather smoothly and monotonous between the two phases. In fact, the green and orange marked bonds are quite remarkable as

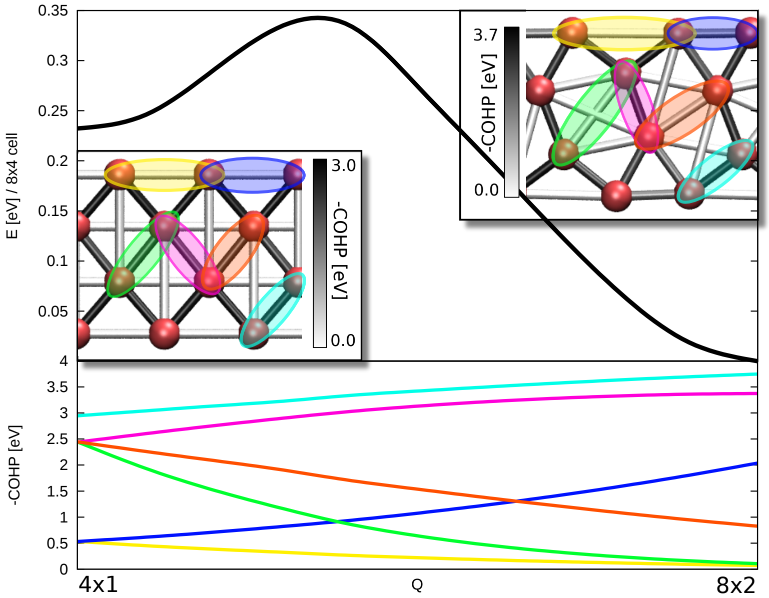

Figure 4.16: *Top:* The black curve depicts the known potential energy surface, which exhibits two minima belonging to the 8×2 phase (*right*), and the 4×1 phase (*left*), whose bonds are color coded as insets (from Fig. 4.15). The colored ellipses mark those bonds for which the bond strengths are traced along the phase transition in the lower graph.

they considerably increase in strength during the phase transition. Other bonds, in particular the one indicated blue between outer-row In atoms, loose strength upon 4×1 phase formation.

The results fit well the localizations of the already identified orbitals (Fig. 4.13) driving the phase transition: While the green and orange marked bonds perfectly match the localization of the excited orbitals in the Brillouin center, the emptied orbitals at the BZ boundary have both a localization at the blue indicated bond. Hence, one can expect that the significant excited states modify the most important bonds strengths in the direction towards the 4×1 phase. This can be also visualized by plotting the COHP analysis exemplary for the green marked bond next to the known ground-state band structure of the 8×2 phase in Fig. 4.17. By depopulating the valence bands at the BZ boundary and occupying the relevant conduction bands in the middle of the Brillouin zone, one shifts charge carriers from antibonding (red) to bonding states (green). Therefore, one can already estimate from the ground-state properties that this excitation will lead to an increased bond strength of the green bond.

After the bonding properties of the excited states were determined qualitatively and solely on the basis of a ground-state analysis, the excited configurations are now modeled with constrained occupation as it was done for the determination of the PESs in Fig. 4.10. For the application of the COHP formalism three representative excited states

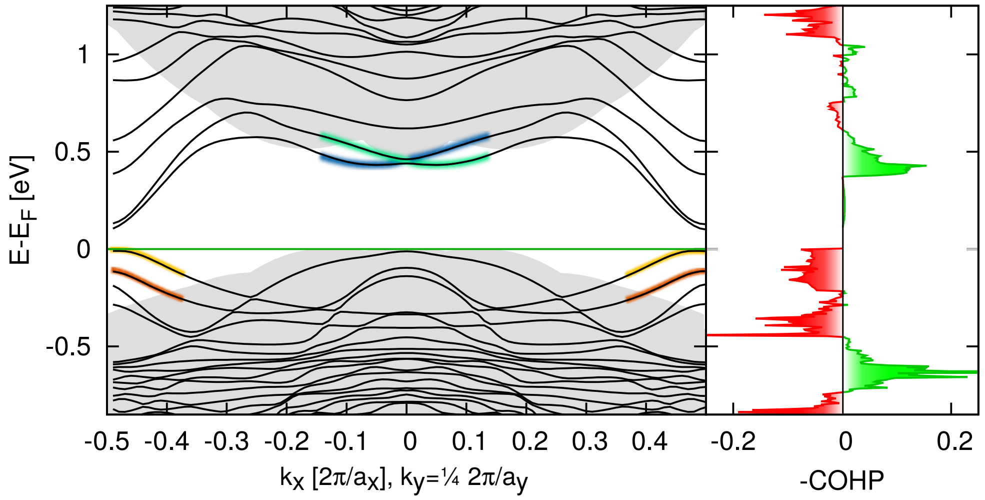

Figure 4.17: *Left:* Band structure of the 8×2 hexagon phase from Fig. 4.11 a). *Right:* COHP diagram for the indium-indium bond marked green in Fig. 4.16.

are selected whose PESs are shown in Fig. 4.18, left. The blue curve belongs to an occupation inversion at the BZ boundary while the red and green curve excite 0.5 and 1.0 electrons per 8×2 unit cell between the identified orbitals marked in Fig. 4.11 **a)**, respectively. For the calculations in the 8×4 unit cell, the number of excited electrons is doubled.

The right hand side of Fig. 4.18 depicts the change in the bond strengths upon particular excitations for selected positions on the PESs shown left. Blue and red drawn bonds indicate an increase and decrease in bond strength, respectively, compared to the electronic ground-state configuration. In agreement with the ground-state analysis,

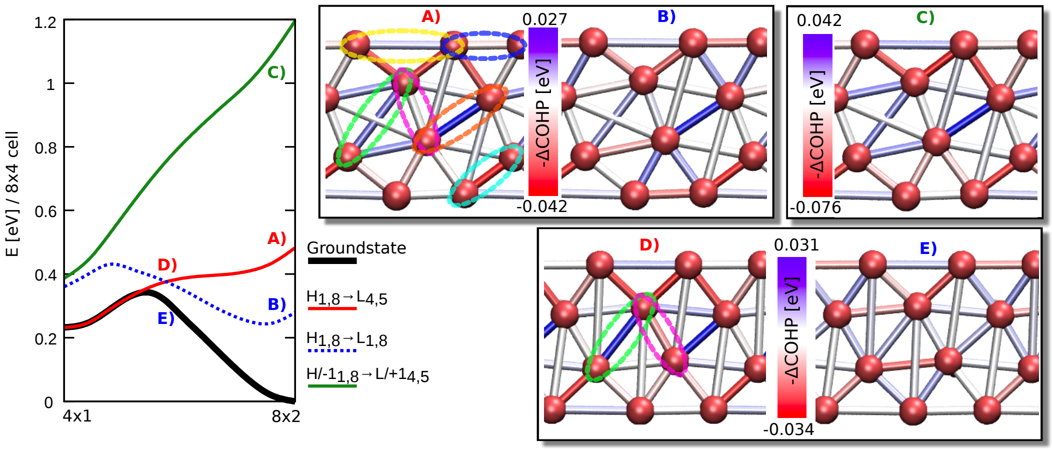

Figure 4.18: *Left:* Three selected potential energy surfaces from Fig. 4.10. *Right:* COHP changes due to the selected excitations. Letters denote the respective positions on the PESs shown left. Blue drawn bonds increase while red drawn ones decrease in strength upon excitation.

the bond in the 8×2 phase, which gains most strength upon excitation, coincidences with the orange marked bond in Figs. 4.16 and 4.18 **A)**. As already pointed out, this fits the need for the phase transition, as this bond is indeed much stronger in the 4×1 than in the 8×2 phase, cf. Figs. 4.15 and 4.16.

Remarkably, the green bond which is strongly involved in the phase transition, is only slightly drawn in blue in the beginning (Fig. 4.18 **A)**). However, as the phase transition has started, this changes completely as can be seen in Fig. 4.18 **D)**, showing the situation in the middle of the phase transition. This means that the excitation strengthens the green bond more and more during the phase transition. This matches perfectly the needs for the phase transition as the gradient of the (green) bond strength curve grows the stronger the closer the system reaches the 4×1 phase (cf. Fig. 4.16, green graph). Similarly suitable acts the excitation onto the pink bond: At the beginning of the phase transition this bond is nearly not influenced (cf. Fig. 4.18 **A)**) but in the middle of the transition (cf. Fig. 4.18 **D)**), this bond is more and more weakened in accordance with the gradient of the corresponding pink curve in Fig. 4.16.

The bonds between the outermost indium chain atoms (marked yellow and blue) are also influenced by the electronic excitation. In particular, if two electrons per 8×4 cell are excited, the yellow marked bond, weaker in the 8×2 than in the 4×1 phase, is strengthened (cf. Fig. 4.18 **C)**).

So far, one can conclude that electronic excitations, involving holes at the BZ boundary and electrons in the zone center conduction states, amplify exactly the important bonds which increase in strength during the transition according to Fig. 4.16. In addition, the bonds pulling in the opposite directions of the green bond are notably weakened, which makes it more easier for the involved indium atoms to decrease the "green" bond length. The bonding analysis therefore nicely illustrates how the excitations identified above drive the phase transition.

Why do some excitations fail to drive the transition? To answer this question, it is illustrative to analyze the occupation inversion at the BZ boundary (cf. blue PES curve in Fig. 4.18). In the 8×2 hexagon phase, this excitation shows a similar change in the bond strengths compared to the one electron per 8×4 excitation discussed above (cf. Figs. 4.18 **A)** & **B)**). Both excited state configurations strengthen in particular the bonds marked orange and green, thereby initiating the phase change. This matches the nearly equal descent of the corresponding red and blue PESs at the beginning of the phase transition. However, the two excitations differ more and more from each other when the phase transition has started: While the red PES continues decreasing, making the 4×1 phase most favorable, the blue PES increases again, leading to a barrier which cannot be overcome. Therefore, a bonding analysis in the middle of the phase transition is needed. The COHP results reflect the gradient behavior nicely - while for the falling red PES the important green and orange marked bonds are strongly strengthened (cf. Fig 4.18 **D)**), this is not the case for the rising blue PES (cf. **E)**). Hence, there are no strong forces pulling the atoms towards the 4×1 phase any more, thus, the transition is not completed and the system oscillates back.

To summarize all bonding results, the COHP analysis has nicely illustrated why particular excitations so strongly drive the phase transition: They weaken/strengthen the important bonds dynamically so that these bonds become closer to the bonds in the 4×1 phase. Moreover, the dynamic behavior is very important as there are excitations which are suitable at the beginning but change their influence in the wrong way during the transition, thus being not able to drive the phase transition.

4.2.3 Time dynamics of the phase transition

After having identified, characterized and illustrated the electronic configurations that are prone to trigger the $(8\times2) \longrightarrow (4\times1)$ phase change, the time dynamics of the corresponding structural modifications have to be addressed. For this purpose, energy conserving molecular dynamic (MD) simulations are performed in adiabatic approximation, again for the three earlier selected excited-state configurations. Their potential energy surfaces are shown in Fig. 4.19, left.

The calculated structural deviation to the 4×1 phase vs. time is shown in Fig. 4.19 on

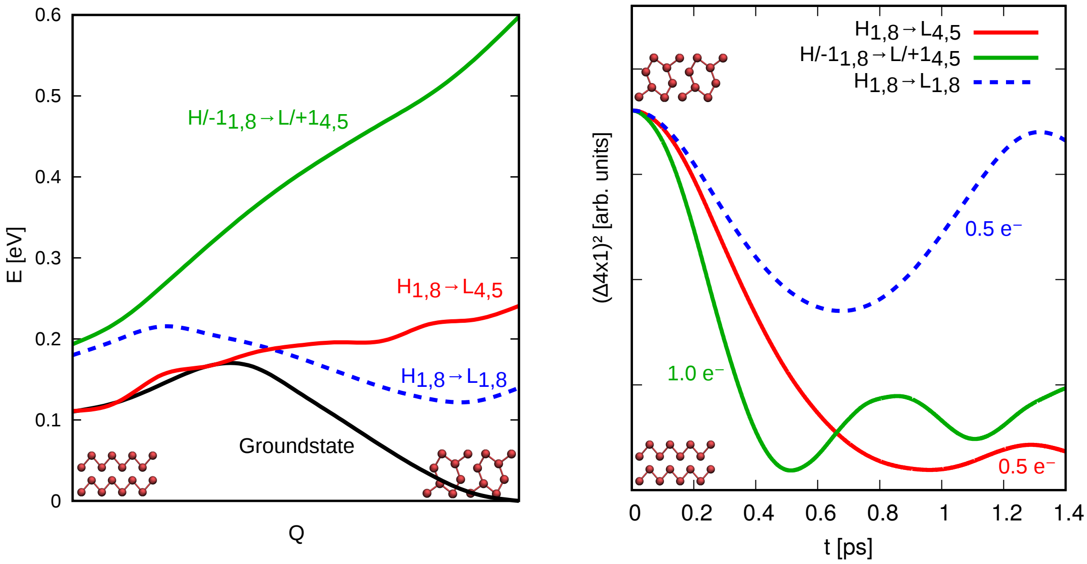

Figure 4.19: *Left:* Three selected potential energy surfaces from Fig. 4.10 for which MD simulations are performed. *Right:* Time evolution of the structural deviation to the 4×1 phase for the three selected excitations starting from the 8×2 phase. The number of excited electrons refers to a 8×2 unit cell.

the right for the three excited state configurations. The blue dashed PES on the left in 4.19 has a barrier in the middle of the phase transition and a global minimum slightly offset from the hexagon ground-state phase. Starting in this ground-state geometry, the excited system transforms its potential energy into kinetic energy while moving towards its global minimum. Afterwards it overshoots due to its kinetic energy but cannot overcome the barrier, hence moving back towards its global minimum. This is confirmed by the MD simulation shown in Fig. 4.19 right, where the blue curve clearly shows this oscillation around its global minimum close to the original 8×2 phase. In contrast to this excitation, the green and red curves constitute excited state configurations having their global minimum at the 4×1 phase. Thereby it is found that the speed of the transition is scalable by the excitation strength. Corresponding to the larger gradient of the PES, involving one electron (green) compared to the half-electron excitation (red), the phase change in the former case occurs much faster, with a time constant of about 400 rather than 700 femtoseconds, cf. Fig. 4.19, right.

An analysis of the atoms' movement shows that the energy of the excited electron configurations is at first primarily transformed into the indium structural degrees of freedom. There exists an aligned movement in the phase space of all atoms towards the 4×1 phase before the phase transition completes (mainly the shear and rotational mode, analyzed in Sec. 4.2.1).

After the 4×1 phase is reached, the atoms' movement dephases quickly in the high-dimensional phase space[6]. Moreover, the shear and rotational mode can excite further phonon modes which do not lead to an aligned movement back towards the 8×2 phase. Instead one finds oscillations around the 4×1 phase and an energy dissipation into the substrate, thereby heating it up.

To support these findings quantitatively, further MD simulations on the ground-state PES are performed. Here, the starting velocities are initialized according to the pattern of the shear (18 cm^{-1}) and rotational (27 cm^{-1}) mode, which were already visualized in Fig. 4.13. By making

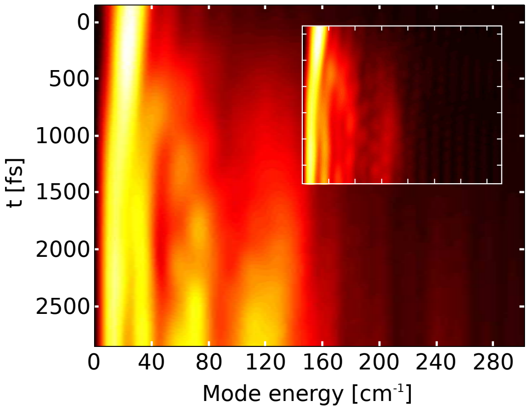

Figure 4.20: Short time Fourier transformation of the atom velocities obtained by a molecular dynamic simulation with only two phonon modes (18 cm^{-1} & 27 cm^{-1}) excited at $t = 0$. A Welch window[183] of length 1.8 ps is used to reduce the artifacts caused by a limited window size. The inset shows the contributions coming solely from the indium atoms.

---

[6] Already the different frequencies of the shear and rotational mode lead to a "wrong" phase for a direct back oscillation.

use of the short time Fourier transformation of the atom velocities, one can calculate a time-dependent frequency spectrum which is depicted in Fig. 4.20. As can be seen, at $t = 0$ the two low frequency modes are strongly excited but decay rapidly due to excitations of many different modes with an energy roughly up to 160 meV. This is especially true if one considers the contributions coming solely from the indium atoms (depicted as inset in Fig. 4.20). Already at 200-300 fs, when the transition is close to the 4×1 phase, many modes with higher energies are excited, hence confirming that a fast decay prevents from oscillations between the 8×2 and 4×1 phase as the aligned movement of all atoms is lost.

4.2.4 Excitation thresholds

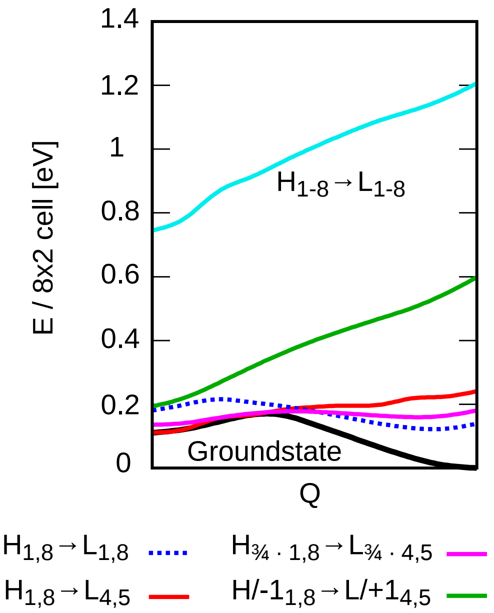

Figure 4.21: Excitation thresholds visualized by means of PES gradients. The green, red and blue curves depict the already known PESs from the previous section. The turquoise PES is based on a full occupation inversion between the highest occupied valence and the lowest unoccupied conduction band (2 e^-). The number of electrons shuffled for the red PES is lowered by 25 % to about 0.4 e^- for the pink one.

After having identified the driving mechanisms and the time dynamics for the optically induced (8×2) $\longrightarrow$ (4×1) phase transition, the question of the lower and a possible upper limit for the excitation strength remains open.

To answer this question, PESs are determined systematically for decreased and increased excitation strengths to probe possible limits. Figure 4.21 shows two PESs additional to the already selected ones from the previous sections. The pink curve depicts the case where the number of charge carriers excited for the red PES is reduced by 25% to around 0.4 e^-, leading to an energy barrier which is minimal over-topped by the starting energy. Therefore, one can roughly estimate that an excitation which involves less than 0.4 e^- per 8×2 unit cell cannot drive the phase transition. In contrast, the turquoise PES is based on a full occupation inversion between the highest occupied valence and the lowest unoccupied conduction band, thereby involving 2.0 e^- per 8×2 unit cell. As can be seen in Fig. 4.21, the gradient between the green (1.0 e^-/8×2 cell) and the turquoise (2.0 e$^-$/8×2 cell) PES does not increase notably. Hence, one can vaguely estimate that the speed of the phase transition saturates at excitations around 1.0 e$^-$/8×2 cell.

These thresholds can also be recognized in Fig. 4.22 which depicts the theoretically predicted phase-transition time constants in dependence on the number of excited electrons in the 8×2 unit cell (blue curve). Moreover, Fig. 4.22 shows the experimentally observed time constants for different exciting laser fluences in red. Similar to the theoretical predictions, the experimental results show also a minimum excitation threshold for fluences at about 0.9 $\mathrm{mJ/cm^2}$ and a saturation of the transition speed for $3\ \mathrm{mJ/cm^2}$. The experimentally observed minimum and maximum time constants as well as the overall progression are thereby in good accordance with the theoretical results. Due to this nice agreement, the laser fluence and the theoretically predicted number of excited electrons can be used to estimate the absorption rate in the surface to about 0.4%.

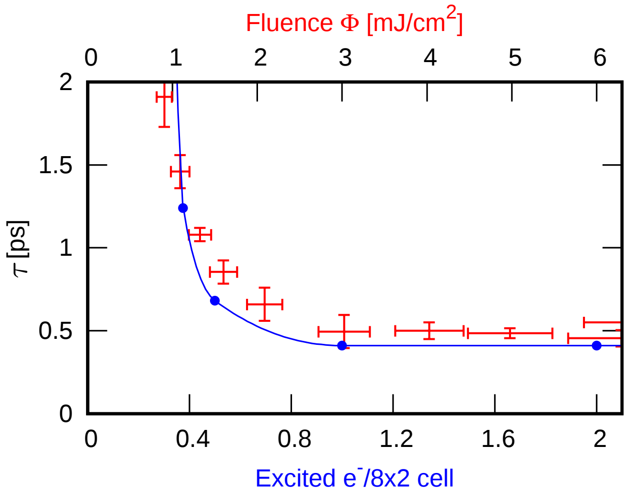

Figure 4.22: Phase-transition time constant τ in dependence on excitation strength. The blue curve depicts the theoretically predicted results for different numbers of excited electrons per 8×2 unit cell. The red points show the experimentally determined transition times of Ref. 153, measured by Tim Frigge in dependence on the exciting laser fluence.

Given that the phase-transition speed saturates for excitations above 1.0 e$^-$/8×2 cell, one wonders whether this is the speed limit for the phase transition in this nanowire system or if there are possibilities speed up the transition. By varying the lattice constant of the silicon substrate, one can add additional strain to the indium nanowires which results into differently steep PESs. Strained silicon can experimentally be obtained by using materials with slightly different lattice constants as substrate for the pseudomorphic epitaxial growth of silicon. For instance, using the germanium compound $\mathrm{Si_{0.7}Ge_{0.3}}$ as substrate can laterally strain the silicon by about 1%[184]. This in-plane strain $\epsilon_{\|}$ leads to a compression of the (111)-silicon layers in growth direction (out-of-plane strain $\epsilon_\perp$), which can be calculated using linear elasticity theory[185,186]

$$\frac{\epsilon_{\|}}{\epsilon_\perp} = -\frac{C_{11} + C_{12} + 4C_{44}}{C_{11} + 2C_{12} + C_{44}}, \tag{4.2}$$

where $C_{11} = 165.6$ GPa, $C_{12} = 63.9$ GPa and $C_{44} = 79.6$ GPa are the stiffness constants of silicon[184,185]. The minus sign in Eq. 4.2 takes into account that a lateral expansion causes a vertical compression and vice versa. This formula is used to calculate the correct vertical strains for several lateral ones. The resulting phase-transition time constants for differently strained silicon substrates are depicted in Fig. 4.23.

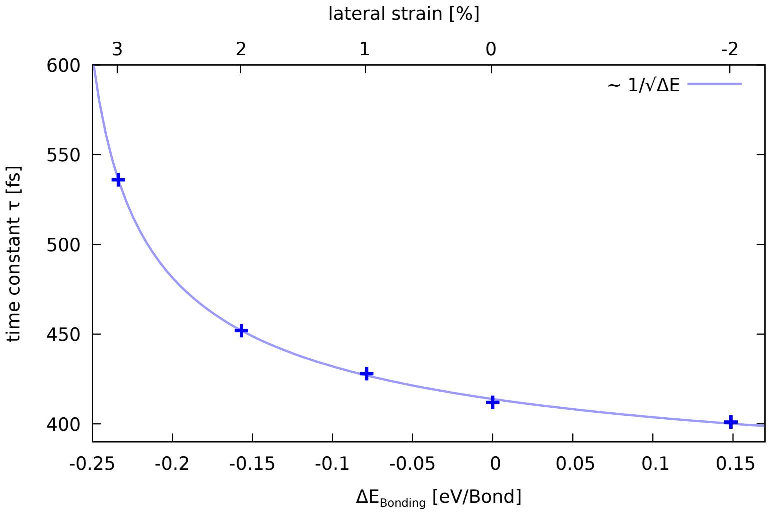

Figure 4.23: Phase-transition time constants in dependence on the applied strain (top axis) and the averaged change in bonding energies in the first layer (bottom axis).

To better characterize the strained systems, also the average bonding energies in the uppermost layer are calculated and plotted on the lower axis (unstrained case as origin). For lateral strains $\geq$ 4% and $\leq$ -3% new phases with different physical behavior are found, therefore Fig. 4.23 is restricted to the range -2% to 3%.

The results show a monotonous decrease of the phase-transition time constant with increasing bonding energies. In a simple picture the bond strengths can be associated with an effective spring constant D which pulls the atoms towards the 4×1 phase. This coherent motion is mainly executed by the two identified phonon modes (cf. Sec. 4.2.1). Since the oscillation speed of a spring pendulum is proportional to $\sqrt{D}$ (and in this simple picture $\sim \sqrt{E_{\text{Bonding}}}$), the phase-transition time in dependence on the bonding energy change might be described by a displaced $1/\sqrt{\Delta E_{\text{Bonding}}}$ function. A corresponding fit is shown in Fig. 4.23 as a slightly blue curve which indeed nicely matches the previously calculated transition times.

In summary, Fig. 4.23 shows that a slight transition speed increase can be achieved by a lateral compression, however, it becomes also clear that the equilibrium unstrained silicon already offers a speed close to the fastest possible optimum.

5

Conclusion

Starting from todays increasing interest in nanostructures and organic semiconductors, the electronic and structural dynamics of materials in various dimensions were examined, using the framework of density functional theory. To realize an in-depth analysis, huge efforts were invested to develop several additional methods and numerical implementations: (i) a polaron description was implemented to investigate temperature dependent charge transport. In addition, (ii) several extensions were written for the molecular editor `Avogadro`[187] to generate and analyze atomic structures. Besides, (iii) the modeling of excited states via constrained occupation was realized by extending the quantum chemistry package `Quantum Espresso`[34]. This extension allows also for tracking ionic movements on an excited potential energy surface. An additionally implemented analysis technique (iv) determines bond strengths, giving access to comprehensible visualizations of the underlying physics.

These methodological developments provided the tools to obtain the results presented in the following. During the investigation of organic semiconductors, special emphasis was given to the transport properties of the polymer Poly(3-hexylthiophene) (P3HT), which is a commonly used conjugated π-system in organic solar cells and field-effect transistors (FETs). All of these applications have in common that the p-type conducting polymer has to offer a conductivity and mobility as high as possible. Since the morphology and degeneration progress has a crucial influence onto the transport properties of a polymer like P3HT, a large number of possible imperfections and defects present in disordered polymer films were modeled and characterized in this thesis. Using a scattering approach, isomerism and small bending defects were identified to have a rather minor influence onto the transport properties. This is in contrast to chain torsions and strong bendings which strongly quench the transport along the affected chains. The latter effect was visualized and related to a reduced overlap of adjacent carbon p_z orbitals. These orbitals constitute the uppermost valence band by forming a delocalized

π-electron system which is severely disturbed and fragmented by these kinds of defects.

The observed fragmentation thereby goes beyond the simple picture of a reduced overlap between adjacent orbitals.

Moreover, polymers like P3HT are susceptible to environmental influences like ambient air. In this context, an oxygen degeneration was investigated by modeling three different kinds of oxygen adsorptions. While an oxygen adsorption to the sulfur atom has negligible effects, an attachment to the carbon backbone has a crucial influence onto the transport properties. This is due to two reasons - on the one hand the oxygen adsorption disturbs also the delocalized π-electron system as it breaks a double bond. On the other hand it causes a structural change in the backbone and reduces the planarity of the thiophene rings.

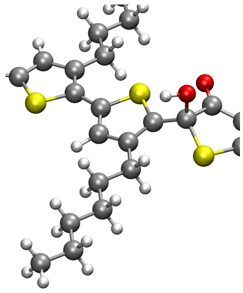

Figure 5.1: One of the analyzed oxygen impurities.

Since the mobility in P3HT is not only limited by static defects, a different theoretical framework was implemented and presented afterwards, to describe also temperature effects. The important coupling between electron and ion dynamics was thereby modeled within a polaron quasiparticle description. In contrast to the coherent scattering approach considered so far, this framework includes the coherent as well as the incoherent, phonon assisted hopping contributions to the total mobility. The required material parameters were calculated from first principles, thereby having access to all phonon patterns and frequencies. A subsequent analysis identified those modes with the largest impact onto the transport properties:

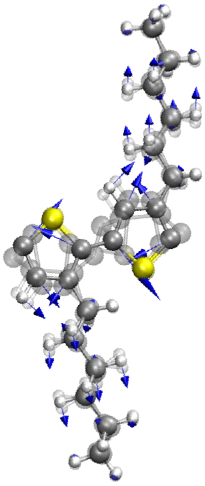

Figure 5.2: One of the important high frequency modes reducing the charge carrier mobility.

It was found that modes affecting the carbon backbone have in general a much larger electron-phonon (el-ph) coupling constant than modes affecting, e.g., the hexyl side chains. As those modes are characterized by oscillations between adjacent atoms, they posses usually much higher frequencies than, e.g., modes bending the full polymer chain. Nevertheless, although these high-energy modes are barely excited at room temperature, it was demonstrated that they have a severe influence onto the mobility already due to their zero point vibrations. Hence, the suppression of these modes gives a further possibility for tuning the transport properties of P3HT, although one has to keep in mind that reducing disorder effects in real polymer films will gain a larger mobility increase.

After the analysis of the transport properties of 1D-P3HT chains and 3D-polymer bulk, the last chapter dealt with a single crystalline system which consists of quasi-1D indium nanowires stabilized by a Si(111) surface. By comparing the relative change in the quantum conductance parallel and perpendicular to the wires upon oxygen adsorption, it was found that the nanowires couple strongly to each other without being directly connected. Such a crosstalk between adjacent wires is a large challenge in electronic chip design on the nanoscale as it increases the leakage current and can causes severe malfunctions.

These nanowires undergo also an interesting insulator-metal transition upon optical excitation, which was recently observed in experiments by the Horn-von Hoegen group in Duisburg on the femtosecond scale[153]. The exciting physics arises thereby from the time-dependent coupled dynamics of electrons and ions. Therefore, the last part of this thesis presented an in-depth analysis and explanation of this phenomenon, to understand the optically driven phase transition from the theory point of view. The microscopic insights were achieved by a detailed density functional theory study for which several of the program extensions mentioned above were necessary; the implementations enabled, e.g., the access to bonding properties during the transition. Moreover, the important electronic states were identified with the help of potential energy surfaces, whose visualization in combination with the bonding analysis gives an intuitive and thorough explanation of the underlying physics. This is especially true for the understanding of the dynamic coupling between the electronic states and the ions movement. Furthermore, potential energy surfaces helped to identify excitation thresholds while additionally performed molecular dynamic simulations provided the opportunity to trace the atomic movements during and subsequent to the phase transition. The thereby obtained theoretical predictions are in strikingly good agreement with the experimental observations - ranging from the excitations thresholds to the phase transition time constants.

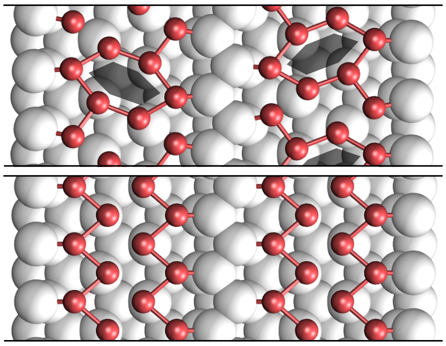

Figure 5.3: The two investigated indium nanowire phases.

The methods developed in the context of this work are in general of broad interest for further work in the field of quantum transport and optically/externally driven phase transitions: Technically, the already mentioned various program modifications and extensions (written during this work) will be of great help (i) to improve the efficiency for creating, editing and analyzing atomic structures (cf. appendix A) and (ii) to have a larger portfolio of postprocessing tools to retrieve physically relevant information like bond strengths. Here, the well documented bond analysis tool will be very helpful in various scenarios, e.g., to characterize phase transitions or chemical adsorption. The developed extensions allow (iii) to unambiguously model frozen excited states with an arbitrary number of $\mathbf{k}$-points or even more technically, but not less important (iv) to restart aborted GW calculations after the wall clock time limit was reached.

Moreover, the mentioned implementation of the polaron transport prediction for organic semiconductors allows, based on material parameters determined from first principles, for an easy and efficient evaluation of the temperature dependent mobility. An application of this code on modified structures will help in tailoring the properties of the investigated materials. For P3HT, one can for instance think about alternative molecular structures which offer an easier processing to less imperfect molecular crystals and a minor appearance of traps induced by high-frequency modes with high polaron binding energies.

Last but not least one has to stress the detailed analysis of the optically driven phase transition from plenty of different perspectives. These range from identified distinctive parts in the band structure over a visualization of the corresponding orbitals and their relation to excited phonon modes up to a comprehensible explanation on the level of bond strengths. This analysis framework is not restricted to the indium nanowires, but can be applied to many other systems undergoing phase transitions or chemical reactions, e.g., in the area of photocatalysis.

A

Extensions and modifications of the molecular editor `Avogadro`

The powerful and open-source molecular editor `Avogadro`[187] was widely used to create, check and manipulate atomic structures for ab initio calculations in this work. To extend the functionality of this program (v. 1.1.0), I developed several extensions in `C++` from which some are shortly presented in the following.

A.1 Input files

`Avogadro` relies on the open-source library `Open Babel` to import and export atom configurations from various chemical file formats. As this library (v. 2.3.2) has only very limited support for `Quantum Espresso`'s input files and no support for its output files, it was necessary to extend this library to work with `Avogadro` in a reasonable way. Thereby the input file was parsed using regular expressions implemented in the `boost` library. Moreover, `Quantum Espresso`'s additional information about fixed atoms in the in- and output files is now kept in mind and can be used for structural relaxations with force field methods inside `Avogadro`.

A.2 Minor Bug fixes and Changes

`Avogadro` offers the possibility to duplicate a unit cell and its atoms in all three lattice directions which can be used, e.g., to build up a larger crystal or to investigate the distances between the atoms of an unit cell and another. However, for some unit cells (e.g., diamond unit cell) this did not work properly.

When copying atoms, `Avogadro` converts the geometry in a more general format (MDL Molefile format), first, before copying it into the clipboard. However, this back and forth conversion did not work reliable and often led to a crashing of `Avogadro` or took a very long time to complete after pasting. To reduce the error-prone overhead, a simple copy & paste routine was added which does only work inside `Avogadro` as it does not make use of the clipboard nor does it convert to a special format. Instead, it provides an exact positioning of the pasted atoms relative to the original atom coordinates.

In addition, I used `Avogadro` to build up systems from scratch adjusting the unit cell size afterwards to the created atomic configuration. However, in the original implementation of `Avogadro`, a resizing of the unit cell led to a scaling of the atom positions by the same factor which was undesired for my purpose.

`Avogadro`, `Open Babel` and `Quantum Espresso` used slightly different constants, e.g., for the conversion between bohr and angstrom. This led to a reduced accuracy in the atomic coordinates every cycle of importing and exporting in `Avogadro`. To overcome this problem, every conversion constant in `Avogadro` and `Open Babel` was adjusted to the one in the `Quantum Espresso` package to be fully compatible.

A.3 Maximize periodic distance

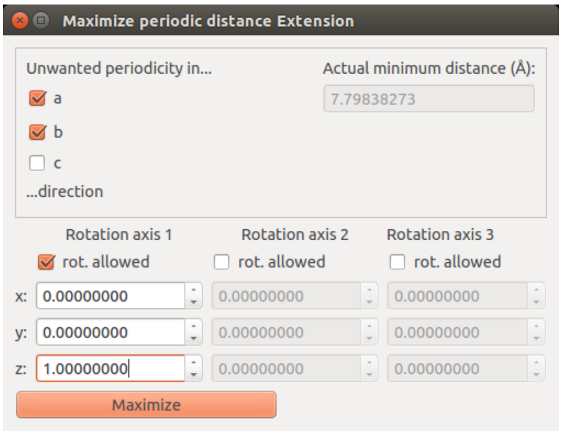
Maximize periodic distance Extension

Unwanted periodicity in...
☑ a
☑ b
☐ c
...direction

Actual minimum distance (Å): 7.79838273

	Rotation axis 1	Rotation axis 2	Rotation axis 3
	☑ rot. allowed	☐ rot. allowed	☐ rot. allowed
x:	0.00000000	0.00000000	0.00000000
y:	0.00000000	0.00000000	0.00000000
z:	1.00000000	0.00000000	0.00000000

Figure A.1: Dialog box of the “Maximize periodic distance Extension”.

The `Quantum Espresso` package makes use of periodic boundary conditions which are not always desired, especially if one wants to deal with surfaces, nanowires or single molecules. The latter require an increased unit cell filled up with vacuum to reduce the influence of the periodic boundary conditions. However, as `Quantum Espresso` relies on a plane wave expansion of the electron wavefunctions, the size of the basis set (and thus the computational effort) increases strongly with the size of the unit cell. To reduce the amount of additional vacuum needed, one can orientate the structure in the unit cell in a way that the distance between the atoms in one cell and in a neighboring one is maximized. This was usual a trial and error work where the molecule was rotated by hand controlled by the displayed distance between two selected atoms from different cells. This approach had also the disadvantage that meanwhile another atom pair can come too close which requires further rotations.

To automate this procedure, I implemented an additional extension into `Avogadro` whose dialog box is pictured in Fig. A.1. It displays the nearest periodic neighbor distance on the top right whereas this value is only evaluated for selected spatial directions on the left. In the lower part the user can provide up to three independent rotational axes which the program uses to maximize the nearest periodic neighbor distance by rotations.

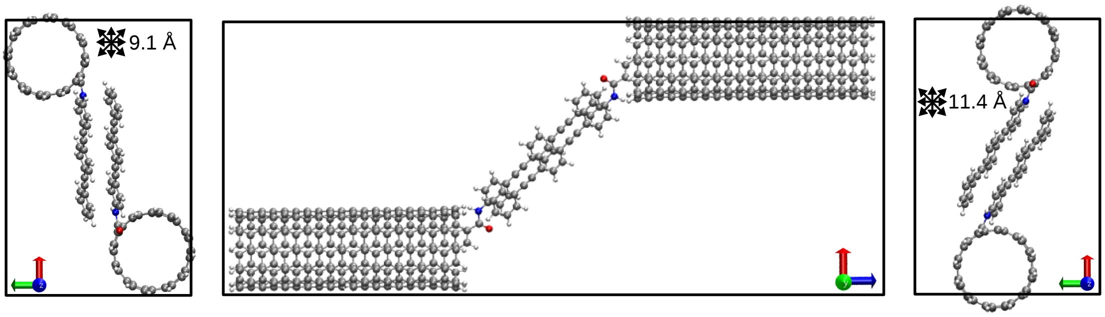

Figure A.2: *Left:* Carbon nanotubes in a unit cell with a nearest periodic neighbor distance of 9.1 Å. *Middle:* Same geometry from the side view. *Right:* Rotated structure by the implemented extension which increased the nearest periodic neighbor distance to 11.4 Å.

Fig. A.2 shows the application of the new extension using an example of carbon nanotubes linked by oligo(phenylene-ethynylene). The goal was to model the conductance of this 1D system so that a periodicity in the plane perpendicular to the nanotubes was undesired. Therefore, it was necessary to increase the unit cell perpendicular to the transport direction in such a way that the nearest periodic neighbor distance is large enough to assume that the influence of the periodicity is negligible.

While the periodic minimum distance is about 9.1 Å in the structure alignment depicted on the left, the extension was able to increase it to 11.4 Å by rotating the geometry around the blue indicated z axis.

A.4 Try to restore a molecule from folded atoms into the unit cell

Some programs (e.g. `VASP`) translate all atoms into the unit cell, which is an equivalent representation due to the periodic boundary conditions. However, these structures are harder to understand as the visualization of them shows only connected fragments (cf. left hand side of Fig. A.3).

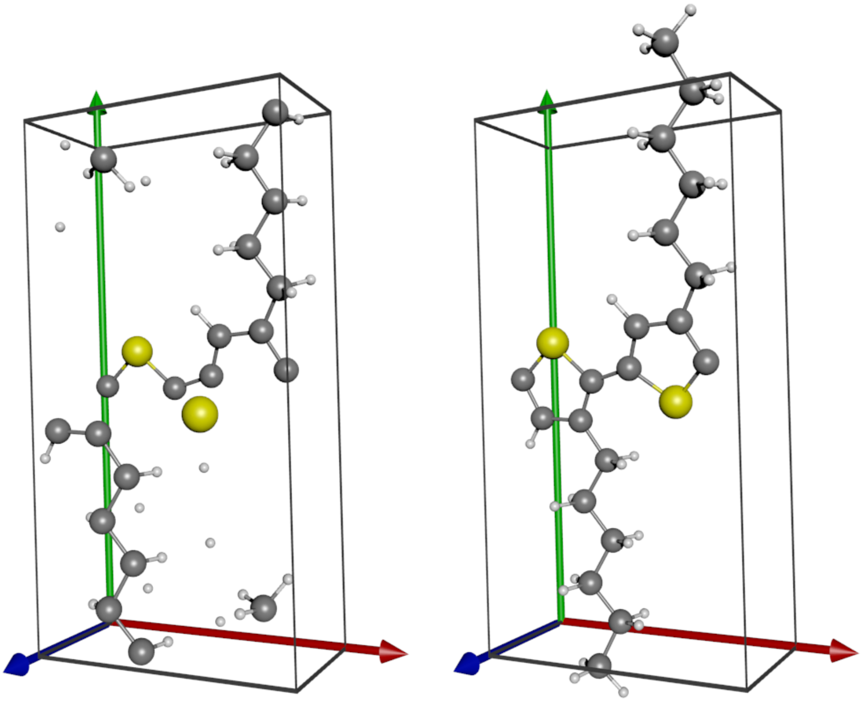

Figure A.3: *Left:* All atoms are folded into the unit cell. *Right:* New extension restored the full molecule.

To restore the original geometry I developed a further extensions which tries to maximize the size of the fragments which ideally leads to only one fragment containing all the atoms. Thereby the extension makes use of the fact that the atoms can be moved by multiples of the lattice vectors without changing the physical structure. An exemplary result of the extension is depicted in Fig. A.3, right.

A.5 Show `PWCond` system

The quantum conductance code `PWCond` sets up usually onto three different self-consistent field (scf) calculations for the three regions left & right contact as well as the scattering region. The atom positions in this three regions have to be adjusted

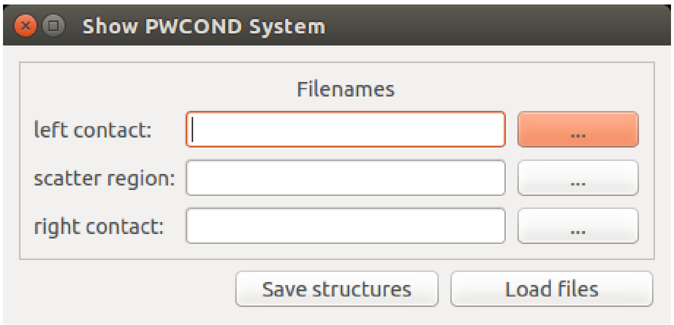

left contact:

scatter region:

right contact:

Figure A.4: Input dialog in which the `Quantum Espresso` input files for the left & right contacts as well as for the scattering region can be selected separately.

in the unit cell to match when they are combined to the overall transport system in `PWCond`.

The implemented extension allows for selecting three different `Quantum Espresso` scf input files (cf. Fig. A.4) whose geometry is afterwards loaded into `Avogadro` and displayed like `PWCond` would arrange it. Moreover, it offers the possibility to adjust the atom positions in the regions to match at the interfaces and to save these changes afterwards back to three files for the left & right contact and the scattering region.

A.6 Measure plane angle

The polymer Poly(3-hexylthiophene) (P3HT) conducts charge carriers mainly along its carbon backbone of the thiophene rings. This transport is very prone to tilting angles between the thiophene ring planes (cf. Fig. A.5 depicting a twisted polymer chain).

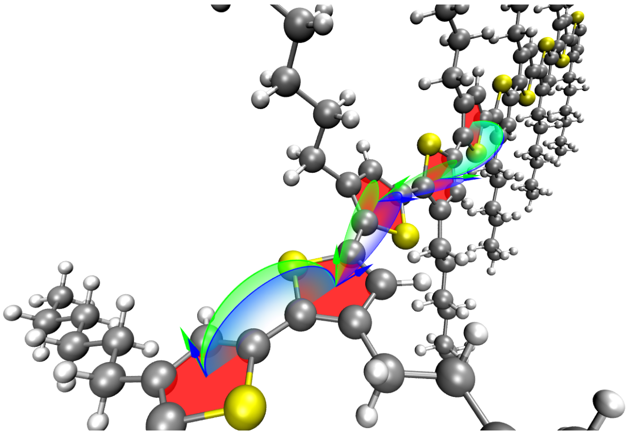

Figure A.5: The angles between two adjacent thiophene rings has a crucial influence onto the transport properties of the polymer P3HT.

To get an easy access to the angles between two adjacent thiophene rings, I implemented a new extension which can calculates the angle between planes. A plane is determined by providing an atom and two bonds which span the plane.

A.7 Put in plane

Especially for aligning molecules as adsorbates onto surfaces I programmed the `Avogadro` extension called "Put in plane". The starting point is a molecule lying in an arbitrary

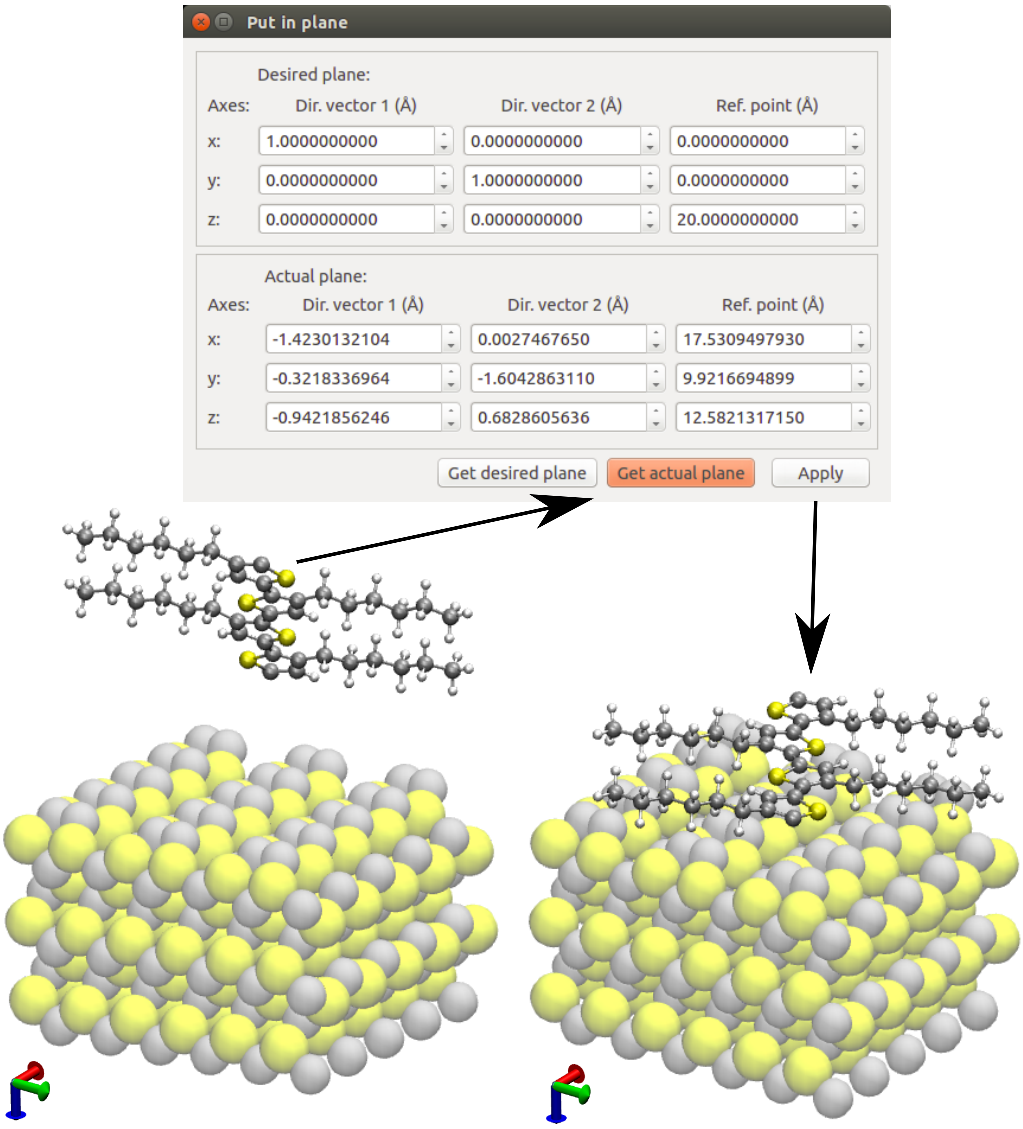

Desired plane:

Axes:	Dir. vector 1 (Å)	Dir. vector 2 (Å)	Ref. point (Å)
x:	1.0000000000	0.0000000000	0.0000000000
y:	0.0000000000	1.0000000000	0.0000000000
z:	0.0000000000	0.0000000000	20.0000000000

Actual plane:

Axes:	Dir. vector 1 (Å)	Dir. vector 2 (Å)	Ref. point (Å)
x:	-1.4230132104	0.0027467650	17.5309497930
y:	-0.3218336964	-1.6042863110	9.9216694899
z:	-0.9421856246	0.6828605636	12.5821317150

Figure A.6: *Left bottom:* SiC surface and an arbitrarily oriented P3HT molecule. *Middle top:* Dialog box for the "Put in plane" extension which asks for the actual and the desired plane. Both planes can optionally be determined by the extension by providing an atom and two bonds spanning the plane. *Right bottom:* Aligned molecule onto the SiC surface by the extension.

plane which should be aligned parallel to the surface. Figure A.6 depicts this situation in the lower left part for a P3HT molecule whose thiophene ring planes should be aligned parallel to a silicon carbide (SiC) surface. By selecting an atom and two bonds of one thiophene ring the extension determines the actual plane of the molecule. Moreover, the new plane can be specified in the upper part of the dialog box in Fig. A.6 - in this case it is the xy plane with an offset of 20 Å to the origin along the z direction.

The lower right of Fig. A.6 shows the aligned molecule after clicking the "Apply" button.

B

Publications

The author of this thesis has contributed to the following publications so far:

- W. B. Dapp, A. Lücke, B. N. J. Persson, and M. H. Müser. Self-affine elastic contacts: Percolation and leakage. *Phys. Rev. Lett.*, 108:244301, Jun 2012. doi: `10.1103/PhysRevLett.108.244301`
- V. Ardizzone, P. Lewandowski, Y. C. Tse, N. H. Kwong, M. H. Luk, A. Lücke, M. Abbarchi, E. Baudin, J. Bloch, A. Lemaitre, P. T. Leung, P. Roussignol, R. Binder, J. Tignon, and S. Schumacher. Formation and control of turing patterns from interacting polaritons in coupled semiconductor microcavities. In *CLEO: 2013*, pages 1–2, June 2013. doi: `10.1364/CLEO_QELS.2013.QTh4E.7`
- V. Ardizzone, P. Lewandowski, M. H. Luk, Y. C. Tse, N. H. Kwong, A. Lücke, M. Abbarchi, E. Baudin, E. Galopin, J., and et al. Formation and control of turing patterns in a coherent quantum fluid. *Scientific Reports*, 3, Oct 2013. ISSN 2045-2322. doi: `10.1038/srep03016`
- P. Lewandowski, V. Ardizzone, Y. C. Tse, N. H. Kwong, M. H. Luk, A. Lücke, M. Abbarchi, J. Bloch, E. Baudin, E. Galopin, A. Lemaître, P. T. Leung, Ph. Roussignol, R. Binder, J. Tignon, and S. Schumacher. Formation and control of transverse patterns in a quantum fluid of microcavity polaritons, *Proc. SPIE* 8984, 2014. doi: `10.1117/12.2037174`
- U. Gerstmann, N. J. Vollmers, A. Lücke, M. Babilon, and W. G. Schmidt. Rashba splitting and relativistic energy shifts in In/Si(111) nanowires. *Phys. Rev. B*, 89: 165431, Apr 2014. doi: `10.1103/PhysRevB.89.165431`
- S. Sanna, U. Gerstmann, E. Rauls, Y. Li, M. Landmann, A. Riefer, M. Rohrmüller, N. J. Vollmers, M. Witte, R Hölscher, A. Lücke, C. Braun, S. Neufeld, K Holtgrewe, and W. G. Schmidt. Surface Charge of Clean LiNbO3 Z-Cut Surfaces.

High Performance Computing in Science and Engineering '14, pages 163–178, Dec 2014. doi: `10.1007/978-3-319-10810-0_12`

- A. Lücke, W.G. Schmidt, E. Rauls, F. Ortmann, and U. Gerstmann. Influence of Structural Defects and Oxidation onto Hole Conductivity in P3HT. *J. Phys. Chem. B*, 119(21):6481–6491, May 2015. ISSN 1520-5207. doi: `10.1021/acs.jpcb.5b03615`
- F. Edler, I. Miccoli, S. Demuth, H. Pfnür, S. Wippermann, A. Lücke, W. G. Schmidt, and C. Tegenkamp. Interwire coupling for In(4 × 1)/Si(111) probed by surface transport. *Phys. Rev. B*, 92:085426, Aug 2015. doi: `10.1103/PhysRevB.92.085426`
- A. Lücke, F. Ortmann, M. Panhans, S. Sanna, E. Rauls, U. Gerstmann, and W. G. Schmidt. Temperature-Dependent Hole Mobility and Its Limit in Crystal-Phase P3HT Calculated from First Principles. *J. Phys. Chem. B*, 120(24):5572–5580, Jun 2016. ISSN 1520-5207. doi: `10.1021/acs.jpcb.6b03598`
- A. Lücke, U. Gerstmann, S. Sanna, M. Landmann, A. Riefer, M. Rohrmüller, N. J. Vollmers, M. Witte, E. Rauls, R. Hölscher, and et al. Solving the scattering problem for the P3HT on-chain charge transport. *High Performance Computing in Science and Engineering '15*, pages 155–170, 2016. doi: `10.1007/978-3-319-24633-8_10`

Moreover, there are two papers already submitted and a further one accepted for publication:

- D. Nozaki, A. Lücke, and W. G. Schmidt. Molecular Orbital Rule for Quantum Interference in Weakly Coupled Dimers: Low-Energy Giant Conductance Switching Induced by Orbital Level Crossing. Submitted to *J. Phys. Chem. Lett.*, 2016.
- A. Lücke, U. Gerstmann, and W.G. Schmidt. Efficent PAW-based COHP analysis for understanding the In/Si(111)(8×2) – (4×1) phase transition. Submitted to *J. Comput. Chem.*, 2017.
- T. Frigge, B. Hafke, T. Witte, B. Krenzer, C. Streubühr, A. Samad Syed, V. Mikšić Trontl, P. Zhou I. Avigo, M. Ligges, D. von der Linde, U. Bovensiepen, M. Horn von Hoegen, S. Wippermann, A. Lücke, S. Sanna, U. Gerstmann, and W. G. Schmidt. Optically excited structural transition in atomic wires on surfaces at the quantum limit. Accepted for publication in *Nature*, 2017.

Acronyms

AE all-electron 11–13, 35
APW augmented plane wave 10

B3LYP Becke, three-parameter, Lee-Yang-Parr 9
BZ Brillouin zone 38, 74, 76, 79, 81–84, 87–89, 138

COHP crystal orbital Hamilton population 34–36, 38, 39, 85–90, 134, 138, 139

DFT density functional theory 3, 6, 20, 38, 43, 59–61, 72, 75, 97, 136
DFT-D2 DFT including dispersion correction according to Grimme[27] 43, 55, 60
DOS density of states 57, 59

el-ph electron-phonon 30, 33, 59, 61, 62, 66, 68, 96, 136

FET field-effect transistor 41, 95
FFT fast Fourier transform 10, 21
FTIR Fourier transform infrared spectroscopy 62

GGA generalized gradient approximation 7, 9, 10, 38, 43, 60
GSL GNU Scientific Library 63
GW Self energy Σ of a many-body system is expressed as a truncated expansion of the single particle Green's function G and the screened Coulomb interaction W 8, 79, 80, 98
$\mathbf{G_0W_0}$ Approximations are used for $G \rightarrow G_0$ and $W \rightarrow W_0$ in GW calculations 79, 80

HH head-to-head 52, 135

HSE06 Heyd-Scuseria-Ernzerhof 9

HT head-to-tail 52

HVB highest valence band 47, 49–51, 57, 58, 60, 68, 69, 81, 134–136, 138

LCB lowest conduction band 81, 138

LDA local density approximation 7, 9, 10, 55, 75

LMTO linear muffin-tin orbital 34

MD molecular dynamic 55, 76, 90, 91, 97, 139

MPI Message Passing Interface 37, 64

OLED organic light-emitting diode 2

OpenMP Open Multi-Processing 38

P3HT Poly(3-hexylthiophene) 2, 3, 14, 33, 41–48, 50, 52, 54–70, 72, 74, 95, 96, 103, 105, 134–136, 140

HT-P3HT head-to-tail P3HT 52, 135

rr-HT-P3HT regioregular head-to-tail P3HT 51, 53, 55, 56, 135

PAW projector augmented wave 11, 13, 34–37

PBE exchange-correlation functional suggested by Perdew, Burke and Ernzerhof 9, 38, 43, 60, 75

PCBM Phenyl-C61-butyric acid methyl ester 58

pDOS projected density of states 56, 57, 136

PES potential energy surface 76, 78, 82–84, 86–93, 95, 97, 137, 139

RAM random-access memory 37

RHEED reflection high energy electron diffraction 75

scf self-consistent field 47, 77

SoC system on chip 1

STM scanning tunneling microscope 72

TT tail-to-tail 52, 135

VBM valence band maximum 44, 47, 53, 56, 57

vdW van der Waals 10, 48

WKB Wentzel-Kramers-Brillouin 44, 45, 134

`VASP` Vienna Ab initio Simulation Package 39, 59, 79, 80, 102

Bibliography

[1] Gordon E. Moore. Cramming more components onto integrated circuits. *Proceedings of the IEEE*, 86:82–85, 1998.

[2] Intel Corporation. Ultra-fast, energy-sipping devices powered by intel. URL `http://www.intel.com/content/www/us/en/silicon-innovations/intel-14nm-technology.html`.

[3] T. Standaert, G. Beique, H. C. Chen, S. T. Chen, B. Hamieh, J. Lee, P. McLaughlin, J. McMahon, Y. Mignot, F. Mont, K. Motoyama, S. Nguyen, R. Patlolla, B. Peethala, D. Priyadarshini, M. Rizzolo, N. Saulnier, H. Shobha, S. Siddiqui, T. Spooner, H. Tang, O. van der Straten, E. Verduijn, Y. Xu, X. Zhang, J. Arnold, D. Canaperi, M. Colburn, D. Edelstein, V. Paruchuri, and G. Bonilla. BEOL process integration for the 7 nm technology node. In *2016 IEEE International Interconnect Technology Conference / Advanced Metallization Conference (IITC/AMC)*, pages 2–4, May 2016. doi: 10.1109/IITC-AMC.2016.7507636.

[4] Professor Sir Richard Friend. Organic solar cells, August 2009. URL `http://www.cam.ac.uk/research/news/organic-solar-cells`.

[5] Wolfgang Nolting. *Grundkurs Theoretische Physik 7*. Springer Dordrecht Heidelberg London New York, 7. auflage edition, 2009.

[6] M. Born and R. Oppenheimer. Zur Quantentheorie der Molekeln. *Annalen der Physik*, 389:457–484, 1927.

[7] P. Hohenberg and W. Kohn. Inhomogeneous electron gas. *Phys. Rev.*, 136: B864–B871, 1964.

[8] Walter Kohn. Electronic structure of matter - wave functions and density functionals. *Nobel Lecture*, pages 213–237, 1999.

[9] D. R. Hartree. The wave mechanics of an atom with a non-coulomb central field. part II. some results and discussion. *Mathematical Proceedings of the Cambridge Philosophical Society*, 24(01):111, Jan 1928. ISSN 1469-8064. doi: 10.1017/s0305004100011920.

[10] V. Fock. Naeherungsmethode zur loesung des quantenmechanischen mehrkoerperproblems. *Zeitschrift fuer Physik*, 61:126–148, 1930.

[11] J. P. Perdew and Alex Zunger. Self-interaction correction to density-functional approximations for many-electron systems. *Phys. Rev. B*, 23:5048–5079, May 1981. doi: 10.1103/PhysRevB.23.5048.

[12] J. P. Perdew. *Electronic structure of solids' 91*, volume 11. Akademie Verlag, Berlin, 1991.

[13] John Perdew, Kieron Burke, and Matthias Ernzerhof. Generalized gradient approximation made simple [Phys. Rev. Lett. 77, 3865 (1996)]. *Phys. Rev. Lett.*, 78(7):1396, 1997. ISSN 0031-9007. doi: 10.1103/PhysRevLett.78.1396.

[14] John Perdew, Kieron Burke, and Matthias Ernzerhof. Generalized gradient approximation made simple. *Phys. Rev. Lett.*, 77(18):3865–3868, 1996. ISSN 0031-9007. doi: 10.1103/PhysRevLett.77.3865.

[15] Axel D. Becke. A new mixing of Hartree–Fock and local density-functional theories. *J. Chem. Phys.*, 98(2):1372–1377, 1993. doi: 10.1063/1.464304.

[16] Chengteh Lee, Weitao Yang, and Robert G. Parr. Development of the Colle-Salvetti correlation-energy formula into a functional of the electron density. *Phys. Rev. B*, 37:785–789, Jan 1988. doi: 10.1103/PhysRevB.37.785.

[17] P. J. Stephens, F. J. Devlin, C. F. Chabalowski, and M. J. Frisch. Ab initio calculation of vibrational absorption and circular dichroism spectra using density functional force fields. *Phys. Chem.*, 98:11623–11627, 94.

[18] Jochen Heyd, Gustavo E. Scuseria, and Matthias Ernzerhof. Hybrid functionals based on a screened coulomb potential. *J. Chem. Phys.*, 124:219906, 2003.

[19] J. L. Lagrange. *Mécanique Analytique*, volume 1. Paris, Ve Courcier, 1811.

[20] W. Kohn and L. J. Sham. Self-consistent equations including exchange and correlation effects. *Phys. Rev.*, 140:A1133–A1138, 1965.

[21] F Aryasetiawan and O Gunnarsson. The GW method. *Reports on Progress in Physics*, 61(3):237–312, Mar 1998. ISSN 1361-6633. doi: 10.1088/0034-4885/61/3/002.

[22] Richard M. Martin. *Electronic structure : basic theory and practical methods*. Cambridge University Press, Cambridge, New York, 2004. ISBN 0-521-78285-6.

[23] M. Shishkin and G. Kresse. Implementation and performance of the frequency-dependent gw method within the PAW framework. *Phys. Rev. B*, 74:035101, Jul 2006. doi: 10.1103/PhysRevB.74.035101.

[24] Jorge Kohanoff. *Electronic Structure Calculation for Solids and Molecules*. Cambridge University Press, 2006.

[25] D. M. Ceperley and B. J. Alder. Ground state of the electron gas by a stochastic method. *Phys. Rev. Let.*, 45:566–569, 1980.

[26] J. P. Perdew and A. Zunger. Self-interaction correction to density-functional approximations for many-electron systems. *Phys. Rev. B*, 23:5048–5079, 1981.

[27] Stefan Grimme. Semiempirical GGA-type density functional constructed with a long-range dispersion correction. *J. Comput. Chem.*, 27(15):1787–1799, 2006. ISSN 0192-8651. doi: 10.1002/jcc.20495.

[28] J. C. Slater. An augmented plane wave method for the periodic potential problem. *Phys. Rev.*, 92(3):603–608, Nov 1953. ISSN 0031-899X. doi: 10.1103/physrev.92.603.

[29] M. C. Payne, M. P. Teter, D. C. Allan, T. A. Arias, and J. D. Joannopoulos. Iterative minimization techniques for *ab initio* total-energy calculations: molecular dynamics and conjugate gradients. *Rev. Mod. Phys.*, 64:1045–1097, Oct 1992. doi: 10.1103/RevModPhys.64.1045.

[30] Warren E. Pickett. Pseudopotential methods in condensed matter applications. *Computer Physics Reports*, 9:115–197, 1989.

[31] U. von Barth and C. D. Gelatt. Validity of the frozen-core approximation and pseudopotential theory for cohesive energy calculations. *Phys. Rev. B*, 21:2222–2228, 1980.

[32] P. E. Bloechl. Projector augmented-wave method. *Phys. Rev. B*, 50:17953–17979, 1994.

[33] Peter E. Blöchl, O. Jepsen, and O. K. Andersen. Improved tetrahedron method for brillouin-zone integrations. *Phys. Rev. B*, 49(23):16223–16233, 1994. ISSN 1098-0121. doi: 10.1103/PhysRevB.49.16223.

[34] Paolo Giannozzi, Stefano Baroni, Nicola Bonini, Matteo Calandra, Roberto Car, Carlo Cavazzoni, Davide Ceresoli, Guido L. Chiarotti, Matteo Cococcioni, Ismaila Dabo, Andrea Dal Corso, Stefano de Gironcoli, Stefano Fabris, Guido Fratesi, Ralph Gebauer, Uwe Gerstmann, Christos Gougoussis, Anton Kokalj, Michele Lazzeri, Layla Martin-Samos, Nicola Marzari, Francesco Mauri, Riccardo Mazzarello, Stefano Paolini, Alfredo Pasquarello, Lorenzo Paulatto, Carlo Sbraccia,

Sandro Scandolo, Gabriele Sclauzero, Ari P. Seitsonen, Alexander Smogunov, Paolo Umari, and Renata M. Wentzcovitch. Quantum espresso: a modular and open-source software project for quantum simulations of materials. *J. Phys. Condens. Matter*, 21(39):395502, 2009. ISSN 0953-8984. doi: 10.1088/0953-8984/21/39/395502.

[35] Supriyo Datta. *Electronic Transport in Mesoscopic Systems*. Cambridge University Press (CUP), 1995. ISBN 9780511805776. doi: 10.1017/cbo9780511805776.

[36] Horst Hoffmann J. Vancea and K. Kastner. Mean free path and effective density of conduction electrons in polycrystalline metal films. *Thin Solid Films*, 121: 201–216, 1984.

[37] Hyoung Joon Choi and Jisoon Ihm. Ab initio pseudopotential method for the calculation of conductance in quantum wires. *Phys. Rev. B*, 59:2267–2275, 1999.

[38] Alexander Smogunov, Andrea Dal Corso, and Erio Tosatti. Ballistic conductance of magnetic Co and Ni nanowires with ultrasoft pseudopotentials. *Phys. Rev. B*, 70:045417, 2004.

[39] Marco Buongiorno Nardelli. Electronic transport in extended systems: Application to carbon nanotubes. *Phys. Rev. B*, 60:7828–7833, Sep 1999. doi: 10.1103/PhysRevB.60.7828.

[40] Frank Ortmann, Friedhelm Bechstedt, and Karsten Hannewald. Theory of charge transport in organic crystals: Beyond holstein's small-polaron model. *Phys. Rev. B*, 79(23), 2009. ISSN 1098-0121. doi: 10.1103/PhysRevB.79.235206.

[41] K. Hannewald. Theory of polaron bandwidth narrowing in organic molecular crystals. *Phys. Rev. B*, 69(7):075211, 2004. ISSN 1098-0121. doi: 10.1103/PhysRevB.69.075211.

[42] Frank Ortmann, Friedhelm Bechstedt, and Karsten Hannewald. Charge transport in organic crystals: interplay of band transport, hopping and electron–phonon scattering. *New J. Phys.*, 12(2):023011, 2010. ISSN 1367-2630. doi: 10.1088/1367-2630/12/2/023011.

[43] Frank Ortmann, Friedhelm Bechstedt, and Karsten Hannewald. Charge transport in organic crystals: Theory and modelling. *Phys. Status Solidi B*, 248(3):511–525, 2011. ISSN 03701972. doi: 10.1002/pssb.201046278.

[44] Carlo Motta and Stefano Sanvito. Charge transport properties of durene crystals from first-principles. *J. Chem. Theory Comput.*, 10(10):4624–4632, Oct 2014. ISSN 1549-9626. doi: 10.1021/ct500390a.

[45] Frank Ortmann, Karsten Hannewald, and Friedhelm Bechstedt. Charge transport

in guanine-based materials. *J. Phys. Chem. B*, 113(20):7367–7371, 2009. ISSN 1520-6106. doi: 10.1021/jp901029t.

[46] Ryogo Kubo. Statistical-mechanical theory of irreversible processes. i. general theory and simple applications to magnetic and conduction problems. *J. Phys. Soc. Jpn.*, 12(6):570–586, 1957. ISSN 0031-9015. doi: 10.1143/JPSJ.12.570.

[47] K. Hannewald and P. A. Bobbert. Anisotropy effects in phonon-assisted charge-carrier transport in organic molecular crystals. *Phys. Rev. B*, 69(7), 2004. ISSN 1098-0121. doi: 10.1103/PhysRevB.69.075212.

[48] Timothy Hughbanks and Roald Hoffmann. Chains of trans-edge-sharing molybdenum octahedra: metal-metal bonding in extended systems. *J. Am. Chem. Soc.*, 105(11):3528–3537, 1983. ISSN 0002-7863. doi: 10.1021/ja00349a027.

[49] Gordon J. Miller. Solids and surfaces: A chemist's view of bonding in extended structures. *Angewandte Chemie*, 101(11):1570–1571, 1989. ISSN 00448249. doi: 10.1002/ange.19891011137.

[50] Richard Dronskowski and Peter E. Blöchl. Crystal orbital hamilton populations (COHP): energy-resolved visualization of chemical bonding in solids based on density-functional calculations. *J. Phys. Chem.*, 97(33):8617–8624, 1993. ISSN 0022-3654. doi: 10.1021/j100135a014.

[51] Alexei Grechnev, Rajeev Ahuja, and Olle Eriksson. Balanced crystal orbital overlap population – a tool for analysing chemical bonds in solids. *J. Phys. Condens. Matter*, 15(45):7751–7761, 2003. ISSN 0953-8984. doi: 10.1088/0953-8984/15/45/014.

[52] Daniel Sanchez-Portal, Emilio Artacho, and Jose M. Soler. Projection of plane-wave calculations into atomic orbitals. *Solid State Communications*, 95(10):685–690, 1995. ISSN 00381098. doi: 10.1016/0038-1098(95)00341-X.

[53] Daniel Sánchez-Portal, Emilio Artacho, and José M. Soler. Analysis of atomic orbital basis sets from the projection of plane-wave results. *J. Phys. Condens. Matter*, 8(21):3859–3880, 1996. ISSN 0953-8984. doi: 10.1088/0953-8984/8/21/012.

[54] M. D. Segall, C. J. Pickard, R. Shah, and M. C. Payne. Population analysis in plane wave electronic structure calculations. *Molecular Physics*, 89(2):571–577, 1996. ISSN 0026-8976. doi: 10.1080/00268979609482494.

[55] M. D. Segall, R. Shah, C. J. Pickard, and M. C. Payne. Population analysis of plane-wave electronic structure calculations of bulk materials. *Phys. Rev. B*, 54(23):16317–16320, 1996. ISSN 1098-0121. doi: 10.1103/PhysRevB.54.16317.

[56] Volker L. Deringer, Andrei L. Tchougréeff, and Richard Dronskowski. Crystal orbital hamilton population (COHP) analysis as projected from plane-wave basis sets. *J. Phys. Chem. A*, 115(21):5461–5466, 2011. ISSN 1520-5215. doi: 10.1021/jp202489s.

[57] Stefan Maintz, Volker L. Deringer, Andrei L. Tchougréeff, and Richard Dronskowski. Analytic projection from plane-wave and PAW wavefunctions and application to chemical-bonding analysis in solids. *Journal of computational chemistry*, 34(29):2557–2567, 2013. ISSN 1096-987X. doi: 10.1002/jcc.23424.

[58] Stefan Maintz, Volker L. Deringer, Andrei L. Tchougréeff, and Richard Dronskowski. LOBSTER: a tool to extract chemical bonding from plane-wave based DFT. *Journal of computational chemistry*, 37(11):1030–1035, 2016. ISSN 1096-987X. doi: 10.1002/jcc.24300.

[59] P. E. Blöchl. Projector augmented-wave method. *Phys. Rev. B*, 50(24):17953–17979, 1994. ISSN 1098-0121. doi: 10.1103/PhysRevB.50.17953.

[60] Felix Bloch. Über die Quantenmechanik der Elektronen in Kristallgittern. *Z. Physik (Zeitschrift für Physik)*, 52(7-8):555–600, 1929. doi: 10.1007/BF01339455.

[61] Per-Olov Löwdin. On the non-orthogonality problem connected with the use of atomic wave functions in the theory of molecules and crystals. *J. Chem. Phys.*, 18(3):365, 1950. ISSN 00219606. doi: 10.1063/1.1747632.

[62] P. C. Pattnaik, J. L. Fry, N. E. Brener, and G. Fletcher. Use of ATM in evaluating spin-density. *Int. J. Quantum Chem.*, 20(S15):499–505, 1981. ISSN 00207608. doi: 10.1002/qua.560200854.

[63] R. J. Kline and M. D. McGehee. Morphology and charge transport in conjugated polymers. *J. Macromol. Sci., Polym. Rev.*, 46(1):27–45, 2006. ISSN 1532-1797. doi: 10.1080/15321790500471194.

[64] Veaceslav Coropceanu, Jérôme Cornil, da Silva Filho, Demetrio A., Yoann Olivier, Robert Silbey, and Jean-Luc Brédas. Charge transport in organic semiconductors. *Chem. Rev.*, 107(4):926–952, 2007. ISSN 0009-2665. doi: 10.1021/cr050140x.

[65] Jenny Nelson, Joe J. Kwiatkowski, James Kirkpatrick, and Jarvist M. Frost. Modeling charge transport in organic photovoltaic materials. *Acc. Chem. Res.*, 42(11):1768–1778, 2009. ISSN 1520-4898. doi: 10.1021/ar900119f.

[66] Patrick Pingel, Achmad Zen, Ruben D. Abellón, Ferdinand C. Grozema, Laurens D.A. Siebbeles, and Dieter Neher. Temperature-resolved local and macroscopic charge carrier transport in thin P3HT layers. *Adv. Funct. Mater.*, 20(14):2286–2295, 2010. ISSN 1616301X. doi: 10.1002/adfm.200902273.

[67] Rodrigo Noriega, Jonathan Rivnay, Koen Vandewal, Koch, Felix P V, Natalie Stingelin, Paul Smith, Michael F. Toney, and Alberto Salleo. A general relationship between disorder, aggregation and charge transport in conjugated polymers. *Nat. Mater.*, 12(11):1038–1044, 2013. ISSN 1476-1122. doi: 10.1038/nmat3722.

[68] Edward J. W. Crossland, Kim Tremel, Florian Fischer, Khosrow Rahimi, Günter Reiter, Ullrich Steiner, and Sabine Ludwigs. Anisotropic charge transport in spherulitic poly(3-hexylthiophene) films. *Adv. Mater.*, 24(6):839–844, 2012. ISSN 09359648. doi: 10.1002/adma.201104284.

[69] Yi-Kang Lan and Ching-I Huang. A theoretical study of the charge transfer behavior of the highly regioregular poly-3-hexylthiophene in the ordered state. *J. Phys. Chem. B*, 112(47):14857–14862, 2008. ISSN 1520-6106. doi: 10.1021/jp806967x.

[70] Yi-Kang Lan and Ching-I Huang. Charge mobility and transport behavior in the ordered and disordered states of the regioregular poly(3-hexylthiophene). *J. Phys. Chem. B*, 113(44):14555–14564, 2009. ISSN 1520-6106. doi: 10.1021/jp904841j.

[71] Nenad Vukmirović and Lin-Wang Wang. Electronic structure of disordered conjugated polymers: Polythiophenes. *J. Phys. Chem. B*, 113(2):409–415, 2009. ISSN 1520-6106. doi: 10.1021/jp808360y.

[72] David P. McMahon and Alessandro Troisi. Organic semiconductors: Impact of disorder at different timescales. *Chemphyschem*, 11(10):2067–2074, 2010. ISSN 1439-4235. doi: 10.1002/cphc.201000182.

[73] Josiah A. Bjorgaard and Muhammet E. Köse. Theoretical study of torsional disorder in poly(3-alkylthiophene) single chains: Intramolecular charge-transfer character and implications for photovoltaic properties. *J. Phys. Chem. A*, 117 (18):3869–3876, 2013. ISSN 1089-5639. doi: 10.1021/jp401521j.

[74] Nenad Vukmirović and Lin-Wang Wang. Overlapping fragments method for electronic structure calculation of large systems. *J. Chem. Phys.*, 134(9):094119, 2011. doi: 10.1063/1.3560956.

[75] Seth B. Darling and Michael Sternberg. Importance of side chains and backbone length in defect modeling of poly(3-alkylthiophenes). *J. Phys. Chem. B*, 113(18): 6215–6218, 2009. ISSN 1520-6106. doi: 10.1021/jp808045j.

[76] Ferdinand C. Grozema, van Duijnen, Piet Th., Yuri A. Berlin, Mark A. Ratner, and Siebbeles, Laurens D. A. Intramolecular charge transport along isolated chains of conjugated polymers: Effect of torsional disorder and polymerization defects. *J. Phys. Chem. B*, 106(32):7791–7795, 2002. ISSN 1520-6106. doi: 10.1021/jp021114v.

[77] Seth B. Darling. Isolating the effect of torsional defects on mobility and band gap in conjugated polymers. *J. Phys. Chem. B*, 112(30):8891–8895, 2008. ISSN 1520-6106. doi: 10.1021/jp8017919.

[78] Renato Colle, Giuseppe Grosso, Alberto Ronzani, and Claudio M. Zicovich-Wilson. Structure and X-ray spectrum of crystalline poly(3-hexylthiophene) from DFT-van der Waals calculations. *Phys. Status Solidi B*, 248(6):1360–1368, 2011. ISSN 03701972. doi: 10.1002/pssb.201046429.

[79] Fritz London. *Z. Phys. Chem. Abt. B*, (11):222, 1930.

[80] Kazunari Yoshizawa, Takashi Yumura, Tokio Yamabe, and Shunji Bandow. The role of orbital interactions in determining the interlayer spacing in graphite slabs. *J. Am. Chem. Soc.*, 122(48):11871–11875, 2000. ISSN 0002-7863. doi: 10.1021/ja994457o.

[81] F. Ortmann, Wolf Gero Schmidt, and Friedhelm Bechstedt. Attracted by long-range electron correlation: Adenine on graphite. *Phys. Rev. Lett.*, 95(18):186101, 2005. ISSN 0031-9007. doi: 10.1103/PhysRevLett.95.186101.

[82] Hendrik J. Monkhorst and James D. Pack. Special points for brillouin-zone integrations. *Phys. Rev. B*, 13(12):5188–5192, 1976. ISSN 1098-0121. doi: 10.1103/PhysRevB.13.5188.

[83] Mohsen Razavy. *Quantum Theory of Tunneling*. World Scientific, River Edge, NJ, 2003. ISBN 9812380183.

[84] Ferdinand C. Grozema and Siebbeles, Laurens D. A. Charge mobilities in conjugated polymers measured by pulse radiolysis time-resolved microwave conductivity: From single chains to solids. *J. Phys. Chem. Lett.*, 2(23):2951–2958, 2011. ISSN 1948-7185. doi: 10.1021/jz201229a.

[85] W. R. Salaneck, O. Inganäs, B. Thémans, J. O. Nilsson, B. Sjögren, J.-E. Österholm, J. L. Brédas, and S. Svensson. Thermochromism in poly(3-hexylthiophene) in the solid state: A spectroscopic study of temperature-dependent conformational defects. *J. Chem. Phys.*, 89(8):4613–4619, 1988. ISSN 00219606. doi: 10.1063/1.454802.

[86] A. Dkhissi, F. Ouhib, A. Chaalane, Roger C. Hiorns, C. Dagron-Lartigau, P. Iratcabal, J. Desbrieres, and C. Pouchan. Theoretical and experimental study of low band gap polymers for organic solar cells. *PCCP*, 14(16):5613–5619, 2012. ISSN 1463-9076. doi: 10.1039/c2cp40170c.

[87] George Volonakis, Leonidas Tsetseris, and Stergios Logothetidis. Impurity-related effects in poly(3-hexylthiophene) crystals. *PCCP*, 16(46):25557–25563, 2014. ISSN 1463-9084. doi: 10.1039/c4cp03203a.

[88] Orestis Alexiadis and Vlasis G. Mavrantzas. All-atom molecular dynamics simulation of temperature effects on the structural, thermodynamic, and packing properties of the pure amorphous and pure crystalline phases of regioregular P3HT. *Macromolecules*, 46(6):2450–2467, 2013. ISSN 0024-9297. doi: 10.1021/ma302211g.

[89] Jui-Fen Chang, Jenny Clark, Ni Zhao, Henning Sirringhaus, Dag Breiby, Jens Andreasen, Martin Nielsen, Mark Giles, Martin Heeney, and Iain McCulloch. Molecular-weight dependence of interchain polaron delocalization and exciton bandwidth in high-mobility conjugated polymers. *Phys. Rev. B*, 74(11):115318, 2006. ISSN 1098-0121. doi: 10.1103/PhysRevB.74.115318.

[90] Kwan-Yue Jen, G. G. Miller, and Ronald L. Elsenbaumer. Highly conducting, soluble, and environmentally-stable poly(3-alkylthiophenes). *J. Chem. Soc., Chem. Commun.*, (17):1346–1347, 1986. ISSN 0022-4936. doi: 10.1039/c39860001346.

[91] David P. McMahon, David L. Cheung, Ludwig Goris, Javier Dacuña, Alberto Salleo, and Alessandro Troisi. Relation between microstructure and charge transport in polymers of different regioregularity. *J. Phys. Chem. C*, 115(39): 19386–19393, 2011. ISSN 1932-7447. doi: 10.1021/jp207026s.

[92] Andrea Seemann, Tobias Sauermann, Christoph Lungenschmied, Oskar Armbruster, Siegfried Bauer, H.-J. Egelhaaf, and Jens Hauch. Reversible and irreversible degradation of organic solar cell performance by oxygen. *Solar Energy*, 85(6):1238–1249, 2011. ISSN 0038-092X. doi: 10.1016/j.solener.2010.09.007.

[93] Kion Norrman, Morten V. Madsen, Suren A. Gevorgyan, and Frederik C. Krebs. Degradation patterns in water and oxygen of an inverted polymer solar cell. *J. Am. Chem. Soc.*, 132(47):16883–16892, 2010. ISSN 1520-5126. doi: 10.1021/ja106299g.

[94] Matthieu Manceau, Agnès Rivaton, Jean-Luc Gardette, Stéphane Guillerez, and Noëlla Lemaître. The mechanism of photo- and thermooxidation of poly(3-hexylthiophene) (P3HT) reconsidered. *Polym. Degrad. Stab.*, 94(6):898–907, 2009. ISSN 0141-3910. doi: 10.1016/j.polymdegradstab.2009.03.005.

[95] Henning Sirringhaus. Reliability of organic field-effect transistors. *Adv. Mater.*, 21:3859–3873, 2009. ISSN 09359648. doi: 10.1002/adma.200901136.

[96] Julia Schafferhans, Andreas Baumann, Alexander Wagenpfahl, Carsten Deibel, and Vladimir Dyakonov. Oxygen doping of P3HT:PCBM blends: Influence on trap states, charge carrier mobility and solar cell performance. *Org. Electron.*, 11(10):1693–1700, 2010. ISSN 1566-1199. doi: 10.1016/j.orgel.2010.07.016.

[97] Andreas Sperlich, Hannes Kraus, Carsten Deibel, Hubert Blok, Jan Schmidt, and Vladimir Dyakonov. Reversible and irreversible interactions of poly(3-hexylthiophene) with oxygen studied by spin-sensitive methods. *J. Phys. Chem. B*, 115(46):13513–13518, 2011. ISSN 1520-6106. doi: 10.1021/jp2077215.

[98] Nadia Grossiord, Jan M. Kroon, Ronn Andriessen, and Blom, Paul W. M. Degradation mechanisms in organic photovoltaic devices. *Org. Electron.*, 13(3):432–456, 2012. ISSN 1566-1199. doi: 10.1016/j.orgel.2011.11.027.

[99] Steffan Cook, Akihiro Furube, and Ryuzi Katoh. Matter of minutes degradation of poly(3-hexylthiophene) under illumination in air. *J. Mater. Chem.*, 22(10): 4282–4289, 2012. ISSN 0959-9428. doi: 10.1039/C1JM14925C.

[100] Minh Trung Dang, Lionel Hirsch, and Guillaume Wantz. P3HT:PCBM, best seller in polymer photovoltaic research. *Adv. Mater.*, 23(31):3597–3602, 2011. ISSN 09359648. doi: 10.1002/adma.201100792.

[101] Yosuke Kanai and Jeffrey C. Grossman. Insights on interfacial charge transfer across P3HT/fullerene photovoltaic heterojunction from ab initio calculations. *Nano Lett.*, 7(7):1967–1972, 2007. ISSN 1530-6984. doi: 10.1021/nl0707095.

[102] David L. Cheung, David P. McMahon, and Alessandro Troisi. Computational study of the structure and charge-transfer parameters in low-molecular-mass p3ht. *J. Phys. Chem. B*, 113(28):9393–9401, 2009. ISSN 1520-6106. doi: 10.1021/jp904057m.

[103] D. L. Cheung, D. P. McMahon, and A. Troisi. A realistic description of the charge carrier wave function in microcrystalline polymer semiconductors. *J. Am. Chem. Soc.*, 131(31):11179–11186, 2009. ISSN 1520-5126. doi: 10.1021/ja903843c.

[104] Carl Poelking and Denis Andrienko. Effect of polymorphism, regioregularity and paracrystallinity on charge transport in poly(3-hexylthiophene) [P3HT] nanofibers. *Macromolecules*, 46(22):8941–8956, 2013. ISSN 0024-9297. doi: 10.1021/ma4015966.

[105] Carl Poelking, Kostas Daoulas, Alessandro Troisi, and Denis Andrienko. Morphology and charge transport in P3HT: A theorist's perspective. In Sabine Ludwigs, editor, *P3HT Revisited – From Molecular Scale to Solar Cell Devices*, volume 265 of *Advances in Polymer Science*, pages 139–180. Springer Berlin Heidelberg, Berlin, Heidelberg, 2014. ISBN 978-3-662-45144-1. doi: 10.1007/12\textunderscore2014\textunderscore277.

[106] Yow-Jon Lin, Cheng-Lung Tsai, Yu-Chao Su, and Day-Shan Liu. Carrier transport mechanism of poly(3,4-ethylenedioxythiophene) doped with poly(4-

styrenesulfonate) films by incorporating ZnO nanoparticles. *Appl. Phys. Lett.*, 100(25):253302, 2012. ISSN 00036951. doi: 10.1063/1.4730391.

[107] S. Bhattacharya, S. Malik, A. K. Nandi, and A. Ghosh. Transport properties of CdS nanowire embedded poly(3-hexyl thiophene) nanocomposite. *J. Chem. Phys.*, 125(17):174717, 2006. ISSN 0021-9606. doi: 10.1063/1.2370928.

[108] Alberto Salleo. Charge transport in polymeric transistors. *Materials Today*, (3): 38–45, 2007.

[109] Chenchen Wang, Leslie H. Jimison, Ludwig Goris, Iain McCulloch, Martin Heeney, Alexander Ziegler, and Alberto Salleo. Microstructural origin of high mobility in high-performance poly(thieno-thiophene) thin-film transistors. *Adv. Mater.*, (6): 697–701, 2010.

[110] Ammar Khan Muhammad and Jiu-Xun Sun. Improvement of mobility edge model by using new density of states with exponential tail for organic diode. *Chinese Phys. B*, (4):047203, 2015.

[111] Jui-Fen Chang, Henning Sirringhaus, Mark Giles, Martin Heeney, and Iain McCulloch. Relative importance of polaron activation and disorder on charge transport in high-mobility conjugated polymer field-effect transistors. *Phys. Rev. B*, 76 (20):205204, 2007. ISSN 1098-0121. doi: 10.1103/PhysRevB.76.205204.

[112] Frank Ortmann Dr. rer. nat. *Charge Transport in Organic Crystals*. PhD thesis, Oct 2009. URL `https://www.db-thueringen.de/receive/dbt_mods_00014133`.

[113] B. Horovitz, R. Österbacka, and Z. V. Vardeny. Multiple fano effect in charge density wave systems. *Michael J. Rice Memorial Festschrift*, 141(1–2):179–183, 2004. ISSN 0379-6779. doi: 10.1016/j.synthmet.2003.09.019.

[114] R. Österbacka, X. M. Jiang, C. P. An, B. Horovitz, and Z. V. Vardeny. Photoinduced quantum interference antiresonances in π -conjugated polymers. *Phys. Rev. Lett.*, 88(22), 2002. ISSN 0031-9007. doi: 10.1103/PhysRevLett.88.226401.

[115] Guy Louarn, Miroslaw Trznadel, J. P. Buisson, Jadwiga Laska, Adam Pron, Mieczyslaw Lapkowski, and Serge Lefrant. Raman spectroscopic studies of regioregular poly(3-alkylthiophenes). *J. Phys. Chem.*, 100(30):12532–12539, 1996. ISSN 0022-3654. doi: 10.1021/jp960104p.

[116] Andreas Lücke, Frank Ortmann, Michel Panhans, Simone Sanna, Eva Rauls, Uwe Gerstmann, and Wolf Gero Schmidt. Temperature-dependent hole mobility and its limit in crystal-phase P3HT calculated from first principles. *J. Phys. Chem. B*, 120(24):5572–5580, Jun 2016. ISSN 1520-5207. doi: 10.1021/acs.jpcb.6b03598.

[117] A. Salleo, T. W. Chen, A. R. Völkel, Y. Wu, P. Liu, B. S. Ong, and R. A. Street. Intrinsic hole mobility and trapping in a regioregular poly(thiophene). *Phys. Rev. B*, 70(11), 2004. ISSN 1098-0121. doi: 10.1103/PhysRevB.70.115311.

[118] R. A. Street, J. E. Northrup, and A. Salleo. Transport in polycrystalline polymer thin-film transistors. *Phys. Rev. B*, 71(16), 2005. ISSN 1098-0121. doi: 10.1103/PhysRevB.71.165202.

[119] A. Zen, J. Pflaum, S. Hirschmann, W. Zhuang, F. Jaiser, U. Asawapirom, J. P. Rabe, U. Scherf, and D. Neher. Effect of molecular weight and annealing of poly(3-hexylthiophene)s on the performance of organic field-effect transistors. *Adv. Funct. Mater.*, 14(8):757–764, 2004. ISSN 1616301X. doi: 10.1002/adfm.200400017.

[120] Christina Scharsich, Ruth H. Lohwasser, Michael Sommer, Udom Asawapirom, Ullrich Scherf, Mukundan Thelakkat, Dieter Neher, and Anna Köhler. Control of aggregate formation in poly(3-hexylthiophene) by solvent, molecular weight, and synthetic method. *J. Polym. Sci., Part B: Polym. Phys.*, 50(6):442–453, 2012. ISSN 0887-6266. doi: 10.1002/polb.23022.

[121] John Northrup. Atomic and electronic structure of polymer organic semiconductors: P3HT, PQT, and PBTTT. *Phys. Rev. B*, 76(24):245202, 2007. ISSN 1098-0121. doi: 10.1103/PhysRevB.76.245202.

[122] Giuseppe Grosso Riccardo Farchioni, editor. *Organic electronic materials*. 41. Springer, 2001.

[123] R. Joseph Kline, Michael D. McGehee, Ekaterina N. Kadnikova, Jinsong Liu, Jean M. J. Fréchet, and Michael F. Toney. Dependence of regioregular poly(3-hexylthiophene) film morphology and field-effect mobility on molecular weight. *Macromolecules*, 38(8):3312–3319, 2005. ISSN 0024-9297. doi: 10.1021/ma047415f.

[124] Tommie W. Kelley and C. Daniel Frisbie. Gate voltage dependent resistance of a single organic semiconductor grain boundary. *J. Phys. Chem. B*, 105(20): 4538–4540, 2001. ISSN 1520-6106. doi: 10.1021/jp004519t.

[125] Anna B. Chwang and C. Daniel Frisbie. Temperature and gate voltage dependent transport across a single organic semiconductor grain boundary. *J. Appl. Phys.*, 90(3):1342, 2001. ISSN 00218979. doi: 10.1063/1.1376404.

[126] Leslie H. Jimison, Michael F. Toney, Iain McCulloch, Martin Heeney, and Alberto Salleo. Charge-transport anisotropy due to grain boundaries in directionally crystallized thin films of regioregular poly(3-hexylthiophene). *Adv. Mater.*, 21 (16):1568–1572, 2009. ISSN 09359648. doi: 10.1002/adma.200802722.

[127] Chuanjun Liu, Kenji Oshima, Masato Shimomura, and Shinnosuke Miyauchi. Anisotropic conductivity–temperature characteristic of solution-cast poly(3-hexylthiophene) films. *Synth. Met.*, 156(21–24):1362–1367, 2006. ISSN 0379-6779. doi: 10.1016/j.synthmet.2006.10.007.

[128] Siddharth Joshi, Patrick Pingel, Souren Grigorian, Tobias Panzner, Ullrich Pietsch, Dieter Neher, Michael Forster, and Ullrich Scherf. Bimodal temperature behavior of structure and mobility in high molecular weight P3HT thin films. *Macromolecules*, 42(13):4651–4660, 2009. ISSN 0024-9297. doi: 10.1021/ma900021w.

[129] Peter J. Brown, D. Steve Thomas, Anna Köhler, Joanne S. Wilson, Ji-Seon Kim, Catherine M. Ramsdale, Henning Sirringhaus, and Richard H. Friend. Effect of interchain interactions on the absorption and emission of poly(3-hexylthiophene). *Phys. Rev. B*, 67(6), 2003. ISSN 1098-0121. doi: 10.1103/PhysRevB.67.064203.

[130] W. G. Schmidt, S. Wippermann, S. Sanna, M. Babilon, N. J. Vollmers, and U. Gerstmann. In-Si(111)$(4 \times 1)/(8 \times 2)$ nanowires: Electron transport, entropy, and metal-insulator transition. *Phys. Status Solidi B*, 249(2):343–359, 2012. ISSN 03701972. doi: 10.1002/pssb.201100457.

[131] H. W. Yeom, S. Takeda, E. Rotenberg, I. Matsuda, K. Horikoshi, J. Schaefer, C. M. Lee, S. D. Kevan, T. Ohta, T. Nagao, and S. Hasegawa. Instability and charge density wave of metallic quantum chains on a silicon surface. *Phys. Rev. Let.*, 82(24):4898–4901, 1999. ISSN 0031-9007. doi: 10.1103/PhysRevLett.82.4898.

[132] Jun Nakamura, Satoshi Watanabe, and Masakazu Aono. Anisotropic electronic structure of the Si(111)$-(4\times1)$In surface. *Phys. Rev. B*, 63(19), 2001. ISSN 1098-0121. doi: 10.1103/PhysRevB.63.193307.

[133] Jun-Hyung Cho, Dong-Hwa Oh, Kwang S. Kim, and Leonard Kleinman. Weakly correlated one-dimensional indium chains on Si(111). *Phys. Rev. B*, 64(23), 2001. ISSN 1098-0121. doi: 10.1103/PhysRevB.64.235302.

[134] Jun-Hyung Cho, Jung-Yup Lee, and Leonard Kleinman. Electronic structure of one-dimensional indium chains on Si(111). *Phys. Rev. B*, 71(8), 2005. ISSN 1098-0121. doi: 10.1103/PhysRevB.71.081310.

[135] Shiow-Fon Tsay. Atomic and electronic structure of the (4×1) and (8×2)In/Si(111) surfaces. *Phys. Rev. B*, 71(3), 2005. ISSN 1098-0121. doi: 10.1103/PhysRevB.71.035207.

[136] S. Wippermann and W. G. Schmidt. Entropy explains metal-insulator transition of the Si(111)-In nanowire array. *Phys. Rev. Let.*, 105(12):126102, 2010. ISSN 1079-7114. doi: 10.1103/PhysRevLett.105.126102.

[137] W. G. Schmidt, M. Babilon, C. Thierfelder, S. Sanna, and S. Wippermann. Influence of na adsorption on the quantum conductance and metal-insulator transition of the In-Si(111)(4×1)–(8×2) nanowire array. *Phys. Rev. B*, 84 (11), 2011. ISSN 1098-0121. doi: 10.1103/PhysRevB.84.115416.

[138] U. Gerstmann, N. J. Vollmers, A. Lücke, M. Babilon, and W. G. Schmidt. Rashba splitting and relativistic energy shifts in In/Si(111) nanowires. *Phys. Rev. B*, 89 (16), 2014. ISSN 1098-0121. doi: 10.1103/PhysRevB.89.165431.

[139] Hyungjoon Shim, Geunseop Lee, Jung-Min Hyun, and Hanchul Kim. Cooperative interplay between impurities and charge density wave in the phase transition of atomic wires. *New J. Phys.*, 17(9):093026, 2015. ISSN 1367-2630. doi: 10.1088/1367-2630/17/9/093026.

[140] F. Edler, I. Miccoli, S. Demuth, H. Pfnür, S. Wippermann, A. Lücke, W. G. Schmidt, and C. Tegenkamp. Interwire coupling for $\mathrm{In}(4 \times 1)$/Si(111) probed by surface transport. *Phys. Rev. B*, 92:085426, Aug 2015. doi: 10.1103/PhysRevB.92.085426.

[141] C Gonzalez, F Flores, and J Ortega. Soft phonon, dynamical fluctuations, and a reversible phase transition: Indium chains on silicon. *Phys. Rev. Lett.*, 96:136101, 2006.

[142] J. R. Ahn, J. H. Byun, H. Koh, E. Rotenberg, S. D. Kevan, and H. W. Yeom. Mechanism of gap opening in a triple-band peierls system: In atomic wires on Si. *Phys. Rev. Lett.*, 93:106401, Aug 2004. doi: 10.1103/PhysRevLett.93.106401.

[143] Y. J. Sun, S. Agario, S. Souma, K. Sugawara, Y. Tago, T. Sato, and T. Takahashi. Cooperative structural and Peierls transition of indium chains on Si(111). *Phys. Rev. B*, 77:125115, Mar 2008. doi: 10.1103/PhysRevB.77.125115.

[144] S. S. Lee, J. R. Ahn, N. D. Kim, J. H. Min, C. G. Hwang, J. W. Chung, H. W. Yeom, Serguei V. Ryjkov, and Shuji Hasegawa. Adsorbate-induced pinning of a charge-density wave in a quasi-1d metallic chains: Na on the $\mathrm{In/Si}(111) - (4 \times 1)$ surface. *Phys. Rev. Lett.*, 88:196401, Apr 2002. doi: 10.1103/PhysRevLett.88.196401.

[145] Simone Wall, Boris Krenzer, Stefan Wippermann, Simone Sanna, Friedrich Klasing, Anja Hanisch-Blicharski, Martin Kammler, Wolf Gero Schmidt, and Michael Horn-von Hoegen. Atomistic picture of charge density wave formation at surfaces. *Phys. Rev. Lett.*, 109:186101, Nov 2012. doi: 10.1103/PhysRevLett.109.186101.

[146] Takehiro Tanikawa, Iwao Matsuda, Taizo Kanagawa, and Shuji Hasegawa. Surface-

state electrical conductivity at a metal-insulator transition on silicon. *Phys. Rev. Lett.*, 93:016801, Jun 2004. doi: 10.1103/PhysRevLett.93.016801.

[147] S V Ryjkov, T Nagao, V G Lifshits, and S Hasegawa. Phase transition and stability of Si(111)-8x2-In surface phase at low temperatures. *Surf. Sci.*, 488:15, 2001.

[148] W Lee, H Shim, and G Lee. Effects of in adsorption on the phase transition of an in/si(111) surface. *J. Korean Phys. Soc.*, 56:943, 2010.

[149] H Shim, S-Y Yu, W Lee, J-Y Koo, and G Lee. Control of phase transition in quasi-one-dimensional atomic wires by electron doping. *Appl. Phys. Lett.*, 94 (23):231901, Jan 2009. doi: 10.1063/1.3143719.

[150] Harumo Morikawa, C. C Hwang, and Han Woong Yeom. Controlled electron doping into metallic atomic wires: Si(111)4×1-In. *Phys. Rev. B*, 81(7):075401, Feb 2010. doi: 10.1103/PhysRevB.81.075401.

[151] T. Shibasaki, N. Nagamura, T. Hirahara, H. Okino, S. Yamazaki, W. Lee, H. Shim, R. Hobara, I. Matsuda, G. Lee, and S. Hasegawa. Phase transition temperatures determined by different experimental methods: Si(111)4×1-In surface with defects. *Phys. Rev. B*, 81(3):035314, Jan 2010. doi: 10.1103/PhysRevB.81.035314.

[152] Geunseop Lee, Sang-Yong Yu, Hyungjoon Shim, Woosang Lee, and Ja-Yong Koo. Roles of defects induced by hydrogen and oxygen on the structural phase transition of Si$(111)4 \times 1$-In. *Phys. Rev. B*, 80:075411, Aug 2009. doi: 10.1103/PhysRevB.80.075411.

[153] T. Frigge, B. Hafke, T. Witte, B. Krenzer, C. Streubühr, A. Samad Syed, V. Mikšić Trontl, P. Zhou I. Avigo, M. Ligges, D. von der Linde, U. Bovensiepen, M. Horn von Hoegen, S. Wippermann, A. Lücke, S. Sanna, U. Gerstmann, and W. G. Schmidt. Optically excited structural transition in atomic wires on surfaces at the quantum limit. *Accepted for publication in Nature*, 2017.

[154] Deok Mahn Oh, S. Wippermann, W. G. Schmidt, and Han Woong Yeom. Oxygen adsorbates on the si$(111)4 \times 1$-in metallic atomic wire: Scanning tunneling microscopy and density-functional theory calculations. *Phys. Rev. B*, 90:155432, Oct 2014. doi: 10.1103/PhysRevB.90.155432.

[155] Hyungjoon Shim, Heechul Lim, Younghoon Kim, Sanghan Kim, Geunseop Lee, Hye-Kyoung Kim, Chiho Kim, and Hanchul Kim. Initial stages of oxygen adsorption on In/Si(111)-4×1. *Phys. Rev. B*, 90:035420, Jul 2014. doi: 10.1103/PhysRevB.90.035420.

[156] Stefan Wippermann, Nadja Koch, and Wolf Gero Schmidt. Adatom-induced conductance modification of in nanowires: Potential-well scattering and structural effects. *Phys. Rev. Lett.*, 100(10):106802, 2008. ISSN 0031-9007. doi: 10.1103/PhysRevLett.100.106802.

[157] Tomoya Uetake, Toru Hirahara, Yoichi Ueda, Naoka Nagamura, Rei Hobara, and Shuji Hasegawa. Anisotropic conductivity of the Si(111)4 $\times$ 1-In surface: Transport mechanism determined by the temperature dependence. *Phys. Rev. B*, 86:035325, Jul 2012. doi: 10.1103/PhysRevB.86.035325.

[158] Hiroyuki Okino, Iwao Matsuda, Rei Hobara, Shuji Hasegawa, Younghoon Kim, and Geunseop Lee. Influence of defects on transport in quasi-one-dimensional arrays of chains of metal atoms on silicon. *Phys. Rev. B*, 76:195418, Nov 2007. doi: 10.1103/PhysRevB.76.195418.

[159] Tomoya Uetake, Toru Hirahara, Yoichi Ueda, Naoka Nagamura, Rei Hobara, and Shuji Hasegawa. Anisotropic conductivity of the Si(111)4 $\times$ 1-In surface: Transport mechanism determined by the temperature dependence. *Phys. Rev. B*, 86:035325, Jul 2012. doi: 10.1103/PhysRevB.86.035325.

[160] P M Chaikin and T C Lubensky. *Principles of Condensed Matter Physics*. Cambridge University Press, Cambridge, 2000.

[161] H. W. Yeom, D. M. Oh, S. Wippermann, and W.G. Schmidt. Impurity-mediated early condensation of a charge density wave in an atomic wire array. *ACS Nano*, 10:810, 2016. doi: 10.1021/acsnano.5b05925.

[162] X. López-Lozano, A. Krivosheeva, A. A. Stekolnikov, L. Meza-Montes, C. Noguez, J. Furthmüller, and F. Bechstedt. Reconstruction of quasi-one-dimensional In/Si(111) systems: Charge- and spin-density waves versus bonding. *Phys. Rev. B*, 73(3), 2006. ISSN 1098-0121. doi: 10.1103/PhysRevB.73.035430.

[163] P. Baum and A. H. Zewail. Breaking resolution limits in ultrafast electron diffraction and microscopy. *Proceedings of the National Academy of Sciences*, 103 (44):16105–16110, Oct 2006. ISSN 1091-6490. doi: 10.1073/pnas.0607451103.

[164] A Cavalleri, Cs Tóth, C W Siders, J A Squier, F Raksi, P Forget, and J C Kieffer. Femtosecond Structural Dynamics in VO_2 during an Ultrafast Solid-Solid Phase Transition. *Phys. Rev. Lett*, 2001.

[165] P Beaud, S L Johnson, E Vorobeva, U Staub, R A De Souza, C J Milne, Q X Jia, and G Ingold. Ultrafast Structural Phase Transition Driven by Photoinduced Melting of Charge and Orbital Order. *Phys. Rev. Lett*, 2009.

[166] Maher Harb, Ralph Ernstorfer, Christoph T Hebeisen, Germán Sciaini, Weina Peng, Thibault Dartigalongue, Mark A Eriksson, Max G Lagally, Sergei G Kruglik,

and R J Dwayne Miller. Electronically Driven Structure Changes of Si Captured by Femtosecond Electron Diffraction. *Phys. Rev. Lett*, 2008.

[167] Germán Sciaini, Maher Harb, Sergei G Kruglik, Thomas Payer, Christoph T Hebeisen, Frank-J Meyer zu Heringdorf, Mariko Yamaguchi, Michael Horn-von Hoegen, Ralph Ernstorfer, and R J Dwayne Miller. Electronic acceleration of atomic motions and disordering in bismuth. *Nature*, 2009.

[168] M. Beye, F. Sorgenfrei, W. F. Schlotter, W. Wurth, and A. Föhlisch. The liquid-liquid phase transition in silicon revealed by snapshots of valence electrons. *Proc. Natl. Acad. Sci.*, 2010.

[169] Hao Hu, Hepeng Ding, and Feng Liu. Quantum Hooke's Law to Classify Pulse Laser Induced Ultrafast Melting. *Sci. Rep.*, 5:8212, 2015.

[170] E. Speiser, S. Chandola, K. Hinrichs, M. Gensch, C. Cobet, S. Wippermann, W. G. Schmidt, F. Bechstedt, W. Richter, K. Fleischer, J. F. McGilp, and N. Esser. Metal-insulator transition in Si(111)-(4 × 1)/(8 × 2)-In studied by optical spectroscopy. *Phys. Status Solidi B*, 247(8):2033–2039, 2010. ISSN 03701972. doi: 10.1002/pssb.200983961.

[171] A. Stekolnikov, Friedhelm Bechstedt, Stefan Wippermann, Wolf Gero Schmidt, Arrigo Calzolari, and Marco Buongiorno Nardelli. Hexagon versus trimer formation in in nanowires on Si(111): Energetics and quantum conductance. *Phys. Rev. Lett.*, 98(2):026105, 2007. ISSN 0031-9007. doi: 10.1103/PhysRevLett.98.026105.

[172] W G Schmidt, S Wippermann, S Sanna, M Babilon, N J Vollmers, and U Gerstmann. In-Si(111)(4×1)/(8×2) nanowires: Electron transport, entropy, and metal-insulator transition. *phys. stat. sol. (b)*, 249:343, 2012.

[173] P. H. Dederichs, S. Blügel, R. Zeller, and H. Akai. Ground states of constrained systems: Application to cerium impurities. *Phys. Rev. Lett.*, 53:2512–2515, Dec 1984. doi: 10.1103/PhysRevLett.53.2512.

[174] Andrea Marini, Rodolfo Del Sole, Angel Rubio, and Giovanni Onida. Quasiparticle band-structure effects on the *d* hole lifetimes of copper within the *GW* approximation. *Phys. Rev. B*, 66:161104, Oct 2002. doi: 10.1103/PhysRevB.66.161104.

[175] Marco Cazzaniga. GW and beyond approaches to quasiparticle properties in metals. *Phys. Rev. B*, 86:035120, Jul 2012. doi: 10.1103/PhysRevB.86.035120.

[176] X. Gonze, B. Amadon, P.-M. Anglade, J.-M. Beuken, F. Bottin, P. Boulanger, F. Bruneval, D. Caliste, R. Caracas, M. Côt;é, T. Deutsch, L. Genovese, Ph. Ghosez, M. Giantomassi, S. Goedecker, D.R. Hamann, P. Hermet, F. Jollet, G. Jomard, S. Leroux, M. Mancini, S. Mazevet, M.J.T. Oliveira, G. Onida,

Y. Pouillon, T. Rangel, G.-M. Rignanese, D. Sangalli, R. Shaltaf, M. Torrent, M.J. Verstraete, G. Zerah, and J.W. Zwanziger. ABINIT: first-principles approach to material and nanosystem properties. *Comput. Phys. Commun.*, 180(12):2582 – 2615, 2009. ISSN 0010-4655. doi: 10.1016/j.cpc.2009.07.007.

[177] V. P. Zhukov and E. V. Chulkov. Lifetimes of low-energy electron excitations in metals. *J. Phys. Condens. Matter*, 14(8):1937–1947, Feb 2002. ISSN 1361-648X. doi: 10.1088/0953-8984/14/8/321.

[178] M. Bauer, S. Pawlik, and Martin Aeschlimann. Electron dynamics of aluminum investigated by means of time-resolved photoemission. *Laser Techniques for Surface Science III*, Apr 1998. doi: 10.1117/12.307123.

[179] V.I. Anisimov. *Strong Coulomb Correlations in Electronic Structure Calculations*. Advances in Condensed Matter Science. Taylor & Francis, 2000. ISBN 9789056991319.

[180] K. Fleischer, S. Chandola, N. Esser, W. Richter, and J. F. McGilp. Surface phonons of the Si(111):In-(4×1) and (8×2) phases. *Phys. Rev. B*, 76:205406, 2007.

[181] S Riikonen, A Ayuela, and D Sanchez-Portal. Metal-insulator transition in the In/Si(111) surface. *Surf. Sci.*, 600:3821, 2006.

[182] C. González, Jiandong Guo, J. Ortega, F. Flores, and H. H. Weitering. Mechanism of the band gap opening across the order-disorder transition of Si(111)(4×1)-In. *Phys. Rev. Lett.*, 102(11):115501, Mar 2009. doi: 10.1103/PhysRevLett.102.115501.

[183] P. Welch. The use of fast fourier transform for the estimation of power spectra: A method based on time averaging over short, modified periodograms. *IEEE Transactions on Audio and Electroacoustics*, 15(2):70–73, Jun 1967. ISSN 0018-9278. doi: 10.1109/TAU.1967.1161901.

[184] Hans Huebl, Andre R. Stegner, Martin Stutzmann, Martin S. Brandt, Guenther Vogg, Frank Bensch, Eva Rauls, and Uwe Gerstmann. Phosphorus donors in highly strained silicon. *Phys. Rev. Lett.*, 97:166402, Oct 2006. doi: 10.1103/PhysRevLett.97.166402.

[185] Dr. Max Migliorato. Empirical potential methods and strain in atomistic simulations. Presentation, Jan. 2012. URL `http://www.tmcsuk.org/TMCSIII/presentations/Leeds2012.pptx`.

[186] J. Singh. *Physics of Semiconductors and Their Heterostructures*. Electrical engineering series. McGraw-Hill, 1993. ISBN 9780071128353.

[187] Marcus D. Hanwell, Donald E. Curtis, David C. Lonie, Tim Vandermeersch, Eva Zurek, and Geoffrey R. Hutchison. Avogadro: an advanced semantic chemical editor, visualization, and analysis platform. *J. Cheminform.*, 4(1):17, 2012. ISSN 1758-2946. doi: 10.1186/1758-2946-4-17.

List of Figures

1.1 Organic solar cells offer a large flexibility for new application possibilities. The image is taken from Ref. 4 and under a Creative Commons License (CC BY-NC-SA 3.0). 2

2.1 Schematic comparison of the pseudopotential V$^{\mathrm{PS}}$ with the original core potential V. Furthermore, the corresponding wave functions ϕ^{PS} and ϕ^{AE} are depicted. Both wave functions have to be equal from the cutoff radius r_c[29],[30]. 11

2.2 Ideal quantum wire (*left*) with parabolic band structure (*right*). The energy levels differ due to an applied voltage U to the ends of the ballistic conductor. 15

2.3 *Left:* System with a scattering region in which a current I is transmitted with a probability T and reflected with a probability $(1-T)$. An example for a simple scattering region is a potential barrier (*right*). 16

2.4 Composition of the system to be analyzed. The middle scattering region is allowed to inherit every kind of defect, however, the surrounding ideal contact unit cells have to be semi-infinite periodically repeated along z direction. 18

2.5 Possibilities to model a gold chain with an adsorbed CO scatterer. . . . 21

2.6 Exemplary division of an unit cell of an infinite gold chain into 18 slabs. 21

2.7 The red marked interface is surrounded by the same atoms in the periodically continued contact (*left*) and the full scattering system (*right*). 28

2.8 Flowchart for the calculation of $\mathrm{COHP}(E)$. 37

2.9 Computation time needed to determine a COHP diagram using `LOBSTER` and the present implementation for bulk diamond and indium nanowires with 8 and 1152 atomic orbitals, respectively (calculated on a single node with 24 cores; note the logarithmic scale). 38

2.10 Chemical bonding results for a carbon-carbon bond in diamond with comparison between Ref. 57 (red) and the present implementation for the `Quantum Espresso` package (blue). Tetrahedron smearing is used in both cases to obtain smooth curves. Note that the x axis plots the negative COHP quantity to have antibonding left and bonding states right. 39

3.1 *Left:* P3HT single chain, *Right:* Model for a bulk P3HT crystal from side view with two monomers per unit cell (blue). 41

3.2 The effective electron potential (*top*) is calculated along a line through the thiophene rings for various displacements between two molecular layers (*bottom*). 44

3.3 Quantum conductance perpendicular to the P3HT layers in dependence on the additional offset between two layers. Red: results of the full scattering approach. Blue: values obtained within the WKB approximation. 45

3.4 System setup for quantum conductance calculations across a chain torsion. Note that the atoms of the outer two monomers (shaded blue) of the scattering region are kept frozen during structural relaxation to guarantee a consistent structural interface between the scattering region and the ideal contacts. Moreover, two monomers outside the scattering region are added (shaded red) to decouple the torsion from its periodic images in the self-consistent calculations. 46

3.5 Calculated quantum conductance along single twisted thiophene-thiophene bonds (red) and configurations which distribute the total torsion angle over several thiophene-thiophene linkages due to structural relaxation (green). The geometries for zero and 180° rotation (indicated by arrows) are shown as insets, respectively. The encircled data point (90°) corresponds to the configuration shown in Fig. 3.8. 46

3.6 Depiction of a charge density isosurface of the HVB for a structure with a 90° torsion between two thiophene rings. 47

3.7 Bond twisting induced change in the total energy for the case that only a single bond is twisted (red) and for the configurations in which the torsion is realized by a sequence of twists (green). Dispersion contributions to the single bond twisting are shown in blue. 48

3.8 a) Relaxed atomic structure for an overall torsion angle of 90° forced by the fixed boundary monomers. The resulting twist angles between adjacent thiophene rings are highlighted. The data point, belonging to the calculated quantum conductance for this configuration, is marked with a circle in Fig. 3.5. The inset depicts the twist angle distributions calculated for various torsions. b) Visualization of the HVB by an isosurface overlaying the same structure as above. 49

3.9 A relaxed bended chain with a minimum curvature radius of 8 Å. The HVB is indicated by a blue isosurface. The quantum conductance in dependence on different curvature radii is shown in the inset. 51

3.10 Setup to determine the transport across an isomer defect. The defect consists of a so-called HH-TT linkage between the thiophene rings which is caused by a swapped position of a hexyl side chain (red rectangle). The contacts are made of ideal regioregular HT-P3HT. In the left contact the atomic numbering is indicated. H denotes the second and T the fifth position. 52

3.11 *Lhs, left part:* Band structure of rr-HT-P3HT (blue) in intrachain direction. *Lhs, middle part:* Ideal quantum conductance for rr-HT-P3HT (blue) compared to calculations for a single isomer defect shown in Fig. 3.10 (red). *Lhs, right part:* Band structure of the scattering region used for the transport calculation (green) and a second region extended by additional two contact monomers on each side (orange). *Rhs:* Orbital character of selected states labeled a), b), and c) in the right band structure on the left hand side. 53

3.12 Three investigated oxygen impurities in P3HT. The COOH and SO_2 defects have been identified by Ref. 87 as stable oxygen-chemisorbed structures while the additionally investigated defect labeled COH-CO turns out to be even more stable. This defect has a stronger influence onto the geometry than the other two since the OH molecule pulls the attached carbon atom out of the thiophene ring plane. 54

3.13 Transport results for a SO_2 (*top*), a COOH (*middle*) and a COH-CO defect (*bottom*). The shaded region is the maximum possible quantum conductance for regioregular head-to-tail P3HT (rr-HT-P3HT) (cf. previous subsection 3.1.4). 55

3.14 *Top:* Density of states calculated for chains containing oxygen impurities (gap states highlighted with dashed lines) in comparison to the pure P3HT polymer. *Bottom:* pDOS projected onto the *s* (green) and *p* (black) states of the two oxygen atoms. The *s* contribution is negligible in the investigated energy range. 56

3.15 HVB indicated as isosurface for the three investigated defects. 57

3.16 P3HT monomer in its unit cell. 59

3.17 *Left:* P3HT band structure in intrachain direction. *Right:* Highest valence band (labeled HVB) together with the tight-binding band fit across the Brillouin zone. 60

3.18 Electron-phonon coupling constants calculated for P3HT (blue) by the method described above. The bars shown in red belong to results derived from model fits to experimental data from Refs. 113 and 114 (redshifted by 4 meV). Note that the references (i) provide relative coupling strengths only and (ii) are restricted to phonon energies above 70 meV. The labeled phonon modes are further discussed in Sec. 3.2.4.1 and visualized in Figs. 3.23 and 3.24. The DFT calculations suggest a phonon gap between 190 meV and 363 meV which is suppressed in the figure. 61

3.19 Polaron band structure with sketched Fermi-Dirac distribution on the right hand side. The chemical potential is indicated in red while the two curves on the right hand side represent the Fermi-Dirac distribution at different temperatures with their respective chemical potential ζ and ζ‘. 63

3.20 Flowchart for the calculation of the coherent $\mu_{\alpha\beta}^{(\mathrm{coh})}$ and incoherent $\mu_{\alpha\beta}^{(\mathrm{inc})}$ mobility. This work flow has to be repeated for every temperature value T. 64

3.21 a) Total mobility results for a P3HT crystal in intra- and interchain direction. b) Same data as in a) but as Arrhenius plot. 65

3.22 Calculated hole mobility assuming that the six lowest phonon frequencies are increased by 10 % (turquoise) or that the phonon frequencies exceeding 80 meV are increased by 10 % (orange) in comparison to the actual values (red). 66

3.23 Calculated eigenvectors of the lowest frequency phonon modes. 67

3.24 Calculated eigenvectors of relevant high-energy phonon modes exceeding 80 meV, ordered according to their polaron binding energy. The HVB orbital character is indicated on the top left (relevant for all the modes shown). 69

4.1 (8×2) hexagon low temperature phase (*top*) and (4×1) room temperature phase forming regular zig-zag chains (*bottom*). 71

4.2 Three different kinds of oxygen defects commonly observed in indium nanowires. The structure and labeling is adopted from Ref. 154 who find a population ratio of $\alpha : \beta : \gamma = 10 : 3 : 1$ by STM measurements for the three kinds of defects. 73

4.3 Schematic setup for the transport calculations along the two directions intra- and interchain. The scattering unit cell containing the oxygen scatterer is sandwiched between ideal wire segments that model semi-infinite ideal contacts. 73

4.4 Side view onto the surface of the (8×2) hexagon phase modeled by three bilayers of silicon with hydrogen termination and a vacuum spacing of 15 Å. 76

4.5 Potential energy surface (PES) of the electronic ground state along the energetic minimum path between the 8×2 hexagon (*right*) and the 4×1 regular zig-zag chain phase (*left*). 76

4.6 Example system in which an excitation from orbital 2 to 4 is modeled. b)–e) show possible configurations which might arise during electronic relaxation. Figures b) and d) constitute thereby converged situations. However, Fig. d) shows an unintentional excited state as the band ordering has changed causing an occupation of different states than selected in a). 77

4.7 New program flow in order to guarantee a convergence to the desired excited state. 78

4.8 *Left/Middle:* Quasiparticle lifetimes calculated for aluminum using Eq. 4.1 (depicted in different units). *Right:* Figure from Ref. 175 showing their $\mathrm{G_0W_0}$ results obtained with the `ABINIT` program package[176] (triangles), older theoretical predictions from Zhukov *et al.*[177] (a) and experimental results by Bauer *et al.*[178] (b). 79

4.9 $\mathrm{G_0W_0}$ quasiparticle lifetimes (*left*) and the experimentally measured population decay time (*right*, from Ref. 153) for the 8×2 phase. 80

4.10 a) Cut through the Brillouin zone in intrachain direction. The cut is discretized using 8 $\mathbf{k}$ points, where each represents one sector which is used to address different excited state configurations. The color of the bands indicates whether they originate from the silicon substrate or the indium nanowires while the shaded gray area visualizes the projected silicon bulk band structure. b) Potential energy surfaces for the ground state (known from Fig. 4.5) and different vertical excitations over the band gap. The solid lines excite only between the HVB and the LCB in one sector (0.25 e$^-$/8×2 unit cell), while the dashed lines include also the symmetric counterpart (0.5 e$^-$/8×2 unit cell). The orange arrow in part a) shows exemplary the excitation $\mathrm{H}_4 \rightarrow \mathrm{L}_4$. c) Further excited state configurations which do not necessarily conserve momentum due to electronic relaxation. The green curve models an excited state with holes in sectors 1 & 8 in the HVB and the underlying HVB-1 and electrons in sectors 4 & 5 in the LCB and LCB+1 (1.0 e$^-$/8×2 unit cell). 81

4.11 a) Band structure of the 8×2 phase as depicted in Fig. 4.10. b) Band structure of the 4×1 phase (in a 8×2 cell for easier comparison). The turquoise highlighted bands correspond to the S_1 and the orange ones to the S_2 band in the 4×1 cell (see, e.g., Refs. 130 & 138 for labeling conventions). All these shaded bands around $\mathrm{k_x} = 0$ and $\mathrm{k_x} = \pm 0.5$ constitute the crucial parts in the Brillouin zone for driving the phase transition by excitation. 82

4.12 Excerpt of the band structure for a structure slightly before (closer to the 8×2 phase, *top*) and after (*bottom*) the maximum of the potential barrier. Orange drawn bands are occupied while black ones are empty. . 83

4.13 Orbitals belonging to the special bands and sectors for the phase transition. The colors correspond to the ones used in Fig. 4.11 to mark the orbitals in the band structure. The arrows indicate two important phonon modes for the phase transition. 84

4.14 *Left:* A COHP bonding analysis between the green and blue marked atoms inside the 8×2 unit cell will include also unwanted but strong contributions from the interaction of the green marked atom with the closer periodic image of the blue atom. *Right:* By extending the unit cell to a 8×4 one, the periodic images are separated far enough to exclude their influence onto the bonding results. 85

4.15 Crystal orbital Hamilton population (COHP) analysis for the 8×2 and 4×1 phase. The curves on the left show the COHP results for two selected bonds marked on the right in the same color. COHP values smaller/larger than zero indicate bonding/antibonding states, respectively. The energy integral over such COHP curves weighted with the occupation number of the corresponding states yields the total bond strength. These calculations are performed for all possible atom pairs and are depicted as color coded bonds (*right*), where dark drawn bonds indicate the ones with the largest bond strengths. 86

4.16 *Top:* The black curve depicts the known potential energy surface, which exhibits two minima belonging to the 8×2 phase (*right*), and the 4×1 phase (*left*), whose bonds are color coded as insets (from Fig. 4.15). The colored ellipses mark those bonds for which the bond strengths are traced along the phase transition in the lower graph. 87

4.17 *Left:* Band structure of the 8×2 hexagon phase from Fig. 4.11 a). *Right:* COHP diagram for the indium-indium bond marked green in Fig. 4.16. 88

4.18 *Left:* Three selected potential energy surfaces from Fig. 4.10. *Right:* COHP changes due to the selected excitations. Letters denote the respective positions on the PESs shown left. Blue drawn bonds increase while red drawn ones decrease in strength upon excitation. 88

4.19 *Left:* Three selected potential energy surfaces from Fig. 4.10 for which MD simulations are performed. *Right:* Time evolution of the structural deviation to the 4×1 phase for the three selected excitations starting from the 8×2 phase. The number of excited electrons refers to a 8×2 unit cell. 90

4.20 Short time Fourier transformation of the atom velocities obtained by a molecular dynamic simulation with only two phonon modes (18 cm^{-1} & 27 cm^{-1}) excited at $t = 0$. A Welch window[183] of length 1.8 ps is used to reduce the artifacts caused by a limited window size. The inset shows the contributions coming solely from the indium atoms. 91

4.21 Excitation thresholds visualized by means of PES gradients. The green, red and blue curves depict the already known PESs from the previous section. The turquoise PES is based on a full occupation inversion between the highest occupied valence and the lowest unoccupied conduction band (2 e^-). The number of electrons shuffled for the red PES is lowered by 25 % to about 0.4 e^- for the pink one. 92

4.22 Phase-transition time constant τ in dependence on excitation strength. The blue curve depicts the theoretically predicted results for different numbers of excited electrons per 8×2 unit cell. The red points show the experimentally determined transition times of Ref. 153, measured by Tim Frigge in dependence on the exciting laser fluence. 93
4.23 Phase-transition time constants in dependence on the applied strain (top axis) and the averaged change in bonding energies in the first layer (bottom axis). 94

5.1 One of the analyzed oxygen impurities. 96
5.2 One of the important high frequency modes reducing the charge carrier mobility. 96
5.3 The two investigated indium nanowire phases. 97

A.1 Dialog box of the “Maximize periodic distance Extension”. 100
A.2 *Left:* Carbon nanotubes in a unit cell with a nearest periodic neighbor distance of 9.1 Å. *Middle:* Same geometry from the side view. *Right:* Rotated structure by the implemented extension which increased the nearest periodic neighbor distance to 11.4 Å. 101
A.3 *Left:* All atoms are folded into the unit cell. *Right:* New extension restored the full molecule. 102
A.4 Input dialog in which the `Quantum Espresso` input files for the left & right contacts as well as for the scattering region can be selected separately. 103
A.5 The angles between two adjacent thiophene rings has a crucial influence onto the transport properties of the polymer P3HT. 103
A.6 *Left bottom:* SiC surface and an arbitrarily oriented P3HT molecule. *Middle top:* Dialog box for the “Put in plane” extension which asks for the actual and the desired plane. Both planes can optionally be determined by the extension by providing an atom and two bonds spanning the plane. *Right bottom:* Aligned molecule onto the SiC surface by the extension. 104

List of Tables

3.1 Calculated binding energies (in eV, with respect to gas phase O_2) for various defect configurations. The results are compared with the values obtained for molecular crystals in Ref. 87. 55

Acknowledgement

At this point I want to express my sincere thanks to all people who were a great help for me during my time as a PhD student.

First of all, I thank my supervisor Prof. Dr. rer. nat. habil. Wolf Gero Schmidt very much for his continuous support and the fruitful discussions which were a great help to improve this work. He was always gladly willing to answer my questions and provided all necessary conditions to realize this work.

I also wish to thank Dr. Uwe Gerstmann for his support and very helpful discussions. Especially his knowledge about implementation details in the program package `Quantum Espresso` helped me significantly to write my own program extensions.

Moreover, I appreciate the support from my office colleagues Martin Rohrmüller, Dr. Nora Vollmers and Kris Holtgrewe and my further colleagues Sergej Neufeld, Maximilian Kulke, Tobias Wecker, Alex Widhalm, Christian Braun and Christoph Dues who were always willing to answer my questions or to help me elsewhere. I would also like to emphasize the great helpfulness of our secretary Simone Lange who was always willing to support us when someone needed help.

Great thanks also to Prof. Dr. rer. nat. habil. Michael Horn-von Hoegen for kindly agreeing to take on the task of examiner and for his very helpful experimental cooperation. In this sense, I thank also my experimental colleagues Bernd Hafke, Dr. Tim Frigge and Dr. Manuel Ligges from the Duisburg-Essen university for the long-standing and extremely fruitful cooperation and their supply of experimental data.

Finally my thanks go to my lovely wife Sophie who encouraged me and was always there for me, thereby making the life worth living.